University of Zululand

Synthesis of binary, ternary, and alloyed metal sulfides by a solvent-less route

By

Philangezwi Welcome Zibane

(20065559)

B. Sc. (Hons) (University of Zululand)

Dissertation

Submitted in fulfilment of the Requirements for the Degree

MASTER OF SCIENCE

In the field of

CHEMISTRY

Faculty of Science and Agriculture

University of Zululand

Supervisor: Prof. N. Revaprasadu (University of Zululand)

Co-supervisor: Dr M. D. Khan (University of Zululand)

September 2020

DECLARATIONS

I hereby declare that the work described in this thesis entitled ‘Synthesis of binary, ternary, and alloyed metal sulfides by a solvent-less route’ is my own work and has not been submitted in any form for another degree or qualification of the University of Zululand or any other university or institution of tertiary education. Information derived from the published or unpublished work of others has been acknowledged in the text and a list of references is given.

Name: Philangezwi Welcome Zibane

Signature …… Date……..

CERTIFICATION BY SUPERVISORS

This is to certify that this work was carried out by Mr. Philangezwi Welcome Zibane in the Department of Chemistry, University of Zululand and is approved for submission in fulfilment of the requirements for the degree of Master of Science in Chemistry.

.....

Supervisor

N. Revaprasadu (PhD)

Professor of Inorganic Chemistry

Department of Chemistry, University of Zululand,

Kwa-Dlangezwa, South Africa.

.....

Co-Supervisor

M.D. Khan (PhD)

Post-Doctoral of Nanotechnology

Department of Chemistry, University of Zululand,

Kwa-Dlangezwa, South Africa.

DEDICATION

This work is dedicated to the creator of earth and heaven almighty God, my wife, kids (Nosihle, Lubanzi, Yizo, Zodwa, Bandile and Kwanda), mum, dad, my sister (Khayelihle Zibane-Xaba) and brothers. Let us do well to others, these will help Africans to conquer all tribulations (political battles and financial imbalances).

Acknowledgements

I would like to convey my humble gratitude to my supervisors, Prof. N. Revaprasadu and Dr Malik Dishad Khan for their motivation, patience and enormous knowledge. Their guidance helped me throughout this research and writing of this thesis. I would also like to gratefully acknowledge the financial support from University of Zululand and NRF/DST through SARChI granted to Prof N. Revaprasadu, which enabled me to pursue this study without any hindrances.

I am equally thankful to Dr S.C Masikane, Dr E. A Gwaza, and Dr S. J. Owonubi, Ms. G. Bildard- Shombe and Mr M Nyemaga for the remarkable roles they played in ensuring the success of this work.

I would also like to thank the entire colleagues of the Chemistry Department of University of Zululand for their support and also lab mates; Mcebisi Khumalo, Sandile Khoza, Amanda Nhlapho, Mfundo Mqadi and Sithole Sanelisiwe, all visiting researchers and former students for their support and assistance during this period of study.

Once more, I would like to thank my family, most importantly my wife (Mrs Zibane) for her constant spiritual and emotional support throughout this journey.

God bless you all.

Table of contents

Abstract

The work outlined in this thesis entails recent advances in reaction protocols to afford high quality semiconductor materials. As a step towards sustainable and green synthesis, this thesis presents the use of a simple, scalable and environmentally benign solventless approach in the preparation of (Ag^{+}, Cd^{2+}, Cu^{2+}, Ni^{2+}, $Zn^{2+}$and Fe^{3+}) doped CoS and (Cu^{2+}, Sb^{3+} and Fe^{3+}) doped $AgBiS_2$ by solid state pyrolysis of ethylxanthate precursors. In addition to the synthetic protocol, the work demonstrates the utility of xanthates as a single source precursor in the fabrication of semiconductor materials due to their low decomposition temperature and high possibility of forming pure crystalline products.

The synthesis part of this study was divided into two sections, the first section was to prepare complexes using ethyl xanthate as a ligand from potassium ethyl xanthate. This was prepared by dissolving a calculated mass of xanthate into a measured amount of distilled water at room temperature followed by reacting with an aqueous solution of the metal nitrate. The second section involves the melt (solvent less) method. This is as follows, a stoichiometric amount of xanthate complexes of the corresponding metal was mixed and crushed to obtain a homogenous mixture. The mixture was then placed in a ceramic boat which was then placed in a glass reactor tube inside the furnace with a temperature of 250 °C under inert conditions for an hour. This methodology was employed for both binary systems and ternary system for this study.

The first chapter reports fundamental aspects of semiconductors. The scope of this literature review chapter is narrowed to the band gap dependent properties of semiconductor materials. Doping of semiconductors has also been discussed as one of the methods used to enhance the conductivity of semiconductors. The chapter also focuses on synthetic routes which provide access to the modulation of the properties of the semiconductors to suit a specific applications. More importantly the chapter provides highlights on the melt method as an alternative approach to circumvent the limitations reported in the use of conventional methods. Examples of both binary and ternary metal chalcogenide semiconductors are also discussed briefly. General applications of metal sulfides are discussed in detail in this thesis.

The work demonstrated in chapter two focused on the synthesis of both ethyl xanthate complexes and (Ag^{+}, Cd^{2+}, Cu^{2+}, Ni^{2+}, $Zn^{2+}$and Fe^{3+}) doped CoS semiconductors. Thermogravimetric analyses of metal ethyl xanthate complexes show clean thermal

decomposition at fairly moderate temperatures, the average decomposition began around 120 °C to and ends between 150 °C and 200 °C. The synthesis of (Ag^{+}, Cd^{2+}, Cu^{2+}, Ni^{2+}, Zn^{2+} and Fe^{3+}) doped CoS were performed by thermal decomposition of a mixture containing 5% of each metal ethyl xanthate at 250°C. The physicochemical properties of the as-prepared semiconductor materials were elucidated by powder X-ray diffraction (p-XRD), transmission electron microscopy (TEM), selected area electron diffraction (SAED), scanning electron microscopy (SEM), energy dispersive spectroscopy (EDs) and ultraviolet visible spectrophotometer (UV-vis) techniques.

Chapter three presents facile cationic (Cu^{2+}, Sb^{3+} and Fe^{3+}) doping in $AgBiS_2$ by the solventless route using xanthate complexes. Thermogravimetric analysis of the as-prepared complexes demonstrated that they all thermalize cleanly at fairly moderate temperatures. Likewise, the physicochemical properties of $AgBiS_2$, $Ag_{1-x}Cu_xBiS_2$, $AgSb_xBi_{1-x}S_2$ and $AgFe_xBi_{1-x}S_2$ systems were ascertained by p-XRD, TEM, SEM and EDX techniques.

The last (fourth chapter), concludes on the progress outlined in the above-mentioned studies towards the environmentally benign techniques for fabrication of semiconductor materials as well as their applicability in solar energy to solve the problem of non-renewable energy crises.

List of Figures

List of Schemes

List of Tables

List of Abbreviations

PEX	Potassium ethyl xanthate
SPP	Single source precursor
DSSC	Dye-sensitised solar cells
AACVD	Aerosol assisted chemical vapor deposition
TOP	Tri-n-octylphosphine
TOPO	Tri-n-octylphosphine oxide
CHNS/O	Carbon Hydrogen Sulphur / Oxygen
TGA	Thermogravimetric analysis
N_2	Nitrogen gas
UV–vis	Ultra violet visible
P-XRD	Powder X-ray diffraction
TEM	Transmission electron microscopy
SEM	Scanning electron microscopy
EDX	Energy Dispersive X-ray analysis
SAED	Selected Area electron Diffraction
EtX	Ethyl xanthate
eV	electron volts

Chapter one

General introduction and literature review

Synthesis of binary, ternary, and alloyed metal sulfides by a solventless route

1.1 Introduction

Extensive research on semiconductors has made a substantial contribution to the production of advanced materials and the development of numerous technological devices [1-4]. The history of semiconductors goes all the way back to the 19th century when different experiments on the electrical properties of materials were conducted [5]. Despite the fact that quite a number of studies were carried out, it was the emergence of silicon and germanium that made a great leap forward in the field [6-11]. Years down the line, scientists and engineers identified multi-element compounds which are inexpensive, easily available, and exhibit properties which can be tuned on specific standards. This includes semiconductors belonging to the II-VI, II-V, IV-VI, II-IV-V and I-III-VI systems [12, 13].

Semiconductors are characterized by an energy band gap which separates the valence and the conduction bands. In principle, the band gap is a major factor determining the optical, electrical and electronic properties of the materials. For bulk semiconductors, the energy band gap is mainly dependent on the composition/identity of the material, and it is therefore a fixed parameter. As the size of the bulky material is reduced to the nanometer scale, the band gap is significantly altered due to quantum confinement effects [14,15]. Consequently, nanostructured semiconducting materials display properties which are different from those exhibited by their bulk counterparts [15]. This type of band-gap engineering has generated a wide realm of optoelectronic property tailoring, that are useful in a variety of fields including energy storage/conversion systems [16], molecular and cellular imaging [17], optoelectronic devices [18, 19] and ultrasensitive detection [20].

Regardless of the size of the material, a semiconductor can either be classified as intrinsic, one which is chemically pure, or extrinsic, one which contains a small amount of added impurities [21]. Introducing controlled amounts of foreign elements into the crystal structure of an intrinsic semiconductor is recognized as an effective way of tuning the properties of the material [22, 23]. The extent to which the properties are altered largely depends on the type of impurity atoms incorporated. These can be categorized into donor atoms and acceptor atoms, subject to the effect they have on the intrinsic semiconductor. Doping a semiconductor with atoms which can donate electrons increases the electron carrier concentration, generating an N-type semiconductor. On the other hand, incorporating electron acceptor impurity atoms increases the hole carrier concentration, generating a P-type semiconductor [24-26]. The science of doping was initially developed for elemental semiconductors such as silicon and germanium. Materials science has now progressed to the point where it has borrowed this old

science previously performed on elemental materials to dope both bulky and nanostructured compound semiconductors [25]. Today, various technological devices such solar cells [27], and light emitting diodes [28], consist of doped compound semiconductors.

The synthetic protocol employed in the preparation of nanostructured materials is one of the principle factors determining the resultant properties and applications of the materials[29, 30]. Numerous techniques for the preparation of semiconductor nanoparticles have been developed over the years, most of which employ the principles of colloidal chemistry or decomposition of single- or multisource organometallic precursors [31-33]. The synthesis of the nanoparticles via thermal decomposition of single molecular precursors in solution is the current dominant technique. Single molecular precursors contain all the elements required in the final structure of the target material and thus allow for easy control of composition and purity of the material [31].

The synthesis of nanomaterials via solventless thermolysis of single molecular precursors is a recently described protocol of nanoparticle synthesis. Precursor decomposition is carried out in air or under inert conditions depending on the target material. During heating, the reaction is initiated by melting of the precursor to form reactive precursor melts, which then decompose to give the intended nanomaterial. Reactions are customarily carried out in the absence of passivating ligands as nanoparticles are stabilized by the ligands generated after decomposition of the precursor. In this regard, the melt method is further referred to as the 'self-capping' approach [34]. There are, however, a few reports in which the synthesis has been performed in the presence of a passivating ligand and/or a catalyst. How well the nanoparticles are passivated depends on the alkyl chain length of the precursor [35, 36].

Metal chalcogenolates, carboxylates, dichalcogenocarboxylates, dichalcogenocarbamates, dithiophosphates, and xanthates are examples of the single source precursors that have been explored for the solventless synthesis of nanostructured materials [34]. Due to their low decomposition temperatures and formation of volatile by products, xanthate precursors have received recent interest for the solventless synthesis of both binary and ternary metal sulfide nanoparticles [37, 38]. The melt method is generally described to be a time effective, cost effective, scalable, environmentally friendly and facile route for the synthesis of nanomaterials.

1.2 Literature review

1.2.1 An introduction to bulky and nanostructured semiconductors

A semiconductor can be defined as a material with an electrical conductivity that falls in the range of 10^{3}-10^{-8} S cm^{-1} [21]. Generally, the electrical conductivity of a semiconductor lies between that of a conductor and an insulator. In conductors, the valence and the conduction bands overlap, hence electrons have the ability to move freely between the bands. On the contrary, the energy separation between the two bands in insulators (energy band gap) is so large that the electrons need unrealistically high potential to move from the valence to the conduction band. In semiconductors, like insulators, there is an energy separation between the two bands. However, this energy separation can allow movement of electrons from the valence band to the conduction band with the help of appropriate energy stimulus such as electromagnetic and thermal energy, amongst others (Figure 1.1). Furthermore, the magnitude of the energy supplied also plays a role to facilitate the transition, aiding the electrons to overcome their energy barrier [39]. For bulky semiconductors, this energy band gap only varies with composition/identity of the material [15].

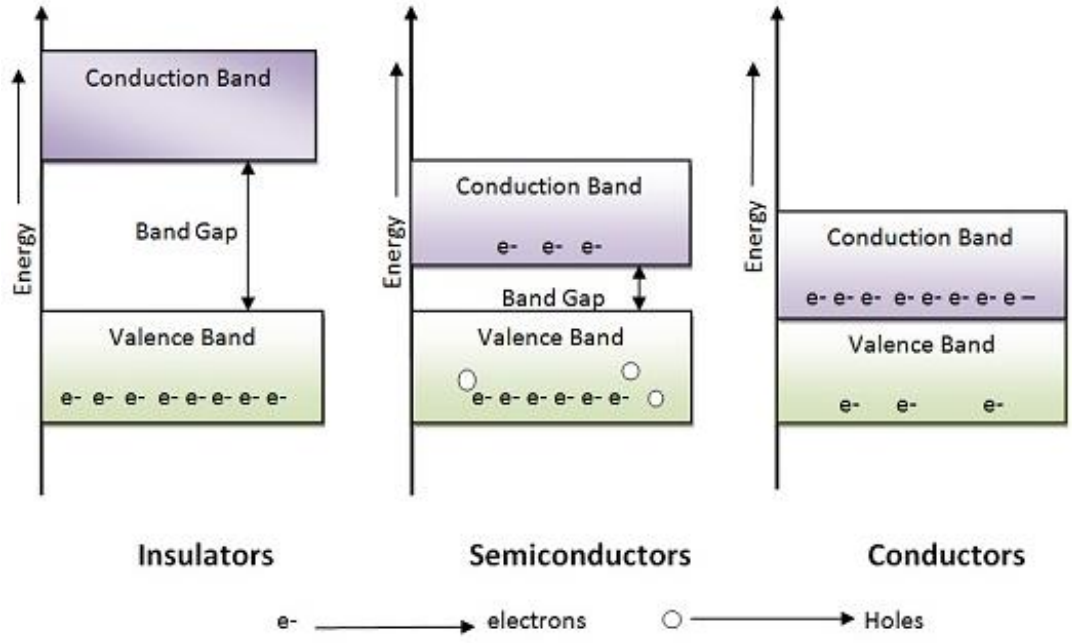

Figure 1.1: The difference between conductors, semiconductors and insulators (https://electronicscoach.com/material.html)

Unlike bulk semiconductors, the band gap of semiconducting nanomaterials can be adjusted by varying different parameters such as size, shape, and composition. In bulk semiconductors, the valence and conduction bands are formed by continuous energy levels. At 0 K, the valence band is filled with electrons, while the conduction band is completely empty. Upon thermal excitation, or absorption of a photon, the electron/s in the valence band moves to the conduction band leaving behind an orbital hole. This hole, which is considered to be a particle with its own charge, binds to the electron via an electrostatic attraction, and the formed hole-electron pair is referred to as an exciton. The distance in the hole-electron pair is called the Bohr radius or exciton Bohr radius. When the size of the semiconductor is smaller than the Bohr radius, the holes and electrons become spatially confined (quantum confinement effect), which results into discrete energy levels instead of the continuous levels observed for bulk semiconductors. Therefore, as the size of a macroscopic semiconductor is decreased to nanometre scale, the band gap of the material increases due to quantum confinement effect. At this point, the wavelength of light, and hence its colour, also becomes size dependent (Figure 1.2) [14, 15, 40]. Due to the small size of the particles (typically in the range of 1-100 nm), and hence high surface area to volume ratio, semiconductor nanoparticles therefore display physical, chemical, optical and electronic properties which are different from those observed in the corresponding bulk materials [31, 41-43]. This feature has enabled the exploitation of the properties and applications of semiconductors in different areas such as luminescence [28], non-linear optics [44], electronics [27] and solar energy conversion [45].

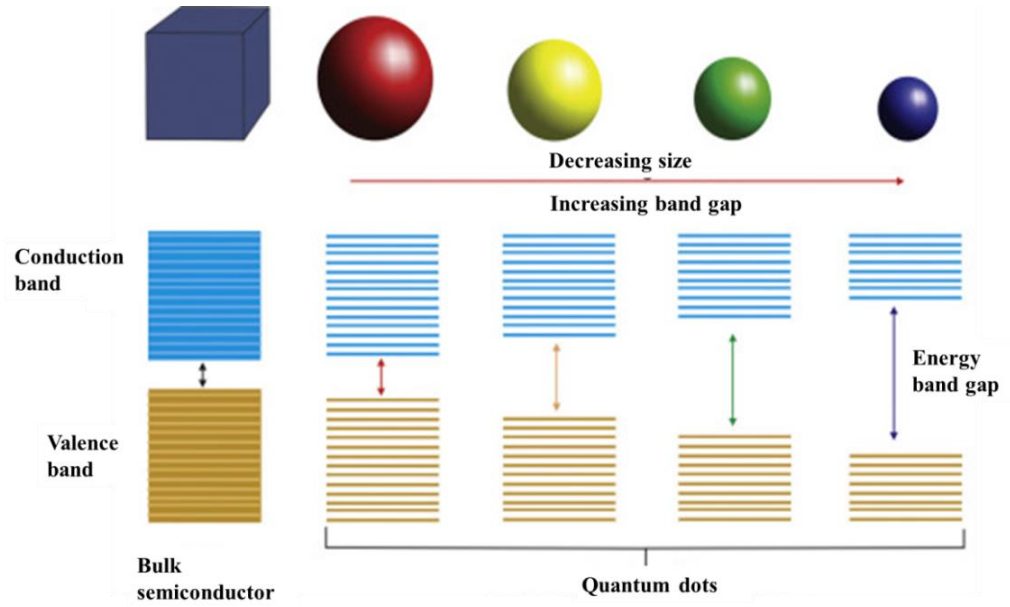

Figure 1.2: Variation of the energy band gap of a semiconductor with size [40].

1.2.2 Binary metal chalcogenide semiconductors

Binary semiconductors constitute a class of compound semiconductors which are made up of two elements. This includes compounds belonging in the group III-V (e.g., BAs, BP), II-VI (e.g., CdS, ZnTe), group I-VII (e.g., CuCl) and group IV-VI (e.g.,SnS, PbSe) systems, just to name a few. The II-VI semiconductors have widespread applications due to their tuneable energy band gaps[46]. Although some occur naturally as minerals, researchers have opted to devise different synthetic methods which provide easy access to tuning their energy band gaps by manipulation of particles features such as size, shape and morphology. Solution-based methods have been the most preferred, however, they are famously known for using toxic chemicals, among other limitations [47, 48]. On the other hand, solventless methods, which are ideal on this regard, are not well explored.

1.2.2.1 Cobalt sulfides

The cobalt sulfide system is among binary materials which have captured the attention of researchers in the field of functional semiconductor materials [49]. Cobalt sulfides have diverse applications owing to their crystallographic phases [30]. Applications of cobalt sulfide materials include optical wave guides and modulated hetero structures amongst others. Recently, cobalt sulfide has been identified as the most promising candidate for energy storage applications, due to its permeable channel, metallic nature, specific surface areas and atomic layered structure [50-52]. Functional cobalt sulfide nanomaterials have been prepared using common reaction methods, the majority being solvent-based [53-55].

1.2.3. Ternary metal chalcogenide semiconductors

Ternary metal chalcogenide semiconductors consist of two metal atoms and a chalcogenide atom [56]. The compounds generally exhibit superior efficiencies over binary semiconductor systems, owing to the synergistic effects resulting from the dual-metal nature which is responsible for the enhancement of the material's electronic properties [57, 58]. However, they are rarely explored due to difficulties associated with their synthesis, control over a three-element phase purity is commonly challenging, especially in cases where reactivities of the precursors are different. Binary phases and/or impurities subsequently form [59, 60]. Ternary materials of the I-V-VI group have attracted a lot of attention due to their promising optical and electronic properties, although still at a development stage [61]. An appropriate example

is the recently identified $AgSbS_2$, which its films and nanoparticles are sought after for application in semiconductor sensitized solar cells [62-64].

1.2.3.1 $AgBiS_2$

Silver bismuth sulfide is a I-V-VI ternary semiconducting material with interesting electronic and magnetic properties [65, 66]. Bulk $AgBiS_2$ has an energy band gap, Eg, of ~1.2 eV [67], which is close to the optimal 1.39 eV suitable for a solar absorber [66]. Furthermore, it has an ideal high absorption coefficient of $\alpha = \sim 105\ cm^{-1}$ at $\lambda = 600$ nm [66]. It is these two features that gives $AgBiS_2$ the potential to be utilized for a high-efficiency solar absorber. Among other merits of $AgBiS_2$, its non-toxic nature becomes favourable towards applications known to impose a threat to environmental health. The nanomaterial counterparts have displayed a comparatively high absorption coefficient of 10^5 to 10^3 cm^1 within the 400–1100 nm wavelength range[68], which enables promising photovoltaic performance, when thin layers of this material are sandwiched between electron-hole conducting materials [69].

1.2.4 Doped semiconductor materials and alloys

The electrical [70], optical [22, 23], magnetic [71] and structural [72] properties of semiconductors can be altered by introducing trace amounts of foreign elements in the crystal structure of the material. These foreign elements are commonly known as dopants and the process of introducing them as impurities in the parent material (intrinsic semiconductor) is known as doping. The doped semiconductor is referred to as an extrinsic semiconductor. Historically, doping was primarily performed to enhance the conductivity of semiconductors via a substitution mechanism which generates P-type or N-type semiconductors. The dopants can either be electron donors or electron acceptors, bringing a change in the charge carrier concentration of the semiconductor. Electron donor dopants are those impurity atoms which can release electrons into the semiconductor crystal lattice whereas electron acceptor dopants accept electrons from the lattice, creating vacancies called holes [21].

1.2.4.1 P-type semiconductors

P-type semiconductors are formed when an intrinsic semiconductor is doped with electron acceptor elements, in which case holes become the majority charge carriers. A hole has a positive electric charge, equal and opposite to the charge on an electron. A common example of P-type doping is the incorporation of trivalent elements such as aluminium, boron or gallium into the Si crystal structure. The dopant, having three valence electrons, replaces one atom of the intrinsic semiconductor, thereby forming a vacancy (hole) with the fourth surrounding atom (Figure 1.3) [26].

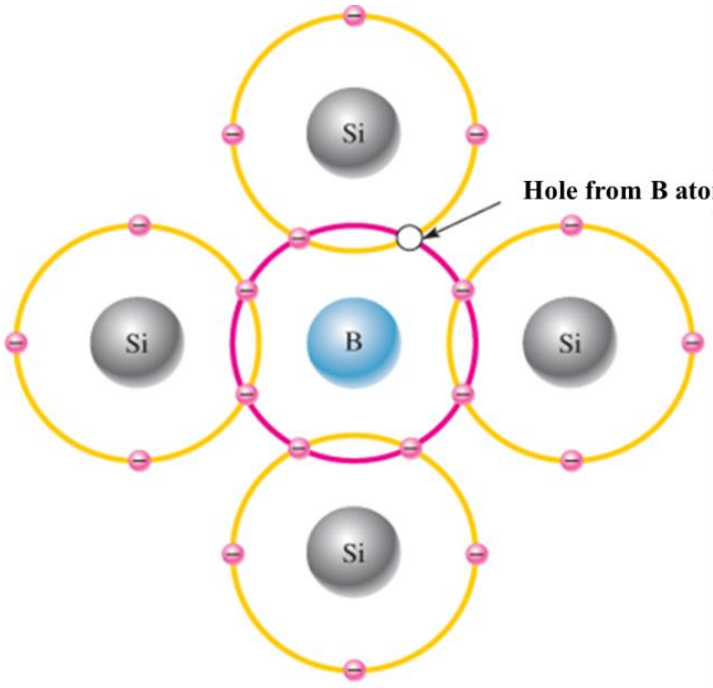

Figure 1.3: Formation of a p-type semiconductor.

1.2.4.2 N-type semiconductors

N-type semiconductors are formed when an intrinsic semiconductor is doped with electron donor elements, in which case the majority charge carriers are the negatively-charged electrons. An example of this type of doping involves the addition of pentavalent elements such as phosphorous into silicon. The dopant (phosphorous) resides in the lattice by substitution of one of the Si atoms, while donating its extra valence electron into the lattice (Figure 1.4). The free mobility of the electron is responsible for conduction [26]. Generally, the conductivity of N-type semiconductors is nearly double to that of P-type semiconductors due to the high mobility of electrons in the former compared to the mobility of holes in the

latter. The mobility of the holes is poor due to their close proximity to the nucleus. Generally, both N-type and P-type doping exploit the octet rule that governs the stability of the atoms in the crystal lattice. The rule indicates that for an atom to be stable, there should be eight electrons in their valence shell. When there is an electron deficiency or excess, the movement of the electrons aiming at achieving stability of the atom is therefore initiating conduction.

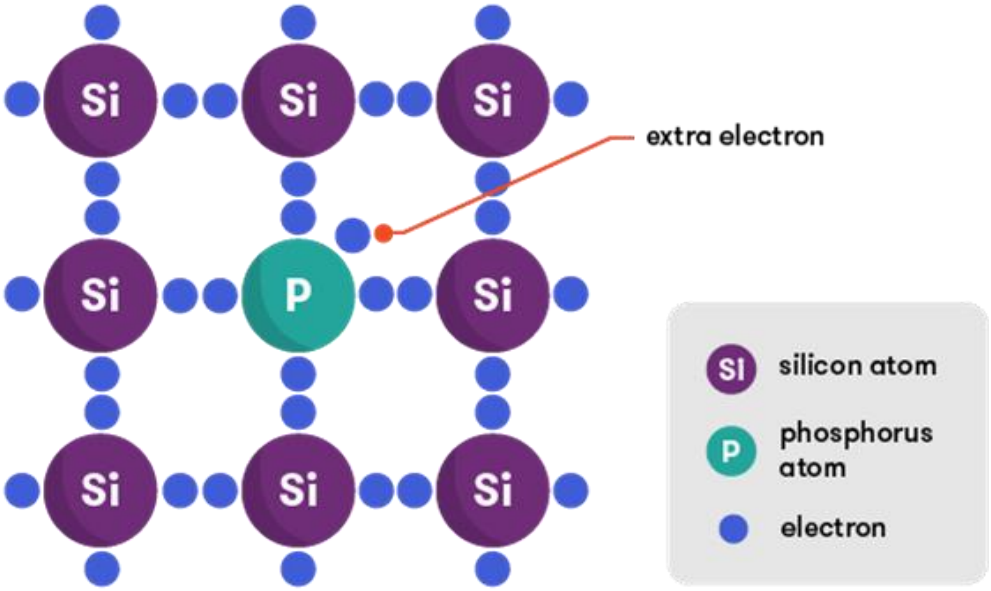

Figure 1.4: Formation of an n-type semiconductor.

Apart from the substitutional approach, doping can also occur interstitially in which the added impurities reside in the sites which are normally unoccupied [73]. The science of doping, initially developed for intrinsic semiconductors in the 1940's [74], has since been slowly introduced to multi element semiconductor nanocrystals [75-77]. Interest on the doping of these nanocrystals has increased in recent years, due to the emergence of novel properties and improvement on existing properties in various semiconductor nanocrystals.

1.2.4.3 Examples of materials used in doping semiconductors

The materials that contain dopants can be binary or ternary which should have low solubility in crystalline grain interiors and the comparable ionic radius to the system [79] that are used in the system of binary and ternary semiconductors are discussed as follows [80].

Nickel has been used as dopant. To prepare thin films, nickel-doped zinc oxide thin films prepared by sol–gel method to investigate of structural, electrical and optical properties [78, 79], nickel doped cadmium sulfide (CdS: $Ni^{2+)}$ by variations in the magnetic property of the nanomaterials were caused by the weak interaction of Ni^{2+} with the host material [80] and nickel-doped CoS_2 nanostructures to investigate the electrocatalysis performance for hydrogen evolution [81]. Nickel can form complexes which are suitable for use in the melt method. Nickel oleate has been used in the melt method, under N_2 to produce Ni nanoparticles which exhibit particle sizes that vary with decomposition temperature [82]. Average particle sizes, calculated from their diameters, are 5 nm (at 330 °C), 5.1 nm (at 350 °C), 5.9 nm (at 380 °C) and 6.6 nm (at 400 °C). The authors also observed temperature having an influence on the crystal phase of the nanoparticles; face-centred cubic (fcc) Ni is obtained at 350 °C, a mixture of fcc with trace amounts of hexagonal close packed (hcp) Ni at 380 °C, as well as a mixture of hcp with traces amounts of fcc at 400 °C. No nickel oxide is observed, even after prolonged exposure to open air, due to the oleate capping layers on the surfaces of the nanoparticles which inhibit oxidation [82]. This gives Ni an advantage to be used in CoS using ethyl xanthate as a ligand.

Antimony (Sb) is a semi-metal which has a similar crystal structure to bismuth with an energy overlap between the valence and conduction band of about 180 meV at 4.2 K [83]. This material has potential for thermoelectric applications due to its highly anisotropic behaviour, low conduction band, effective mass and high electron mobility [84]. This material finds usage in electronics such as an anode in Li-ion battery due to its high Li-storage capacity [85]. Sb acts as an anode because of its capacity for Li-storage. Rath *et al* [86] reported on a solution based approach for the preparation of thin films of copper antimony sulfide, an emerging absorber material for third generation solar cells. In this work they find that copper and antimony xanthates are used as precursor materials for the formation of two different copper antimony sulfide phases: chalcostibite ($CuSbS_2$) and tetrahedrite ($Cu_{12}Sb_4S_{13}$). Han *et al.*[87] investigated regarding their structural and optical properties, which is an essential property in view of applying these materials as light-harvesting agents in semiconductor sensitized solar cells. Starting from molecular precursors antimony *O*-ethyldithiocarbonate (ethyl xanthate, $(C_2H_5OCS_2)_3Sb$), ultra-long Sb_2S_3 nanowires with a diameter in the range of 5–10 nm were easily synthesized at room temperature by employing ethylenediamine both as a solvent and a bidentate ligand. By varying the crystallization duration, the shape of Sb_2S_3 particles evolved from belts, tubes and finally to nanowires through the well-known rolling process.

This synthetic route was workable for the preparation of other chalcogenides such as ZnS and PbS particles with well-defined nanostructures. The photocatalytic experiment of the as-prepared Sb_2S_3 nanowires under visible light indicated that the photodegradation ratio of methyl orange in aqueous solution was up to 95% after 25 min of irradiation, which was much better than that of its bulk counterparts under the same conditions. High efficiency resulted from the broad spectrum response and high surface area nature of the as-synthesized Sb_2S_3 nanowires. Antimony shows that it can form a complex and can be used as a suitable dopant in $AgBiS_2$ base on the above properties and applications.

Iron (Fe), is the most abundant transition metal in the earth's crust and easy form metal sulfides and has potential significant in several applications in Fe-S, such as biomedical and catalytic processes [88, 89] hydrogen generation [90] environmental remediation [91], batteries and solar cells [92-94]. It has a number of advantages over other materials which includes cost and low toxicity, vacancy-dependent crystalline structures which could be useful in bandgap tuning across quantum confinement regimes most importantly doping, as well as interesting magnetic and electric properties [95]. It can exist in several phases, such as pyrite (cubic-FeS_2), marcasite (orthorhombic-FeS_2), pyrrhotite ($Fe_{1-x}S$), greigite (cubic spinel-Fe_3S_4), smythite (Fe_3S_4), troilite-2H (FeS) and mackinawite ($Fe_{1+x}S$), amongst others [96, 97]. Iron sulfide compounds exhibit a wide range of properties, from the semiconducting FeS_2 to ferromagnetic Fe_3S_4 [98]. Amongst the iron sulfide phases, cubic-FeS_2 (pyrite) has attracted most interest, in particular in the development of thin-film solar cells and solid-state batteries, owing to its properties which include strong light absorption (~ 5 × 105 cm^{-1}) and a direct band gap of 0.95 eV [46, 99-101]. Iron can form several complexes such as iron(III) thioxanthates $Fe(S_2C\text{-}S\text{-}R)_3$ which are as stable as their corresponding xanthate complexes. Similar to the case of the xanthates, the stability of the thioxanthates decreases and the ability of the ligand to reduce the central metal atom increases with increasing chain length when R is an alkyl group. Some long-chain ligands are capable of reducing the central iron atom to form an iron(II) complex. Complexes with branched alkyl chains are more stable than the straight-chain analogues [102]. Based on the above properties Fe(III) xanthate can be used as a significant dopant in both CoS and $AgBiS_2$ using ethyl xanthate complexes.

Copper (Cu) is a metal with the following properties based on oxidation states. The binding energy of Cu^{2+} to ethyl xanthate is larger than that of Cu^{+} [103]. Covalent interaction between ethyl xanthate ion and Cu^{+} is relatively weak, whereas the ionic bond interaction is relatively strong. The solution effect was not taken into account, but important information related to

multi-spin states has been gained [104]. Akhtar *et al.* [105] synthesised Bis(*O*-alkyl xanthato)copper(II) (alkyl = ethyl and hexyl) complexes and used them as single source precursors for the synthesis of copper sulfide nanomaterials by using various methods which include thermolysis, solid-state deposition, doctor blade method and melt method at different temperatures and reaction times. The use of copper as copper-doped in titania nanomaterials in a flame aerosol reactor it improved the anatase to rutile phase transformation, decreased crystalline nature and primary particle size, and better suspension stability [106]. Copper-dopants concentration, by doping and precursors of TiO_2 affect the photocatalysis activity of the TiO_2 films obtained on the decomposition of methyl orange. the film activity increases by 53% if a 1% (in mass) of $Cu(CH_3COO)_2$ solution is applied to the glass substrate prior to depositing TiO_2 on it. This shows that the photocatalysis activity, however, can be reduced by the Cu^{2+} dopants that are deposited on the surface of TiO_2 films [107]. They discovered that the melt method produced digenite(Cu_2S-CuS) and covellite (CuS) from the ethyl analogue and pure Digenite (Cu_2S-CuS) phase from hexagon analogue. The octagon analogue gave digenite (Cu_2S-CuS) and chalcocite(Cu_2S) phases. Nanoparticles exhibited spherical and cuboid morphologies [105]. In this study copper(II) ethyl xanthate can be used as dopant in CoS and in $AgBiS_2$ using the melt method to observe the doping effects in both binary and ternary materials.

Zinc has been used in various materials as a dopant. In nature the most common zinc ore is sphalerite (zinc blende) and zinc sulfide mineral. Zinc has been used in different applications, such as zinc doped indium oxide in optical properties and electrical properties [108]. The zinc doped TiO_2 revealed that the lowest concentration of Zn-doped titania nanofibers solution inhibits the growth of *S. in aureus* ATCC 29231 and *E. coli* ATCC 52922 strains antibacterial activity [109] and the development of zinc doped hydroxyapatite for bone implant applications [110]. It is also used in gas sensing application such as zinc-doped copper oxide [111]. Other studies have also used zinc doped in cobalt ferrite. The doping of Zn^{2+} ions in the cobalt ferrite matrices were confirmed by the diffraction peak-shift towards lower angles in photocatalytic application [112]. Zinc can also form complexes of ethyl, isopropyl, and butyl xanthates. These complexes were used in rubber compounds with different xanthate accelerators at low temperatures from 30°C to 150°C. The properties showed that all three xanthate accelerators are effective for room temperature curing which are good polymers of zinc from xanthates as Sulphur source. Of all the metal oxide nanoparticles studied thus far, zinc oxide nanoparticles exhibited the highest toxicity against microorganisms [113]. All the

characteristics of the zinc oxide nanoparticles depend on their particle size, shape, concentration, and exposure time to the bacterial cell. The above zinc properties show that it can be used to melt method and be used in ethyl xanthate to form zinc complexes from zinc salts which are soluble in water to manipulate the cobalt sulphide properties by doping zinc ethyl xanthate in it.

Cadmium has been used mostly as dopant in TiO_2 films by different methods for photocatalytic [114-116] and in zinc oxide (Cd: ZnO) thin films for solar cell applications [117-119]. Cadmium is a good dopant in materials for catalytic and photovoltaic properties. CdS materials also has photocatalytic properties. The enhancement of activity is not limited to the own absorption range of CdS, but also results from a significant extension of the spectral response up to about 620 nm [120]. These results have stimulated many studies on the photochemical production of hydrogen with suspensions of various semiconductors, such as CdS [121], TiO_2 [122], $SrTiO_3$ [123], and ZnS [124]. Cadmium ethyl xanthate complexes has been used to synthesis CdS nanoparticle [125, 126]. The indication of cadmium as a dopant for different materials and in ethyl xanthate it shows that cadmium ethyl xanthate can be used in binary materials of CoS to alter or improve properties of CoS.

1.2.5 Synthetic routes to intrinsic and extrinsic metal chalcogenide semiconductor nanoparticles

Extensive research on the properties and potential applications of semiconductor nanomaterials has generated numerous techniques for the preparation of both intrinsic and extrinsic semiconductors. Metal chalcogenide semiconductor nanoparticles have been synthesized by both solution-based as well as solventless techniques. The solution-based techniques, which are the dominating synthetic approaches, can mainly be grouped into chemical precipitation, hydrothermal/solvothermal and thermal decomposition routes.

1.2.5.1 Chemical precipitation/co-precipitation approach

Chemical precipitation is one of the oldest colloidal approaches of nanoparticles synthesis. In this route, stoichiometric quantities of metal and chalcogenide precursors both dissolved in appropriate solvents are mixed to precipitate the respective metal chalcogenide nanoparticles

at low temperatures. An example is the preparation of CdS nanoparticles from aqueous solutions of $CdCl_2$ and Na_2S at temperatures ranging from 20-80 ºC [127]. Doped semiconductors are prepared in a similar way using the co-precipitation approach. The metal precursor and the dopant precursor are dissolved in appropriate solvents and the two solutions are mixed at room/low temperature. A solution of the chalcogen precursor is then slowly added to this mixture while stirring to precipitate the doped semiconductor nanoparticles. For-instance Aqeel *et al*. prepared Cr-doped ZnS nanoparticles using aqueous solutions of zinc nitrate, chromium acetate and sodium sulfide at 60-70 ºC [128]. The size and shape control of the particles can be achieved by addition of capping agents [128]. This approach is simple, cost-effective and allows for large-scale production of nanomaterials. However, since the synthesis is carried out at low/room temperature, the method normally suffers from poor crystallinity of the synthesized materials. Furthermore, carrying out reactions in air presents challenges for the synthesis of air sensitive semiconductors. A recent modification of the approach involves precipitation of the particles at low temperatures followed by calcination [129].

1.2.5.2 Hydrothermal/solvothermal approach

Hydrothermal and solvothermal techniques are a typical type of wet chemical synthesis which employs aqueous solution (for hydrothermal synthesis), or organic solvents (for solvothermal synthesis) as the reaction medium. Reactions are carried out in a closed system at temperatures higher than the boiling point of the employed solvent and consequently high pressures. These reaction conditions guarantee the solubility of the precursors in the solvent, and increase the reactivity of the precursors. The approach has been used to prepare both intrinsic and extrinsic semiconductors. In a typical reaction, the precursors and other reagents are placed in a closed vessel such as an autoclave or bomb and heated in an oven/furnace at the required temperature and time. The properties of the synthesized nanomaterials can be tuned by varying various parameters such as reaction temperature, pressure, reaction medium, pH and precursor concentration [130-134]. The main advantage of this approach is that it is possible to dissolve almost any precursor in a particular solvent by elevating the reaction temperature and pressure. Furthermore, the approach is cost-effective, easy to operate, and offers high yields of the nanoparticles. However, carrying out the reactions in a closed system makes it impossible to follow the synthetic process in-situ, and devising growth mechanism [135].

1.2.5.3 Hot injection route

The hot injection route involves thermal decomposition of organometallic precursor/s in solution under inert conditions. In a typical reaction procedure, the precursor/precursors, dispersed in the appropriate solvent are rapidly injected in a pre-heated coordinating solvent to afford capped nanoparticles. A typical laboratory setup is shown in Figure 1.5. As described

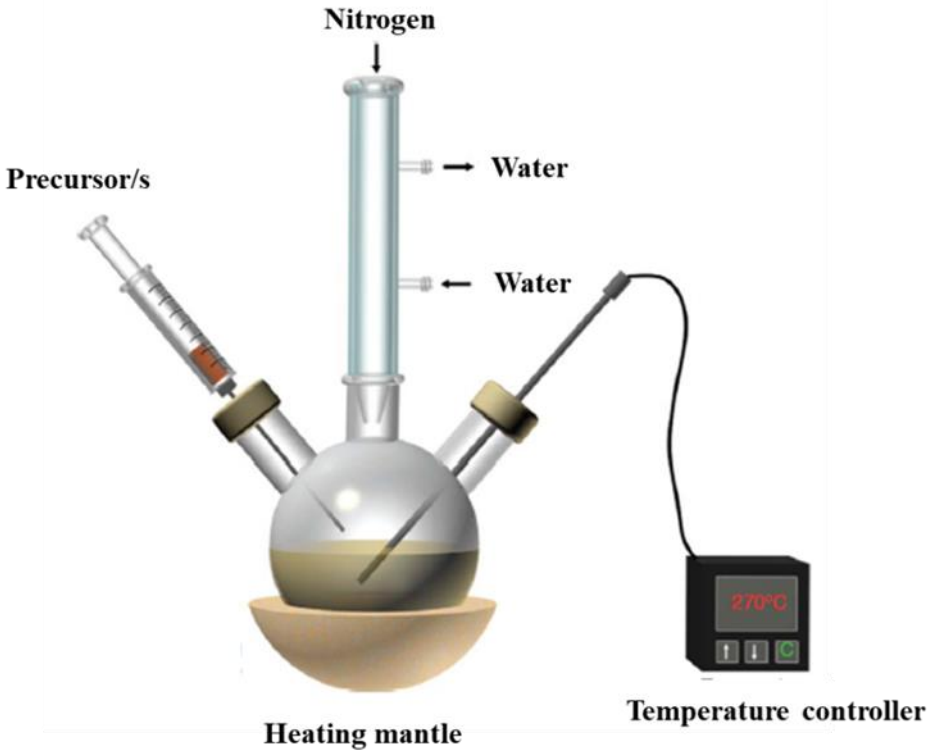

Figure 1.5: Synthesis of semiconductor nanoparticles via the hot injection route [147].

by Bawendi and co-workers in the synthesis of cadmium chalcogenide nanocrystallites, the approach was initially developed for the synthesis of nanoparticles using dual source precursors [140]. In their report, tri-n-octylphosphine (TOP) and tri-n-octylphosphine oxide (TOPO) were used as dispersion medium and coordinating solvent respectively, whereas dimethylcadmium(Me_2Cd),bis(trimethylsilyl)sulfide,seleniumpowder/bis(trimethylsilyl)selenium, and tellurium powder/bis(tert-butyldimethyl)tellurium were used as precursors for cadmium, sulfur, selenium and tellurium respectively. In a typical reaction, a mixture of Me_2Cd and the corresponding chalcogenide source dispersed in TOP was injected rapidly into TOPO preheated to the required temperature. Basically, the formation of TOPO capped nanoparticles is preceded by nucleation followed by low temperature growth. Highly crystalline, nearly monodispersed cadmium chalcogenide nanocrystals were obtained. The route is, however, associated with a number of problems such as the toxicity of the precursors

and extremely harsh reaction conditions. Follow up investigations incorporated less toxic reagents such as cadmium acetate, cadmium chloride, cadmium oxide and 1-octadecene; as well as a wider range of coordinating solvents including phosphonic acids, fatty acids and long-chain amines [136-138].

An alternative approach to the use of a mixture of precursors in the hot injection route is the use of single molecular precursors in which all the elements required in the final nanocrystal structure are contained in one compound. Just like in the dual source precursor route, the single source precursor is dispersed in the appropriate solvent and injected into a hot coordinating solvent; this is followed by its pyrolysis to afford the monomers required for nucleation and growth of the nanoparticles. Contrary to the dual-/multi source precursor approach, this route has the advantage of maintaining the composition as well as purity of the material [31]. Generally, the report by Bawendi *et al*. paved the way to the synthesis of a variety of intrinsic and extrinsic semiconductor nanoparticles using both single- and multi-source precursors [139-146].

1.2.5.4 Heat-up route

The heat-up approach, also referred to as the non-injection route, was developed by Cao *et al* [148]. The approach differs from the hot injection route in that the precursor/precursors are mixed with the coordinating solvent at low temperature and then heated up to the required temperature to initiate the reaction. Compared to the hot injection technique, the approach is much simpler, avoids the use of a dispersion medium, and provides room for scalability of the nanomaterials. Furthermore, it has been shown that the quality of the nanomaterials prepared by the heat up technique is as good as that of the materials prepared via the hot injection route [147].

1.2.5.5 The solventless approach (Melt method)

Modernized melt method presents a simple, solventless and scalable synthetic route towards functional semiconductor materials. The approach has developed from the conventional solid-state methods which require a mixture of pure elements to be heated at extreme temperatures. These conventional methods had limitations associated with upscaling, volatility of the reactants at elevated temperatures and crystallographic phase impurities [149-151]. The melt method basically involves thermal decomposition of suitable metal-organic compounds under an inert atmosphere [152]. The versatility of the method is well portrayed by the different classes of materials it produces, and these are metals, metal oxides, and metal chalcogenides, amongst others [152, 153]. The method, like others used to synthesize nanomaterials, is capable of producing materials exhibiting a wide range of morphologies, which include: spheres, nanorods, nanowires, nanosheets and nanodisks, amongst others. The choice of a precursor also plays a role towards producing nanomaterials bearing interesting features ideally, precursors which decompose at low-to-moderate temperatures and able to achieve self-capping during decomposition, are most preferred. Carboxylates, dithiocarbamates, xanthates, dithiocarboxylates, thiotetrazoles and thiolates are examples of the ligands which have been used as precursors in the synthesis of both bulky and nanostructured materials via the melt method (Figure 1.6). Amongst these precursors, the use of metal xanthate complexes as precursors to the solventless synthesis of metal sulfides has received considerable interest.

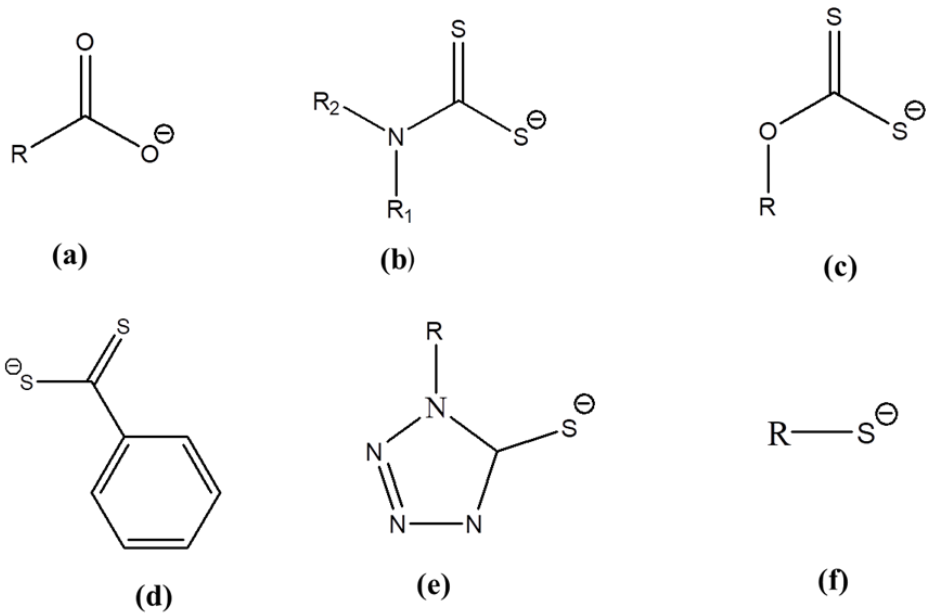

Figure 1.6: Common ligands used to make molecular precursors suitable for melt reactions: (a) carboxylates, (b) dithiocarbamates, (c) xanthates, (d) dithiocarboxylates, (e), thiotetrazoles and (f) thiolates.

1.2.5.6 Xanthates

Xanthates are a group of organic salts represented by the formula $ROCS_2M$ (R = alkyl, M = alkali metal). The name xanthate originates from the Greek word xanthos, meaning yellowish, which is the colour of most xanthate salts. The salts were first discovered in the year 1823 by William C. Zeise, and find most of industrial applications such as production of viscose rayon and as floatation agents in mining. Xanthates can be prepared by the reaction of any desirable primary or secondary alcohol with alkali earth metal hydroxide (such as KOH and NaOH) and CS_2 in an ice bath, as shown in (Scheme 1.1) [154]. Xanthates ligands are known to coordinate with metal centres in a variety of coordination modes e.g. monodentate, bidentate chelating or in a bridging manner leading to the formation of metal complexes (Scheme 1.2). Xanthates have not been well investigated in the past few years, although they exhibit features which are ideal for melt reactions. These features include low melting point and decomposition temperatures, which results to the formation of high quality metal sulfide nanomaterials. Furthermore, xanthates display clean decomposition through the Chugaev elimination mechanism (Scheme 1.3) [155] i.e. the by-products (COS, alkene) produced during the decomposition process are highly volatile and can be removed easily.

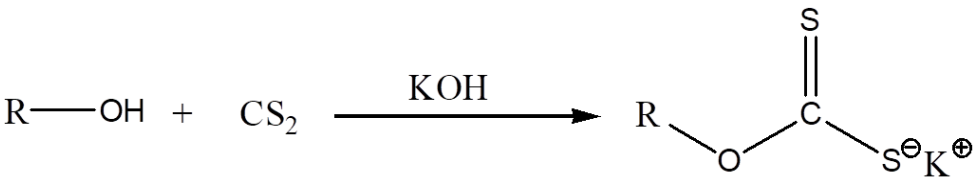

Scheme 1.1: Synthesis of potassium salts of xanthate ligands.

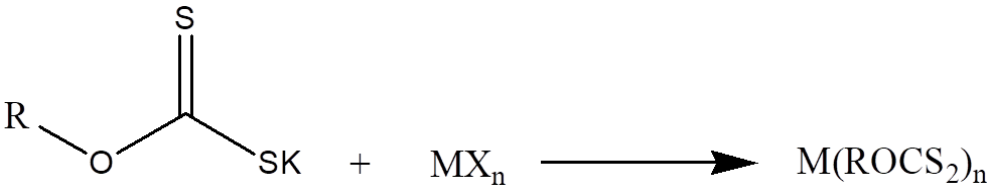

Scheme 1.2: General synthesis of xanthate complexes

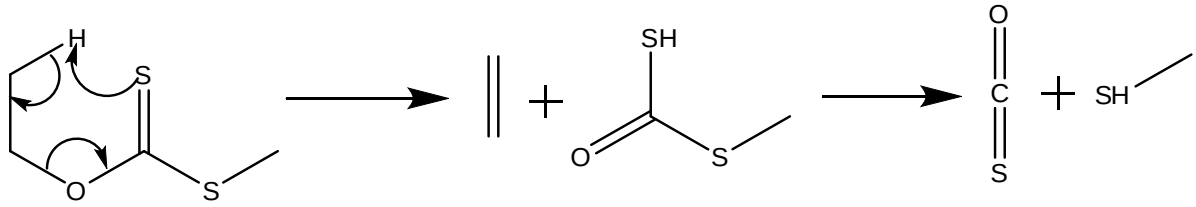

Scheme 1.3: Decomposition mechanism of xanthates by Chugaev elimination

1.2.6 General applications of metal sulfides

1.2.6.1 Photocatalytic and electro catalytic production of hydrogen

Hydrogen is an eco-friendly and renewable fuel useful in various applications such as stationary power generation, eco-friendly vehicles and domestic heating. It is normally found in combination with other elements and a number of methods for its production have been developed [156]. The water splitting process is among the hydrogen generating techniques which have gained much attention [157-159]. In this approach, water is broken down to produce hydrogen and oxygen using electricity (electrochemical water splitting) [157], solar energy (photochemical water splitting) [158] or electricity produced directly from solar energy (photoelectrochemical water splitting) [159]. The process is technologically simple but requires a high amount of energy and therefore lacks significant commercial importance [160]. To improve the kinetics of the reaction and make the water splitting process practical, various

electro- or photocatalysts are normally employed. An efficient photocatalyst is required to display high corrosion resistance, chemical stability, visible light harvesting efficiency and suitable band edges; whereas a good electocatalyst is required to have high electric conductivity, mechanical, thermal and chemical stability, as well as rich redox chemistry [30, 157-159]. In this regard, metal sulfides are among the most studied materials which have demonstrated promise as an efficient photo/electrocatalysts for the production of hydrogen via the water splitting process [30, 161].

1.2.6.2 Batteries and supercapacitors

The non-renewability and rapid depletion of the fossil fuels have created a need for developing various systems that aid in the capture, storage, and/or conversion of the energy obtained from renewable energy sources (such as wind power, hydro power, solar power and biofuels) to ensure energy sustainability. Batteries and supercapacitors are energy storage devices which find application in electric vehicles, portable electronic devices, high-power electric devices, and military devices. Due to the increasing global energy demands, studies on high performance energy storage devices have increased immensely [30]. The nature of the electrode material being one of the major factors determining the performance of the two systems, extensive efforts have been directed towards the search of highly efficient, inexpensive, durable, and resource-rich electrode materials [162-164]. Owing to their unique physical, chemical, and electrochemical properties, metal sulfides are promising electrode materials for both supercapacitors, and batteries [30, 52]. Examples of the studied materials include CoS [165], NiS [37], $AgBiS_2$ [155], $NiCo_2S_4$ [166], $CuCo_2S_4$ [167], $ZnCo_2S_4$ [168], and $FeNi_2S_4$ [169].

1.2.6.3 Optoelectronic devices

Optoelectronic devices are devices which convert light energy to electrical energy or electrical energy to light energy. The devices can be categorized into photodiodes, light emitting diodes, solar cells, and laser diodes. Optoelectronic devices find applications in indication lights, medical devices, computer components, household appliances, switches, instrument panels, traffic signals, telecommunications, military services, and automatic access control systems, among others. The operation of optoelectronic devices is based on the quantum mechanical effects of light on various electronic materials such as nanostructured semiconductors [170, 171]. Once synthesized, the nanostructures are integrated into the devices for further practical use [172].

1.2.6.4 Biological applications

The use of quantum dots for biological and biomedical applications is one of the fastest growing fields of nanotechnology. The unique optical properties of these crystals make them useful in various biological applications such as in-vivo imaging [173], immunoassay [174], drug delivery [175], and tumor cells diagnosis [176]. which ideally requires an integrated experimental and modelling approach due to limited knowledge of the sulphides surface chemistry, particularly when comparing it to the better established, though multifaceted and oxide surface chemistry.

1.3 Statement of the research problem

CoS and $AgBiS_2$ are environmentally friendly and potentially suitable for various applications. The synthesis of these materials at scalable level is desirable and the method should be further extended to investigate the suitability of the method to incorporate different metals for tuning of their electronic structures. Various dopants such as (Ag^{+}, Ni^{2+}, Zn^{2+},Cd^{2+} Cu^{2+} and Fe^{3+}), proven to be suitable materials for energy applications, therefore their incorporation in binary CoS and ternary $AgBiS_2$ will be investigated by a potentially scalable method, and the effect of these dopants will be studied.

Aim and objectives of the study

The aim of this study is to synthesize binary (CoS) and ternary($AgBiS_2$) metal chalcogenides and doping of transition metals such as Fe^{3+}, Ni^{2+}, Zn^{2+}, Cd^{2+}, Ag^{+} and Cu^{2+}, Bi^{3+}, Sb^{3+} into the synthesized materials by using the melt (solvent less) method.

Specific objectives of the study:

i. To synthesize the xanthate ligand and respective metal (Ag, Bi, Co, Cu, Fe and Sb) complexes.

ii. To synthesize phase pure undoped CoS and CoS doped with Ag^{+}, Cu^{2+}, Ni^{2+} , Cd^{2+}, Zn^{2+} and Fe^{3+}, using the melt (solvent less) method.

iii. To synthesize and control the size of ternary system $AgBiS_2$ and observe effect of dopants such as Ag^{+} ,Cu^{2+}, Bi^{3+}, Sb^{3+} and Fe^{3+} using melt (solvent less) method.

iv. To characterize the synthesized materials using X-ray diffraction, transmission electron microscopy, scanning electron microscopy, UV-visible, photoluminescence and Fourier transform infrared spectroscopy.

v. To investigate the effect of doping on water splitting and energy storage applications.

1.4 References

1. Rahman, M.A., *A review on semiconductors including applications and temperature effects in semiconductors.* American Scientific Research Journal for Engineering, Technology, and Sciences (ASRJETS), 2014. **7**(1): p. 50-70.
2. Sealy, B., *Review of III-V semiconductor materials and devices.* Journal of the Institution of Electronic and Radio Engineers, 1987. **57**(1): p. S2.
3. Myers, J.D. and Xue J., *Organic semiconductors and their applications in photovoltaic devices.* Polymer Reviews, 2012. **52**(1): p. 1-37.
4. Neamen, D.A., *An introduction to semiconductor devices.* 2006.
5. Busch, G., *Early history of the physics and chemistry of semiconductors-from doubts to fact in a hundred years.* European Journal of Physics, 1989. **10**(4): p. 254.
6. Teal, G.K. and E. Buehler. *Growth of silicon single crystals and of single crystal silicon pn junctions*. in *Physical Review*. 1952. American Physical Soc One Physics Ellipse, College PK, MD 20740-3844 USA.
7. McAfee, K. and G. Pearson. *The electrical properties of silicon pn junctions grown from the melt*. in *Physical Review*. 1952. American Physical Soc one physics ellipse, College PK, MD 20740-3844 USA.
8. Goucher, F., Pearson,G.L, Teal, G.K Sparks, G.K and Shockley, W. *Theory and Experiment for a Germanium p− n Junction.* Physical Review, 1951. **81**(4): p. 637.
9. Teal, G.K., *Single crystals of germanium and silicon—basic to the transistor and integrated circuit.* IEEE Transactions on electron devices, 1976. **23**(7): p. 621-639.
10. Chapin, D.M., C. Fuller, and G. Pearson, *A new silicon p-n junction photocell for converting solar radiation into electrical power.* Journal of Applied Physics, 1954. **25**(5): p. 676-677.
11. Ruth, R.P. and J.W. Moyer, *Power efficiency for the photovoltaic effect in a germanium grown junction.* Physical Review, 1954. **95**(2): p. 562.

12. Fonstad Jr, C.G. JF Ahadian, Y Royter, SG Patterson, *Compound semiconductor materials and devices*. 1997, Research Laboratory of Electronics (RLE) at the Massachusetts Institute of ….
13. Pamplin, B.R., T. Kiyosawa, and K. Masumoto, *Ternary chalcopyrite compounds.* Progress in Crystal Growth and Characterization, 1979. **1**(4): p. 331-387.
14. Klimov, V.I., *Semiconductor and metal nanocrystals: synthesis and electronic and optical properties*. 2003: CRC Press.
15. Smith, A.M. and Nie S., *Semiconductor nanocrystals: structure, properties, and band gap engineering.* Accounts of chemical research, 2010. **43**(2): p. 190-200.
16. Chattopadhyay, S., L.-C. Chen, and K.-H. Chen, *Energy production and conversion applications of one-dimensional semiconductor nanostructures.* NPG Asia Materials, 2011. **3**(8): p. 74-81.
17. Smith, A.M., Ruan G, Rhyner M. N and Nie S, *Engineering luminescent quantum dots for in vivo molecular and cellular imaging.* Annals of biomedical engineering, 2006. **34**(1): p. 3-14.
18. Linden, K.J., *Precision synthesis of quantum dot nanostructures for fluorescent and optoelectronic devices*. 2007, Google Patents.
19. Chuang, S.L. and S.L. Chuang, *Physics of optoelectronic devices.* 1995.
20. Chen, X., Wang X, Liu L, Yang D and Fan L, *Functionalized semiconductor nanocrystals for ultrasensitive detection of peptides.* Analytica Chimica Acta, 2005. **542**(2): p. 144-150.
21. Spain, E. and Venkatanarayanan A., *13.02 Review of Physical Principles of Sensing and Types of Sensing Materials.* 2014.
22. Qiao, F., Kang R, Liang Q, Cai Y, Bian J and Hou X, *Tunability in the optical and electronic properties of ZnSe microspheres via Ag and Mn doping.* ACS omega, 2019. **4**(7): p. 12271-12277.
23. Bandaru, S. Saranya G, English N.J, Yam C and Chen M, *Tweaking the Electronic and Optical Properties of α-MoO 3 by Sulphur and Selenium Doping–a Density Functional Theory Study.* Scientific reports, 2018. **8**(1): p. 1-12.
24. Peter, Y. and M. Cardona, *Fundamentals of semiconductors: physics and materials properties*. 2010: Springer Science & Business Media.
25. Pierret, R.F. and G.W. Neudeck, *Advanced semiconductor fundamentals*. Vol. 6. 1987: Addison-Wesley Reading, MA.

26. Wolkenstein, T., *Electrons and Holes in a Semiconductor*, in *Electronic Processes on Semiconductor Surfaces during Chemisorption*. 1991, Springer. p. 1-34.
27. Lee, M.-L, Huang F, Chen P and Sheu J, *GaN intermediate band solar cells with Mn-doped absorption layer.* Scientific reports, 2018. **8**(1): p. 1-8.
28. Liu, B., Sharma M, Yu J, Shendre S, Hettiarachchi C and Sharma S, *Light-Emitting Diodes with Cu-Doped Colloidal Quantum Wells: From Ultrapure Green, Tunable Dual-Emission to White Light.* Small, 2019. **15**(38): p. 1901983.
29. Munaro, J., Dolcet, P., Nappini, S., Magnano, E., Dengo, N., Lucchini, G., Speghini, A. and Gross, S., *The role of the synthetic pathways on properties of Ag2S nanoparticles for photothermal applications.* Applied Surface Science, 2020. **514**: p. 145856.
30. Kulkarni, P., Nataraj S.K., Balakrishna RG,. *Nanostructured binary and ternary metal sulfides: synthesis methods and their application in energy conversion and storage devices.* Journal of Materials Chemistry A, 2017. **5**(42): p. 22040-22094.
31. Pickett, N.L. and P. O'Brien, *Syntheses of semiconductor nanoparticles using single-molecular precursors.* The Chemical Record, 2001. **1**(6): p. 467-479.
32. Wang, D., T. Xie, and Y. Li, *Nanocrystals: Solution-based synthesis and applications as nanocatalysts.* Nano Research, 2009. **2**(1): p. 30-46.
33. Ganachari, S.V. and Banapurmath NR, *Synthesis Techniques for Preparation of Nanomaterials.* Handbook of Ecomaterials, Springer, Cham. https://doi. org/10.1007/978-3-319-48281-1_149-1, 2017.
34. Lewis, E., S. Haigh, and P. O'Brien, *The synthesis of metallic and semiconducting nanoparticles from reactive melts of precursors.* Journal of Materials Chemistry A, 2014. **2**(3): p. 570-580.
35. Zhang, C., Zhang S, Yu L, Zhang Z, Zhang P, Z Wu , *Size-controlled synthesis of monodisperse Ag2S nanoparticles by a solventless thermolytic method.* Materials Letters, 2012. **85**: p. 77-80.
36. McNaughter, P.D. Saah SA, Akhtar M, *The effect of alkyl chain length on the structure of lead (II) xanthates and their decomposition to PbS in melt reactions.* Dalton Transactions, 2016. **45**(41): p. 16345-16353.
37. Shombe, G.B., Khan, M.D., Zequine, C., Zhao, C., Gupta, R.K. and Revaprasadu, N., *Direct solvent free synthesis of bare α-NiS, β-NiS and α-β-NiS composite as excellent*

electrocatalysts: Effect of self-capping on supercapacitance and overall water splitting activity. Scientific Reports, 2020. **10**(1): p. 1-14.

38. Alqahtani, T., MD Khan, DJ Kelly, SJ Haigh., *Synthesis of $Bi_{2-2x}Sb_{2x}S_3$ ($0 \leq x \leq 1$) solid solutions from solventless thermolysis of metal xanthate precursors.* Journal of Materials Chemistry C, 2018. **6**(46): p. 12652-12659.
39. Joskow, P.L., *Electricity sectors in transition.* The energy journal, 1998. **19**(2).
40. Kumar, D.S., B.J. Kumar, and H. Mahesh, *Quantum Nanostructures (QDs): An Overview*, in *Synthesis of Inorganic Nanomaterials*. 2018, Elsevier. p. 59-88.
41. Tang, H. Xu, G., Weng, L., Pan, L., & Wang, L. , *Luminescence and photophysical properties of colloidal ZnS nanoparticles.* Acta Materialia, 2004. **52**(6): p. 1489-1494.
42. Grieve, K., P. Mulvaney, and F. Grieser, *Synthesis and electronic properties of semiconductor nanoparticles/quantum dots.* Current opinion in colloid & interface science, 2000. **5**(1-2): p. 168-172.
43. Smith, A.M., Duan, H., Rhyner, M. N., Ruan, G., & Nie, S., *A systematic examination of surface coatings on the optical and chemical properties of semiconductor quantum dots.* Physical Chemistry Chemical Physics, 2006. **8**(33): p. 3895-3903.
44. Tripathi, S. and R. Kaur, *Investigation of non-linear optical properties of CdS/PS polymer nanocomposite synthesized by chemical route.* Optics Communications, 2015. **352**: p. 55-62.
45. Rajeshwar, K. and N.R. De Tacconi, *Solution combustion synthesis of oxide semiconductors for solar energy conversion and environmental remediation.* Chemical Society Reviews, 2009. **38**(7): p. 1984-1998.
46. Xia, J. Jiao J, Dai B, Qiu W, He S, Qiu W, Shen P, Chen L , *Facile synthesis of FeS_2 nanocrystals and their magnetic and electrochemical properties.* Rsc Advances, 2013. **3**(17): p. 6132-6140.
47. Peng, X., *An essay on synthetic chemistry of colloidal nanocrystals.* Nano Research, 2009. **2**(6): p. 425-447.
48. Schmidt, V., Wittemann, J. V., Senz, S., & Gösele, U, *Silicon nanowires: a review on aspects of their growth and their electrical properties.* Advanced Materials, 2009. **21**(25-26): p. 2681-2702.
49. Nozik, A.J. and R. Memming, *Physical chemistry of semiconductor− liquid interfaces.* The Journal of Physical Chemistry, 1996. **100**(31): p. 13061-13078.
50. He, G., He, G., Qiao, M., Li, W., Lu, Y., Zhao, T., Zou, R., Li, B., Darr, J.A., Hu, J., Titirici, M.M. and Parkin, I.P, *S, N-Co-Doped Graphene-Nickel Cobalt Sulfide*

Aerogel: Improved Energy Storage and Electrocatalytic Performance. Advanced Science, 2017. **4**(1): p. 1600214.

51. Liu, Y., Li, Y., Kang, H., Jin, T. and Jiao, L, *Design, synthesis, and energy-related applications of metal sulfides.* Materials Horizons, 2016. **3**(5): p. 402-421.
52. Rui, X., H. Tan, and Q. Yan, *Nanostructured metal sulfides for energy storage.* Nanoscale, 2014. **6**(17): p. 9889-9924.
53. Zhang, B., Yang, G., Li, C., Huang, K., Wu, J., Hao, S., Feng, J., Peng, D. and Huang, Y., *Phase controllable fabrication of zinc cobalt sulfide hollow polyhedra as high-performance electrocatalysts for the hydrogen evolution reaction.* Nanoscale, 2018. **10**(4): p. 1774-1778.
54. Zhang, M., Yu, C., Zhao, C., Song, X., Han, X., Liu, S., Hao, C. and Qiu, J., *Cobalt-embedded nitrogen-doped hollow carbon nanorods for synergistically immobilizing the discharge products in lithium–sulfur battery.* Energy Storage Materials, 2016. **5**: p. 223-229.
55. Wu, Y., Eliyahu, J., Liu, P. and Hu, N.X., *Solvent-based inks comprising silver nanoparticles*. 2012, Google Patents.
56. Zhang, R., Cho, S., Lim, D.G., Hu, X., Stach, E.A., *Metal–metal chalcogenide molecular precursors to binary, ternary, and quaternary metal chalcogenide thin films for electronic devices.* Chemical communications, 2016. **52**(28): p. 5007-5010.
57. Bhardwaj, S. and B. Pal, *Photodeposition of Ag and Cu binary co-catalyst onto TiO_2 for improved optical and photocatalytic degradation properties.* Advanced Powder Technology, 2018. **29**(9): p. 2119-2128.
58. Fadlun, W., *Carbon Dioxide Reduction to Solar Fuels via Iron-Based Nanocomposite: Strategies to Intensify the Photoactivity.* Journal of Computational and Theoretical Nanoscience, 2020. **17**(2-3): p. 654-662.
59. Wang, L., et al., *Recent advances in ternary two-dimensional materials: synthesis, properties and applications.* Journal of Materials Chemistry A, 2017. **5**(44): p. 22855-22876.
60. DeSario, D., *The relationship between ordered intermetallic nanoparticle synthesis and the bulk phase diagram.* 2014.
61. Fan, F.-J., L. Wu, and S.-H. Yu, *Energetic I–III–VI 2 and I 2–II–IV–VI 4 nanocrystals: synthesis, photovoltaic and thermoelectric applications.* Energy & Environmental Science, 2014. **7**(1): p. 190-208.

62. Bernechea, M., Miller, N.C., Xercavins, G., So, D., Stavrinadis, A. and Konstantatos, G., *Solution-processed solar cells based on environmentally friendly AgBiS 2 nanocrystals.* Nature Photonics, 2016. **10**(8): p. 521.
63. Akgul, M.Z., Figueroba, A., Pradhan, S., Bi, Y. and Konstantatos, G, *Low-Cost RoHS Compliant Solution Processed Photovoltaics Enabled by Ambient Condition Synthesis of AgBiS2 Nanocrystals.* ACS photonics, 2020. **7**(3): p. 588-595.
64. Snaith, H., *Oxford, United Kingdom, 10 th to 12 th September 2014.*
65. Heremans, J.P., V. Jovovic, and D.T. Morelli, *Ternary thermoelectric materials and methods of fabrication*. 2009, Google Patents.
66. Paul, S., Dalal, B., Jana, R., Shit, A., Datta, A. and De, S.K., *Enhanced Photophysical Properties of $Bi_2S_3/AgBiS_2$ Nanoheterostructures Synthesized via Ag(I) Cation Exchange Mediated Transformation of Binary Bi_2S_3.* The Journal of Physical Chemistry C, 2020.
67. Rodriguez, A.N., M. Nair, and P. Nair, *Absorber Films of Ag_2S and $AgBiS_2$ prepared by Chemical Bath Deposition.* MRS Online Proceedings Library Archive, 2002. **730**.
68. Lyu, M., Yun, J.H., Chen, P., Hao, M. and Wang, L, *Addressing Toxicity of Lead: Progress and Applications of Low-Toxic Metal Halide Perovskites and Their Derivatives.* Advanced Energy Materials, 2017. **7**(15): p. 1602512.
69. Mehdaoui, L. Miloua, R., Khadraoui, M., Bensaid, M.O., Abdelkader, D., Chiker, F. and Bouzidi, A., *Theoretical analysis of electronic, optical, photovoltaic and thermoelectric properties of $AgBiS_2$.* Physica B: Condensed Matter, 2019. **564**: p. 114-124.
70. Chen, S., Qiao, X., Zheng, Z., Cathelinaud, M., Ma, H., Fan, X. and Zhang, X., *Enhanced electrical conductivity and photoconductive properties of Sn-doped Sb_2Se_3 crystals.* Journal of Materials Chemistry C, 2018. **6**(24): p. 6465-6470.
71. Mairoser, T., Loder, F., Melville, A., Schlom, D.G. and Schmehl, A., *Influence of chemical doping on the magnetic properties of EuO.* Physical Review B, 2013. **87**(1): p. 014416.
72. Barakat, M., G. Hayes, and S.I. Shah, *Effect of cobalt doping on the phase transformation of TiO_2 nanoparticles.* Journal of nanoscience and nanotechnology, 2005. **5**(5): p. 759-765.
73. Yang, J., Liu, R., Huang, S., Shao, Y., Huang, Y. and Yu, Y., *Enhanced photocatalytic activity and stability of interstitial Ga-doped CdS: combination of experiment and calculation.* Catalysis Today, 2014. **224**: p. 104-113.

74. Capasso, F., *Band-gap engineering: from physics and materials to new semiconductor devices.* Science, 1987. **235**(4785): p. 172-176.

75. Schwartz, D.A., Norberg, N.S., Nguyen, Q.P., Parker, J.M. and Gamelin, D.R., *Magnetic quantum dots: synthesis, spectroscopy, and magnetism of Co^{2+}-and Ni^{2+}-doped ZnO nanocrystals.* Journal of the American Chemical Society, 2003. **125**(43): p. 13205-13218.

76. Haller, E., *Germanium: From its discovery to SiGe devices.* Materials science in semiconductor processing, 2006. **9**(4-5): p. 408-422.

77. Chen, H.-Y., S. Maiti, and D.H. Son, *Doping location-dependent energy transfer dynamics in Mn-doped CdS/ZnS nanocrystals.* Acs Nano, 2012. **6**(1): p. 583-591.

78. Kim, K.-T. Kim, G.H., Woo, J.C. and Kim, C.I., *Characteristics of Nickel-doped Zinc Oxide thin films prepared by sol–gel method.* Surface and Coatings Technology, 2008. **202**(22-23): p. 5650-5653.

79. Goswami, N. and A. Sahai, *Structural transformation in nickel doped zinc oxide nanostructures.* Materials Research Bulletin, 2013. **48**(2): p. 346-351.

80. Elango, M. Nataraj, D., Nazeer, K.P. and Thamilselvan, M., *Synthesis and characterization of nickel doped cadmium sulfide (CdS:Ni^{2+}) nanoparticles.* Materials Research Bulletin, 2012. **47**(6): p. 1533-1538.

81. Cui, Y., Zhou, C., Li, X., Gao, Y. and Zhang, J., *High performance electrocatalysis for hydrogen evolution reaction using nickel-doped CoS_2 nanostructures: experimental and DFT insights.* Electrochimica Acta, 2017. **228**: p. 428-435.

82. Kim, S.-G., Terashi, Y., Purwanto, A. and Okuyama, K.,, *Synthesis and film deposition of Ni nanoparticles for base metal electrode applications.* Colloids and Surfaces A: Physicochemical and Engineering Aspects, 2009. **337**(1-3): p. 96-101.

83. Windmiller, L.R., *de Haas-van Alphen effect and Fermi surface in antimony.* Physical Review, 1966. **149**(2): p. 472.

84. Zhang, J., Song, L., Pedersen, S.H., Yin, H. and Iversen, B.B., *Discovery of high-performance low-cost n-type Mg_3Sb_2-based thermoelectric materials with multi-valley conduction bands.* Nature communications, 2017. **8**(1): p. 1-8.

85. Bryngelsson, H., Eskhult, J., Nyholm, L., Herranen, M., Alm, O. and Edström, K., *Electrodeposited Sb and Sb/Sb_2O_3 nanoparticle coatings as anode materials for Li-ion batteries.* Chemistry of Materials, 2007. **19**(5): p. 1170-1180.

86. Rath, T., MacLachlan, A.J., Brown, M.D. and Haque, S.A. *Structural, optical and charge generation properties of chalcostibite and tetrahedrite copper antimony sulfide*

thin films prepared from metal xanthates. Journal of Materials Chemistry A, 2015. **3**(47): p. 24155-24162.

87. Han, Q., Sun, S., Sun, D., Zhu, J. and Wang, X., *Room-temperature synthesis from molecular precursors and photocatalytic activities of ultralong Sb_2S_3 nanowires.* RSC Advances, 2011. **1**(7): p. 1364-1369.
88. Janick, P.A. and L.M. Siegel, *Electron paramagnetic resonance and optical spectroscopic evidence for interaction between siroheme and iron sulfide (Fe_4S_4) prosthetic groups in Escherichia coli sulfite reductase hemoprotein subunit.* Biochemistry, 1982. **21**(15): p. 3538-3547.
89. Gillum, W., Mortenson, L.E., Chen, J.S. and Holm, R.H., *Quantitative extrusions of the iron sulfide (Fe_4S_4*) cores of the active sites of ferredoxins and the hydrogenase of Clostridium pasteurianum.* Journal of the American Chemical Society, 1977. **99**(2): p. 584-595.
90. Heinen, W. and A.M. Lauwers, *Organic sulfur compounds resulting from the interaction of iron sulfide, hydrogen sulfide and carbon dioxide in an anaerobic aqueous environment.* Origins of Life and Evolution of the Biosphere, 1996. **26**(2): p. 131-150.
91. Kim, E.-J., Kim, J.H., Azad, A.M. and Chang, Y.S., *Facile synthesis and characterization of Fe/FeS nanoparticles for environmental applications.* ACS applied materials & interfaces, 2011. **3**(5): p. 1457-1462.
92. Henriksen, G. and D. Vissers, *Lithium-aluminum/iron sulfide batteries.* Journal of power sources, 1994. **51**(1-2): p. 115-128.
93. Geng, H., Zhu, L., Li, W., Liu, H., Quan, L., Xi, F. and Su, X., *FeS/nickel foam as stable and efficient counter electrode material for quantum dot sensitized solar cells.* Journal of Power Sources, 2015. **281**: p. 204-210.
94. Chen, H., Zhu, L., Liu, H. and Li, W., *Efficient iron sulfide counter electrode for quantum dots-sensitized solar cells.* Journal of Power Sources, 2014. **245**: p. 406-410.
95. Wang, H. and I. Salveson, *A review on the mineral chemistry of the non-stoichiometric iron sulphide, $Fe_{1-x}S$ ($0 \leq x \leq 0.125$): polymorphs, phase relations and transitions, electronic and magnetic structures.* Phase Transitions, 2005. **78**(7-8): p. 547-567.
96. Bharde, A.A., Parikh, R.Y., Baidakova, M., Jouen, S., Hannoyer, B., Enoki, T., Prasad, B.L.V., Shouche, Y.S., Ogale, S. and Sastry, M., *Bacteria-mediated precursor-dependent biosynthesis of superparamagnetic iron oxide and iron sulfide nanoparticles.* Langmuir, 2008. **24**(11): p. 5787-5794.

97. Vaughan, D.J., *Mineral chemistry of metal sulfides.* Cambridge Earth Sci. Ser., Cambridge, 1978. **493**.

98. Hobbs, D. and J. Hafner, *Magnetism and magneto-structural effects in transition-metal sulphides.* Journal of Physics: Condensed Matter, 1999. **11**(42): p. 8197.

99. Shukla, S., Loc, N.H., Boix, P.P., Koh, T.M., Prabhakar, R.R., Mulmudi, H.K., Zhang, J., Chen, S., Ng, C.F., Huan, C.H.A. and Mathews, N., *Iron pyrite thin film counter electrodes for dye-sensitized solar cells: high efficiency for iodine and cobalt redox electrolyte cells.* ACS nano, 2014. **8**(10): p. 10597-10605.

100. Li, L., Cabán-Acevedo, M., Girard, S.N. and Jin, S., *High-purity iron pyrite (FeS_2) nanowires as high-capacity nanostructured cathodes for lithium-ion batteries.* Nanoscale, 2014. **6**(4): p. 2112-2118.

101. Liang, D., Cabán-Acevedo, M., Kaiser, N.S. and Jin, S., *Gated hall effect of nanoplate devices reveals surface-state-induced surface inversion in iron pyrite semiconductor.* Nano Letters, 2014. **14**(12): p. 6754-6760.

102. Ewald, A. and E. Sinn, *Magnetically anomalous thio complexes of iron (III) and nickel (II).* Australian Journal of Chemistry, 1968. **21**(4): p. 927-938.

103. George, L. and H. Edmund, *Encyclopedia of applied physics. 4: Combustion to Diamagnetism*. 1992, VCH Publishers.

104. Deng, J., Lei, Y., Wen, S. and Chen, Z., *Modeling interactions between ethyl xanthate and Cu/Fe ions using DFT/B_3LYP approach.* International Journal of Mineral Processing, 2015. **140**: p. 43-49.

105. Akhtar, M., Alghamdi, Y., Akhtar, J., Aslam, Z., Revaprasadu, N. and Malik, M.A., *Phase controlled synthesis of copper sulfide nanoparticles by colloidal and non-colloidal methods.* Materials Chemistry and Physics, 2016. **180**: p. 404-412.

106. Sahu, M. and P. Biswas, *Single-step processing of copper-doped titania nanomaterials in a flame aerosol reactor.* Nanoscale research letters, 2011. **6**(1): p. 441.

107. Ren, C., Zhong, B., Chen, G. and Fang, W., *Effect of copper ion dopants on photocatalysis activity of titanium dioxide thin films.* Guisuanyan Xuebao(Journal of the Chinese Ceramic Society), 2006. **34**(1): p. 39-43.

108. Pan, H.-C., Shiao, M.H., Su, C.Y. and Hsiao, C.N., *Influence of sputtering parameter on the optical and electrical properties of zinc-doped indium oxide thin films.* Journal of Vacuum Science & Technology A: Vacuum, Surfaces, and Films, 2005. **23**(4): p. 1187-1191.

109. Amna, T., Hassan, M.S., Barakat, N.A., Pandeya, D.R., Hong, S.T., Khil, M.S. and Kim, H.Y., *Antibacterial activity and interaction mechanism of electrospun zinc-doped titania nanofibers.* Applied microbiology and biotechnology, 2012. **93**(2): p. 743-751.

110. Norhidayu, D., I. Sopyan, and S. Ramesh. *Development of zinc doped hydroxyapatite for bone implant applications*. in *ICCBT 2008 Conference*. 2008.

111. Cretu, V., Postica, V., Mishra, A.K., Hoppe, M., Tiginyanu, I., Mishra, Y.K., Chow, L., De Leeuw, N.H., Adelung, R. and Lupan, O., *Synthesis, characterization and DFT studies of zinc-doped copper oxide nanocrystals for gas sensing applications.* Journal of Materials Chemistry A, 2016. **4**(17): p. 6527-6539.

112. Sundararajan, M., Sailaja, V., Kennedy, L.J. and Vijaya, J.J., *Photocatalytic degradation of rhodamine B under visible light using nanostructured zinc doped cobalt ferrite: kinetics and mechanism.* Ceramics International, 2017. **43**(1): p. 540-548.

113. Hu, X., Cook, S., Wang, P. and Hwang, H.M., *In vitro evaluation of cytotoxicity of engineered metal oxide nanoparticles.* Science of the Total Environment, 2009. **407**(8): p. 3070-3072.

114. Andronic, L., Enesca, A., Vladuta, C. and Duta, A., *Photocatalytic activity of cadmium doped TiO2 films for photocatalytic degradation of dyes.* Chemical Engineering Journal, 2009. **152**(1): p. 64-71.

115. Li, Y., Guo, Y., Li, Y. and Zhou, X., *Fabrication of Cd-doped TiO_2 nanorod arrays and photovoltaic property in perovskite solar cell.* Electrochimica Acta, 2016. **200**: p. 29-36.

116. Li, X.S., Fryxell, G.E., Engelhard, M.H. and Wang, C., *The synthesis of cadmium doped mesoporous TiO2.* Inorganic Chemistry Communications, 2007. **10**(6): p. 639-641.

117. Vijayalakshmi, S., S. Venkataraj, and R. Jayavel, *Characterization of cadmium doped zinc oxide (Cd: ZnO) thin films prepared by spray pyrolysis method.* Journal of Physics D: Applied Physics, 2008. **41**(24): p. 245403.

118. Haq, B.U., R. Ahmed, and S. Goumri-Said, *DFT characterization of cadmium doped zinc oxide for photovoltaic and solar cell applications.* Solar energy materials and solar cells, 2014. **130**: p. 6-14.

119. Wang, Y., Yang, Y., Zhang, X., Liu, X. and Nakamura, A., *Optical investigation on cadmium-doped zinc oxide nanoparticles synthesized by using a sonochemical method.* CrystEngComm, 2012. **14**(1): p. 240-245.
120. Reber, J.F. and M. Rusek, *Photochemical hydrogen production with platinized suspensions of cadmium sulfide and cadmium zinc sulfide modified by silver sulfide.* The Journal of Physical Chemistry, 1986. **90**(5): p. 824-834.
121. Darwent, J.R., *H_2 Production photosensitized by aqueous semiconductor dispersions.* Journal of the Chemical Society, Faraday Transactions 2: Molecular and Chemical Physics, 1981. **77**(9): p. 1703-1709.
122. Sakata, T. and T. Kawai, *Heterogeneous photocatalytic production of hydrogen and methane from ethanol and water.* Chemical Physics Letters, 1981. **80**(2): p. 341-344.
123. Domen, K., Kudo, A., Onishi, T., Kosugi, N. and Kuroda, H., *Photocatalytic decomposition of water into hydrogen and oxygen over nickel (II) oxide-strontium titanate ($SrTiO_3$) powder. 1. Structure of the catalysts.* The Journal of Physical Chemistry, 1986. **90**(2): p. 292-295.
124. Frame, F.A., Carroll, E.C., Larsen, D.S., Sarahan, M., Browning, N.D. and Osterloh, F.E., *First demonstration of CdSe as a photocatalyst for hydrogen evolution from water under UV and visible light.* Chemical Communications, 2008(19): p. 2206-2208.
125. Nair, P.S., Radhakrishnan, T., Revaprasadu, N., Kolawole, G. and O'Brien, P., *Cadmium ethylxanthate: A novel single-source precursor for the preparation of CdS nanoparticles.* Journal of Materials Chemistry, 2002. **12**(9): p. 2722-2725.
126. Ge, M., Yue, Y., Liu, Y., Wu, J., Sun, Y., Chen, X. and Dai, N., *Facile capping CdS and ZnS shells by thermolysis of ethylxanthate precursors for CdSe/CdS/ZnS nanocrystals.* Colloids and Surfaces A: Physicochemical and Engineering Aspects, 2011. **384**(1-3): p. 574-579.
127. Devi, R.A., Latha, M., Velumani, S., Oza, G., Reyes-Figueroa, P., Rohini, M., Becerril-Juarez, I.G., Lee, J.H. and Yi, J., *Synthesis and characterization of cadmium sulfide nanoparticles by chemical precipitation method.* Journal of nanoscience and nanotechnology, 2015. **15**(11): p. 8434-8439.
128. Aqeel, M., Ikram, M., Asghar, A., Haider, A., Ul-Hamid, A., Naz, M., Imran, M. and Ali, S., *Synthesis of capped Cr-doped ZnS nanoparticles with improved bactericidal and catalytic properties to treat polluted water.* Applied Nanoscience, 2020: p. 1-11.
129. Fouad, D.E., Zhang, C., El-Didamony, H., Yingnan, L., Mekuria, T.D. and Shah, A.H., *Improved size, morphology and crystallinity of hematite (α-Fe_2O_3)*

nanoparticles synthesized via the precipitation route using ferric sulfate precursor. Results in Physics, 2019. **12**: p. 1253-1261.

130. Li, Y., Liao, H., Ding, Y., Fan, Y., Zhang, Y. and Qian, Y., *Solvothermal elemental direct reaction to CdE (E= S, Se, Te) semiconductor nanorod.* Inorganic chemistry, 1999. **38**(7): p. 1382-1387.
131. Yu, S.-H., Yang, J., Han, Z.H., Zhou, Y., Yang, R.Y., Qian, Y.T. and Zhang, Y.H., *Controllable synthesis of nanocrystalline CdS with different morphologies and particle sizes by a novel solvothermal process.* Journal of Materials Chemistry, 1999. **9**(6): p. 1283-1287.
132. Yang, J., Xue, C., Yu, S.H., Zeng, J.H. and Qian, Y.T.,*General Synthesis of Semiconductor Chalcogenide Nanorods by Using the Monodentate Ligand n-Butylamine as a Shape Controller.* Angewandte Chemie International Edition, 2002. **41**(24): p. 4697-4700.
133. Madathil, A.N.P., K. Vanaja, and M. Jayaraj. *Synthesis of ZnO nanoparticles by hydrothermal method*. in *Nanophotonic Materials IV*. 2007. International Society for Optics and Photonics.
134. Hoa, T.T.Q., The, N.D., McVitie, S., Nam, N.H., Canh, T.D. and Long, N.N., *Optical properties of Mn-doped ZnS semiconductor nanoclusters synthesized by a hydrothermal process.* Optical Materials, 2011. **33(**3): p. 308-314.
135. Pottathara, Y.B., Grohens, Y., Kokol, V., Kalarikkal, N. and Thomas, S., *Synthesis and Processing of Emerging Two-Dimensional Nanomaterials*, in *Nanomaterials Synthesis*. 2019, Elsevier. p. 1-25.
136. Qu, L., Z.A. Peng, and X. Peng, *Alternative routes toward high quality CdSe nanocrystals.* Nano letters, 2001. **1**(6): p. 333-337.
137. Peng, X., *Green Chemical Approaches toward High-Quality Semiconductor Nanocrystals.* Chemistry–A European Journal, 2002. **8**(2): p. 334-339.
138. Qu, L. and X. Peng, *Control of photoluminescence properties of CdSe nanocrystals in growth.* Journal of the American Chemical Society, 2002. **124**(9): p. 2049-2055.
139. Nyamen, L.D., N. Revaprasadu, and P.T. Ndifon, *Low temperature synthesis of PbS and CdS nanoparticles in olive oil.* Materials science in semiconductor processing, 2014. **27**: p. 191-196.
140. Nyamen, L.D., Pullabhotla, V.S.R., Nejo, A.A., Ndifon, P. and Revaprasadu, N., *Heterocyclic dithiocarbamates: precursors for shape controlled growth of CdS nanoparticles.* New Journal of Chemistry, 2011. **35**(5): p. 1133-1139.

141. Mikulec, F.V., Kuno, M., Bennati, M., Hall, D.A., Griffin, R.G. and Bawendi, M.G., *Organometallic synthesis and spectroscopic characterization of manganese-doped CdSe nanocrystals.* Journal of the American Chemical Society, 2000. **122**(11): p. 2532-2540.

142. Ji, T., W.-B. Jian, and J. Fang, *The First Synthesis of $Pb_{1-x}Mn_xSe$ Nanocrystals.* Journal of the American Chemical Society, 2003. **125**(28): p. 8448-8449.

143. Norris, D.J., Yao, N., Charnock, F.T. and Kennedy, T.A., *High-quality manganese-doped ZnSe nanocrystals.* Nano Letters, 2001. **1**(1): p. 3-7.

144. Manzoor, K., Aditya, V., Vadera, S.R., Kumar, N. and Kutty, T.R.N., *A single-source solid-precursor method for making eco-friendly doped semiconductor nanoparticles emitting multi-color luminescence.* Journal of nanoscience and nanotechnology, 2007. **7**(2): p. 463-473.

145. Shombe, G.B., Mubofu, E.B., Mlowe, S. and Revaprasadu, N., *Synthesis of hierarchical PbS nanostructures capped with castor oil.* Materials Letters, 2016. **185**: p. 17-20.

146. Nyamen, L.D., Nejo, A.A., Pullabhotla, V.S., Ndifon, P.T., Malik, M.A., Akhtar, J., O'Brien, P. and Revaprasadu, N., *The syntheses and structures of Zn (II) heterocyclic piperidine and tetrahydroquinoline dithiocarbamates and their use as single source precursors for ZnS nanoparticles.* Polyhedron, 2014. **67**: p. 129-135.

147. Zhong, H., T. Mirkovic, and G.D. Scholes, *Nanocrystal synthesis*, in *Comprehensive nanoscience and technology*. 2011, Elsevier Inc. p. 153-201.

148. Yang, Y.A., Wu, H., Williams, K.R. and Cao, Y.C., *Synthesis of CdSe and CdTe nanocrystals without precursor injection.* Angewandte Chemie International Edition, 2005. **44**(41): p. 6712-6715.

149. Kodama, T. and N. Gokon, *Thermochemical cycles for high-temperature solar hydrogen production.* Chemical Reviews, 2007. **107**(10): p. 4048-4077.

150. Frenzer, G. and W.F. Maier, *Amorphous porous mixed oxides: Sol-gel ways to a highly versatile class of materials and catalysts.* Annu. Rev. Mater. Res., 2006. **36**: p. 281-331.

151. Willmott, P., *Deposition of complex multielemental thin films.* Progress in Surface Science, 2004. **76**(6-8): p. 163-217.

152. Crouch, D., Norager, S., O'Brien, P., Park, J.H. and Pickett, N., *New synthetic routes for quantum dots.* Philosophical Transactions of the Royal Society of London. Series A: Mathematical, Physical and Engineering Sciences, 2003. **361**(1803): p. 297-310.

153. Geetha, S. and D. Trivedi, *A new route to synthesize high degree polythiophene in a room temperature melt medium.* Synthetic Metals, 2005. **155**(1): p. 232-239.
154. Roy, K.M., *Xanthates.* Ullmann's Encyclopedia of Industrial Chemistry, 2000.
155. Khan, M.D., Aamir, M., Sohail, M., Bhoyate, S., Hyatt, M., Gupta, R.K., Sher, M. and Revaprasadu, N., *Electrochemical investigation of uncapped $AgBiS_2$ (schapbachite) synthesized using in situ melts of xanthate precursors.* Dalton Transactions, 2019. **48**(11): p. 3714-3722.
156. Lang, Y., R.R. Arnepalli, and A. Tiwari, *A review on hydrogen production: Methods, materials and nanotechnology.* Journal of Nanoscience and Nanotechnology, 2011. **11**(5): p. 3719-3739.
157. Yan, Y., Xia, B.Y., Zhao, B. and Wang, X., *A review on noble-metal-free bifunctional heterogeneous catalysts for overall electrochemical water splitting.* Journal of Materials Chemistry A, 2016. **4**(45): p. 17587-17603.
158. Takanabe, K., *Photocatalytic water splitting: quantitative approaches toward photocatalyst by design.* ACS Catalysis, 2017. **7**(11): p. 8006-8022.
159. Jacobsson, T.J., *Photoelectrochemical water splitting: an idea heading towards obsolescence?* Energy & Environmental Science, 2018. **11**(8): p. 1977-1979.
160. Christopher, K. and R. Dimitrios, *A review on exergy comparison of hydrogen production methods from renewable energy sources.* Energy & Environmental Science, 2012. **5**(5): p. 6640-6651.
161. Zhang, Z., *Metal Sulfide Photocatalysts for Hydrogen Generation by Water Splitting Under Illumination of Solar Light*. 2014, Wiley Online Library. p. 165-187.
162. Iro, Z.S., C. Subramani, and S. Dash, *A brief review on electrode materials for supercapacitor.* Int. J. Electrochem. Sci, 2016. **11**(12): p. 10628-10643.
163. Sharma, K., A. Arora, and S.K. Tripathi, *Review of supercapacitors: Materials and devices.* Journal of Energy Storage, 2019. **21**: p. 801-825.
164. Li, W., B. Song, and A. Manthiram, *High-voltage positive electrode materials for lithium-ion batteries.* Chemical Society Reviews, 2017. **46**(10): p. 3006-3059.
165. Bao, S.-J., Li, C.M., Guo, C.X. and Qiao, Y., *Biomolecule-assisted synthesis of cobalt sulfide nanowires for application in supercapacitors.* Journal of Power Sources, 2008. **180**(1): p. 676-681.
166. Zhu, F., H. Xia, and T. Feng, *Nanowire interwoven $NiCo_2S_4$ nanowall arrays as promising anodes for lithium ion batteries.* Materials Technology, 2015. **30**(sup2): p. A53-A57.

167. Wang, Y., Yang, D., Zhou, T., Pan, J., Wei, T. and Sun, Y.,*Oriented $CuCo_2S_4$ nanograss arrays/Ni foam as an electrode for a high-performance all-solid-state supercapacitor.* Nanotechnology, 2017. **28**(46): p. 465402.
168. Cheng, C., Zhang, X., Wei, C., Liu, Y., Cui, C., Zhang, Q. and Zhang, D., *Mesoporous hollow $ZnCo_2S_4$ core-shell nanospheres for high performance supercapacitors.* Ceramics International, 2018. **44**(14): p. 17464-17472.
169. Huang, Y., Ge, S., Chen, X., Xiang, Z., Zhang, X., Zhang, R. and Cui, Y., *Hierarchical $FeCo_2S_4$@ $FeNi_2S_4$ Core/Shell Nanostructures on Ni Foam for High-Performance Supercapacitors.* Chemistry–A European Journal, 2019. **25**(62): p. 14117-14122.
170. Giuseppone, N., et al., *Supramolecular materials for opto-electronics*. 2014: Royal Society of Chemistry.
171. Piprek, J., *Semiconductor optoelectronic devices: introduction to physics and simulation*. 2013: Elsevier.
172. Garbovskiy, Y.A. and A.V. Glushchenko, *Liquid crystalline colloids of nanoparticles: preparation, properties, and applications,* in *Solid State Physics*. 2010, Elsevier. p. 1-74.
173. Li, L., Daou, T.J., Texier, I., Kim Chi, T.T., Liem, N.Q. and Reiss, P., *Highly luminescent $CuInS_2$/ZnS core/shell nanocrystals: cadmium-free quantum dots for in vivo imaging.* Chemistry of Materials, 2009. **21**(12): p. 2422-2429.
174. Sun, B., Xie, W., Yi, G., Chen, D., Zhou, Y. and Cheng, J., *Microminiaturized immunoassays using quantum dots as fluorescent label by laser confocal scanning fluorescence detection.* Journal of immunological methods, 2001. **249**(1-2): p. 85-89.
175. Ramadan, S., Guo, L., Li, Y., Yan, B. and Lu, W., *Hollow copper sulfide nanoparticle-mediated transdermal drug delivery.* Small, 2012. **8**(20): p. 3143-3150.
176. Li, Y., Lu, W., Huang, Q., Li, C. and Chen, W., *Copper sulfide nanoparticles for photothermal ablation of tumor cells.* Nanomedicine, 2010. **5**(8): p. 1161-1171.

Chapter Two

Facile cationic (Ag^{+}, Cd^{2+}, Cu^{2+}, Ni^{2+}, $Zn^{2+}$and Fe^{3+}) doping in CoS by a solventless route using xanthate complexes

2.1 Introduction

Recently, metal sulfides such as cobalt sulfide (CoS) have been considered as one of the most promising materials for energy applications due to their unique properties such as permeability and high specific surface areas [1, 2]. The high redox activity of cobalt sulfide is responsible for its enhanced electrochemical capacitance performance [3-5]. Likewise, it also effectively catalyzes the redox electrolytes in dye-sensitized solar cells (DSSCs), which is an indication of its suitability as a replacement for the very expensive Pt counter electrodes [6]. Thus, this efficient performance makes cobalt sulfide a promising system for energy applications. It is well-known that the synthesis of phase-pure nanostructured materials is a challenge, hence the judicious selection of precursors is crucial for the design and development of semiconductor nanoparticles [4]. Various precursor materials have been employed to prepare cobalt sulfide nanoparticles for different applications [7-10]. However, few reports have demonstrated the use of single source precursors (SSPs) for the synthesis of CoS nanoparticles as opposed to conventional multi-source precursor routes [11]. The skilful use of single source precursors is often advantageous and desirable because of the presence of preformed bonds between metal and the chalcogen atom in the same metal-organic framework [12-16]. In addition, the preparation of these metal organic precursors is comparably cost-effective, simple and does not take much time. Furthermore, the precursors are generally stable enough to be stored for a long duration for further use. Numerous studies have reported the synthesis of both CoS nanoparticles and thin films from single source precursors. Amongst them, bis(diethyldithiocarbamato)cobalt(II) complex has been reportedly used as a single source precursor to deposit CoS thin films by the drop-casting method followed by thermal treatment [17]. The films were subsequently used as counter electrodes in dye-sensitized solar cells. In another study, tris(methyl-n-hexyldithiocarbamato)cobalt(III) complex was used by O'Brien *et al* [18] to deposit $Co_{1-x}S$, CoS_2, and Co_3S_4 thin films by the alcohol catalysed chemical vapour deposition (AACVD) method. Likewise, the choice of a synthetic approach is another important aspect to consider in order to obtain a high yield of the nanoparticles with controllable phase and size. However, according to the literature survey, limited studies exist on the synthesis of transition metal doped CoS nanoparticles using the melt method. In addition, recently, the use of solvent free methods in the fabrication of nanomaterials has gained considerable attention. With the solventless approach, a precursor material is brought to decompose by the action of heat. This method is preferred over the conventional wet chemical synthesis because it is simple, scalable and avoids the use of toxic chemicals [19].

Apart from the influence of single source precursors and synthetic method on the overall properties of the material, doping of semiconductors has also been reported to improve the physicochemical properties and hence their performance in specific applications. It is interesting to note that, the choice of dopant coupled with a decent synthetic approach has considerable influence on the properties of the resulting material through controlled doping. To achieve this, the pristine material has to be doped with a small controllable amount of an impurity which in turn boosts the efficiency of the semiconductors in electronic and optoelectronic applications [20]. However, the resulting properties of the doped material depend on nature of the dopant and crystal system of the nanomaterial as well.

In this chapter, the synthesis of cobalt (II)ethylxanthate is reported. The complex was subsequently employed as a single source precursor to prepare cobalt sulfide nanoparticles by the solid state pyrolysis (melt) method. In addition, complexes of cadmium(II)ethylxanthate, zinc(II)ethylxanthate, nickel(II)ethylxanthate copper(II)ethylxanthate, silver(I)ethylxanthate and iron(III)ethylxanthate were synthesized for the purpose of doping their corresponding metal atoms (Cd, Zn, Ni, Cu, Ag and Fe) in CoS. The results for the physicochemical characterization of both the complex, pristine CoS and metal doped CoS are described in this chapter.

2.2 Methodology

2.2.1 Synthesis of Complexes

The metal-ethylxanthate complexes used in the synthesis of both pristine CoS and metal doped CoS were prepared as follows:

2.2.1.1 Synthesis of cobalt(II)ethylxanthate, [$Co(S_2COEt)_2$]

An aqueous solution of potassium ethyl xanthate (PEX) was prepared by dissolving (5.0 g, 0.0312 mmol) of xanthate in 20.0 mL of distilled water at room temperature under stirring. In another beaker, $CoCl_2$ (3.72 g, 0.0156 mmol) was dissolved in 20.0 mL of water, and added drop wise into the PEX solution under continuous stirring. Dark greenish precipitates were observed and the mixture was stirred for further 30 minutes, to allow completion of reaction. The resulting black precipitate was then collected, filtered, washed with distilled water and dried under vacuum. The elemental analysis (%) showed the presence of C (22.03%); H (3.33%); S (41.09%); Co (19.32%). The calculated values of the elements are C (23.93%); H (3.35%); S (42.50%) and Co(19.55%).

2.2.1.2 Synthesis of cadmium(II)ethylxanthate, [$Cd(S_2COEt)_2$]

An aqueous solution of potassium ethyl xanthate (PEX) was prepared by dissolving (5.0 g, 0.0312 mmol) of PEX in 20.0 mL of distilled water at room temperature under stirring. In another beaker, Cd (II) chloride (3.155 g, 0.0156 mmol) was dissolved in 20.0 ml of water and added drop-wise into the PEX solution under continuous stirring. The formation of white precipitates was observed and the mixture was stirred for further 30 minutes to allow completion of the reaction. The resulting white precipitate was then filtered, washed with distilled water and dried under vacuum. The elemental analysis (%) showed the presence of C(18.08, H(2.46), S(35.93) and Cd (31.58). The calculated values are C (20.31), H (2.84), S (36.15), and Cd (31.68).

2.2.1.3 Synthesis of Zinc(II)ethylxanthate, [$Zn(S_2COEt)_2$]

An aqueous solution of potassium ethyl xanthate was prepared by dissolving (5.0 g, 0.0312 mmols) of xanthate in 20.0 mL of distilled water at room temperature under stirring. Zinc(II)acetate (3.430 g, 0.0156 mmol) was dissolved in 20.0 mL of water in a separated beaker and the solution was added drop wise into the xanthate solution under continuous stirring. A whitish precipitate appeared and the mixture was stirred for further 30 minutes, to allow completion of reaction. The resulting white precipitate was then collected by filtration, washed

with distilled water and dried under vacuum. The elemental analysis (%) showed the presence of: C (23.03), H (3.33), S (41.19), Zn (21.33). The calculated values are C (23.41), H (3.30), S (41.70) and Zn (21.24).

2.2.1.4 Synthesis of Nickel(II)ethylxanthate, [Ni(S_2COEt)$_2$]

An aqueous solution of potassium ethyl xanthate was prepared by dissolving (5.0 g, 0.0312 mmols) of xanthate in 20.0 mL of distilled water at room temperature under stirring. In another beaker, Ni(II)chloride (3.714 g, 0.0156 mmol) was dissolved in 20.0 ml of water, and added drop-wise into the xanthate mixture under continuous stirring. The brownish precipitate formed and the mixture was stirred for a further 30 minutes, to allow completion of reaction. The resulting brown precipitate was then collected by filtration, washed with distilled water and dried under vacuum. The elemental analysis (%) showed the presence of: C (23.94), H (3.17), S(42.31) and Ni (19.39). The calculated values are C (23.93), H (3.34), S (42.59) and Ni (19.49).

2.2.1.5 Synthesis of silver(I)ethylxanthate, Ag(S_2COEt)

An aqueous solution of potassium ethyl xanthate was prepared by dissolving (5.0 g, 0.0312 mmols) of xanthate in 20.0 mL of distilled water at room temperature under stirring. In another beaker, silver(I) nitrate (5.300g, 0.0312 mols) was dissolved in 20.0 mL of water, and added drop-wise into the xanthate solution under continuous stirring. The light greenish precipitate appeared and the mixture was stirred for further 30 minutes, to allow completion of reaction. The resulting light green precipitate was then collected by filtration, washed with distilled water, dried and kept in desiccator. The elemental analysis (%) showed the presence of : C (15.82), H (2.25), S (28.2) and Ag (47.3). The calculated values are C(15.71), H(2.20), S (27.93) and Ag (47.1).

2.2.1.6 Synthesis of Iron(III)ethylxanthate, [Fe(S_2COEt)$_3$]

An aqueous solution of potassium ethyl xanthate was prepared by dissolving (5.0 g, 0.0312 mmol) of xanthate in 20.0 mL of distilled water at room temperature under stirring. In another beaker, Iron(III) chloride (2.80 g, 0.0104 mmol) was dissolved in 20.0 mL of water was and added drop-wise into the xanthate solution under continuous stirring. The blackish precipitate appeared and the mixture was stirred for further 30 minutes, to allow completion of reaction. The resulting black precipitate was then collected by filtration, washed with distilled water and dried in desiccator dish. The elemental analysis (%) showed the presence of C (25.80), H(3.61)

S(45.81) and Fe(13.32). The calculated values are C(25.77), H (3.59), S(45.88) and Fe (13.34).

2.2.1.7 Synthesis of Copper(II)ethylxanthate, [$Cu(S_2COEt)_2$]

An aqueous solution of potassium ethyl xanthate was prepared by dissolving (5.00 g, 0.0312 mmol) of xanthate in 20.0 mL of distilled water at room temperature under stirring. In another beaker, Copper (II) nitrate (3.70 g, 0.0156 mol) was dissolved in 20.0 mL of water and added drop-wise into the xanthate solution under continuous stirring. The yellowish appeared and the mixture was stirred for further 30 minutes. To allow completion of the reaction. The resulting yellow precipitate was then collected by filtration, washed with distilled water and dried under vacuum. The elemental analysis (%) showed the presence of: C (23.1), H (3.14), S (41.16) and Cu (20.74). The calculated values are C (23.57), H (3.30), S (41.86) and Cu (20.77).

2.2.2 Synthesis of CoS and metal- doped CoS nanoparticles

A stoichiometric amount of xanthate complexes of the corresponding metals was mixed and crushed to obtain a homogeneous mixture. The mixture was placed in a ceramic boat which was then placed in a glass reactor tube inside the furnace, which was then switched on and set at 250 $^{\circ}$C under inert conditions. After one hour, the furnace was switched off and allowed to cool to room temperature. The solid product was finally collected for analysis. the figure 2.1. below show step by step how the binary materials formed with the Table 2.1 showing the mass percentage used to dope dopants.

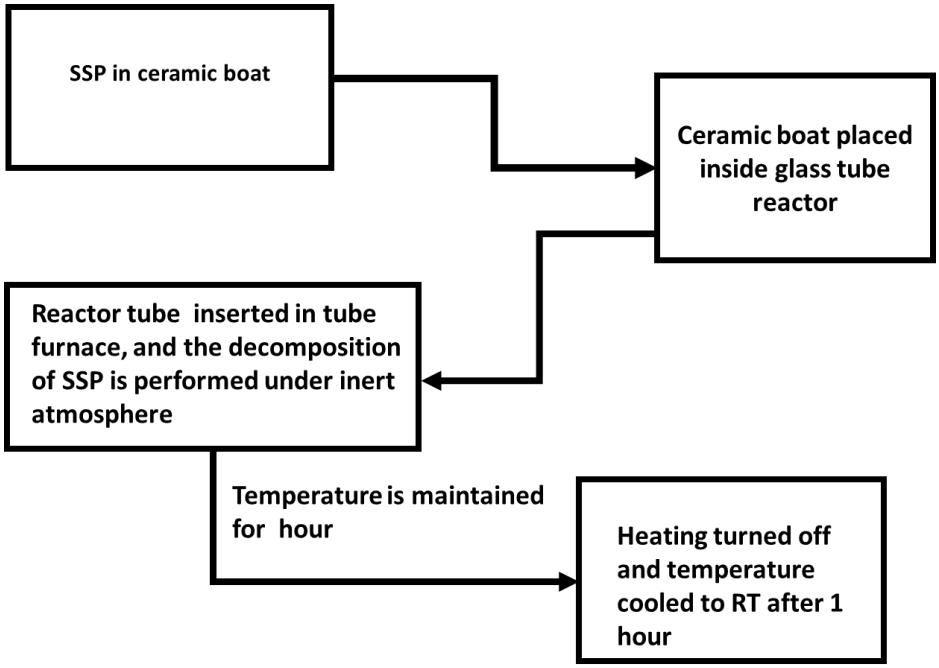

Figure 2.1: Diagrammatic representation of melt method.

Table 2.1: Stoichiometric amounts of xanthate precursors for melt method.

Material synthesized	**% of dopant**	**% of cobalt**	**Mass of dopant**	**Mass of cobalt**
CoS		100%		0.200g Co
$Co_{0.95}Cu_{0.05}S$	5%Cu	95%Co	0.01015g Cu	0.190 g Co
$Co_{0.95}Ni_{0.05}S$	5%Ni	95%Co	0.09990g Ni	0.190 g Co
$Co_{0.95}Cd_{0.05}S$	5%Cd	95%Co	0.01177g Cd	0.190 g Co
$Co_{0.95}Zn_{0.05}S$	5%Zn	95%Co	0.01021g Zn	0.190 g Co
$Co_{0.95}Fe_{0.05}S$	5%Fe	95% Co	0.01390g Fe	0.190 g Co
$Co_{0.95}Ag_{0.05}S$	5%Ag	95%Co	0.07602g Ag	0.190 g Co

2.2.3 Characterization techniques for xanthate complexes

2.2.3.1 CHNS/O analyser

Elemental microanalyses were performed on a Perkin-Elmer automated model 2400 series II for the samples' atomic composition. This technique provides a highly sensitive analysis of C, H, N, S/O present in the sample. It is mostly used to determine the complexes' purity.

2.2.3.2 Thermogravimetric analysis (TGA)

Thermogravimetric analyses were carried out at 20 ℃/min with a temperature ranging from 30 ℃ to 700 ℃ under N_2 gas and flow rate of 10 mL/min using a Perkin Elmer Pyris 6 TGA equipped with a closed perforated ceramic pan.

2.2.4 Characterization techniques for nanoparticles

2.2.4.1 Optical measurements

Optical measurements were done using a Varian Cary 50 UV–visible spectrophotometer. The samples were placed in silica cuvette (1 cm path length), using absolute ethanol as a reference solvent.

2.2.4.2 Powder X-ray diffraction (p-XRD)

Powder diffraction patterns were recorded in the high angle 2θ range of 20–70° using a Bruker AXS D8 diffractometer equipped with a nickel filtered Cu Kα radiation (λ = 1.5418 Å) at 40 kV, 40 mA and at room temperature. The scan speed and step sizes were 0.5 min^{-1} and 0.01314 respectively.

2.2.4.3 Transmission electron microscopy (TEM)

Samples were allowed to dry completely at room temperature and viewed using a JEOL 1400 TEM. Viewing was done at an accelerating voltage of 120 kV (TEM) and images captured digitally using a Megaview III camera, stored and measured using soft imaging systems iTEM software (TEM). This electron microscopy works like a slide projector which shines a beam of light through a slide and as the light passes through it, is subjected to changes by the structures and objects on the slide. The light beam is transmitted through certain parts of the slide which is then projected onto the viewing screen forming an enlarged image of the slide. In this

technique, the light source is replaced by an electron source, optical lenses by magnetic electron lenses and a detector is a phosphorescence screen or an electron multiplier.

2.2.4.4 Scanning electron microscopy (SEM) and Energy Dispersive X-ray analysis (EDX)

The SEM and EDX measurements of the as-prepared particles were performed on a Zeiss Ultra Plus FEG (at 10 kV) and Oxford detector (at 20 kV) respectively, firstly an electron gun emits a beam of electrons which passes through a condenser lens and is refined into a thin stream. The objective lens then focuses the electron beam onto the specimen. The electrons are redirected to scan the specimen in a controlled pattern called a raster. Once the electrons have hit the specimen, a series of interactions deflect secondary particles to detector and then convert the signal to voltage and amplifies it. The voltage is then applied to a cathode-ray tube and converted to an image.

2.4 Results and discussion

2.4.1 Characterization of ligands and complexes

The following are the figures and reaction formation of complexes with the confirmation of thermogravimetric analysis. The formation of cobalt (III)ethylxanthate complex is shown in equation (i) and its structure is displayed by Figure 2.3. The formation of cadmium(II)ethylxanthate complex is shown in equation (ii) and its structure is presented in Figure 2.4. The formation of Nickel(II)ethylxanthate complex is shown in equation (iii) and its structure is shown Figure 2.5, The formation of silver(I)ethylxanthate complex is shown in equation (iv) and its structure is shown Figure 2.6 The formation of Iron(v)ethylxanthate complex is shown in equation (vi) and its structure is shown Figure 2.7, The formation of Copper (II)ethylxanthate complex is shown in equation (vii) and its structure is shown Figure 2.8 and The formation of Zinc(II)ethylxanthate complex is shown in equation (viii) and its structure is shown Figure 2.9.

The thermal stability and decomposition behaviour of the synthesized CoEtX, CdEtX, NiEtX, AgEtX, FeEtX, CuEtX and ZnEtX complexes were investigated by using thermogravimetric analysis (TGA) and the results are given in Figures 2.2. The thermograms of all the complexes show clean thermal decomposition at fairly moderate temperatures. Complexes of CoEtX, CdEtX, NiEtX, AgEtX, FeEtX and CuEtX decompose in a single step while complex of ZnEtX thermalize in two steps decomposition. The second decomposition step of complex ZnEtX could be due to some sublimation of the product. The decomposition of FeEtX, CuEtX and ZnEtX complexes begin around 120 °C while those of complexes CoEtX, CdEtX, NiEtX and AgEtX begin around 150 °C accompanied by a rapid weight loss, and ends between 150 °C and 200 °C. On the other hand, complexes CoEtX and NiEtX decompose above 200 °C but below 230 °C which is a characteristic decomposition behaviour of xanthate complexes [21, 22]. The decomposition patterns of complexes CoEtX, CdEtX, NiEtX, AgEtX, FeEtX, CuEtX and ZnEtX show final weight loss of 27.5 %, 53.7 %, 27.6 %, 55.5 % ,26.6%, 32.2% and 36.5 %, respectively, which is in good agreement with the calculated percentage (figure 2.2 below) weight loss of 30.2%, 40.7%, 30.1%, 52.3%, 28.6%, 31.3% and 31.6% for CoS, CdS, NiS Ag_2S, Fe_2S_3, CuS, and ZnS, respectively.

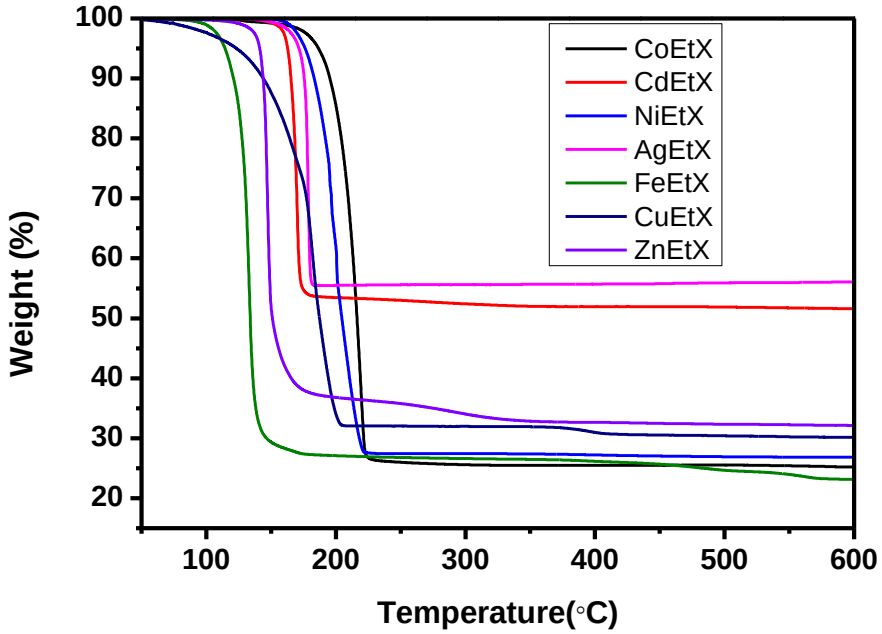

Figure 2.2: TGA profiles for CoEtX, CdEtX, NiEtX, AgEtX, FeEtX, CuEtX and ZnEtX

$$CoCl_2.6H_2O + 2C_3H_5KOS_2 \longrightarrow Co[C_3H_5OS_2]_2 + 2KCl \quad \text{(i)}$$

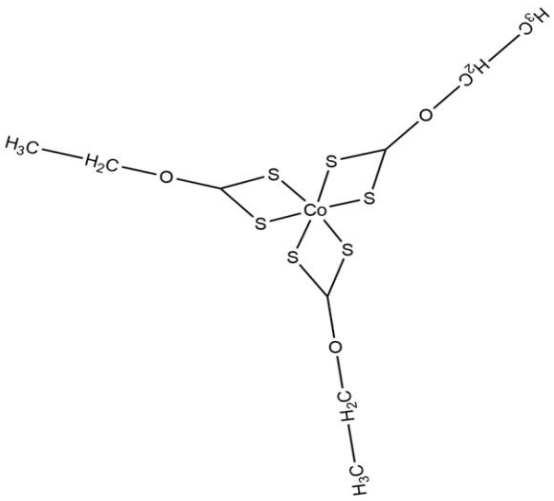

Figure 2.3: Chemical structure of cobalt(III)ethylxanthate.

$$CdCl_2.H_2O + 2C_3H_5KOS_2 \longrightarrow Cd[C_3H_5OS_2]_2 + 2KCl \quad \text{(ii)}$$

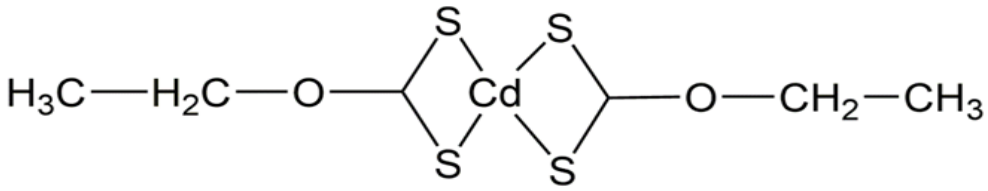

Figure. 2.4: Chemical structure of cadmium(II)ethylxanthate.

$$NiCl_2.6H_2O + 2C_3H_5KOS_2 \longrightarrow Ni[C_3H_5OS_2]_2 + 2KCl \quad \text{(iii)}$$

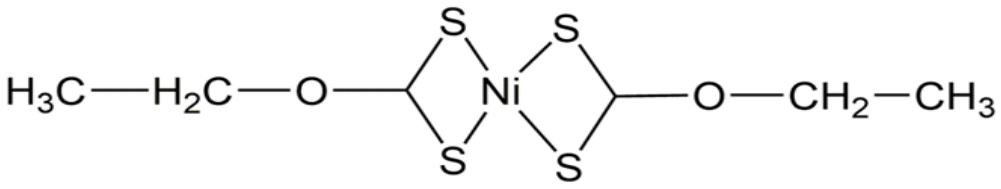

Figure 2.5: The chemical structure of Nickel(II)ethylxanthate

$$AgNO_3 + C_3H_5KOS_2 \longrightarrow Ag[C_3H_5OS_2] + KNO_3 \quad \text{(iv)}$$

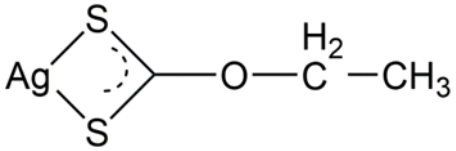

Figure 2.6: The chemical structure of silver(I)ethylxanthate

$$FeCl_3.6H_2O + 3C_3H_5KOS_2 \longrightarrow Fe[C_3H_5OS_2]_3 + 3KCl \quad \text{(v)}$$

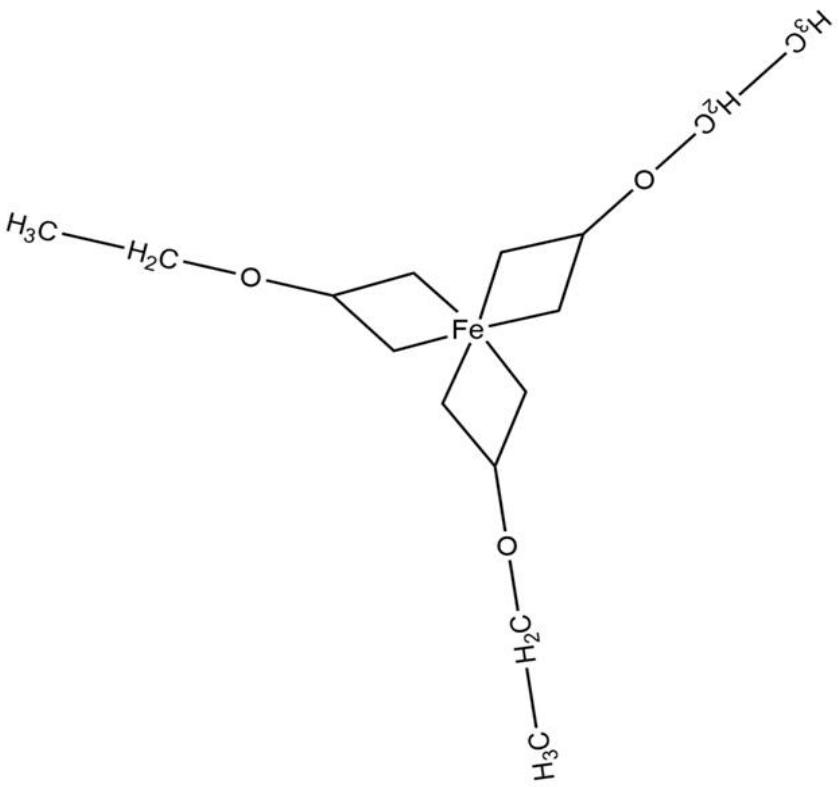

Figure 2.7: The chemical structure of Iron(III)ethylxanthate

$$Cu(NO_3).3H_2O + 2C_3H_5KOS_2 \longrightarrow Cu[C_3H_5OS_2]_2 + 2KNO_3 \quad \text{(vi)}$$

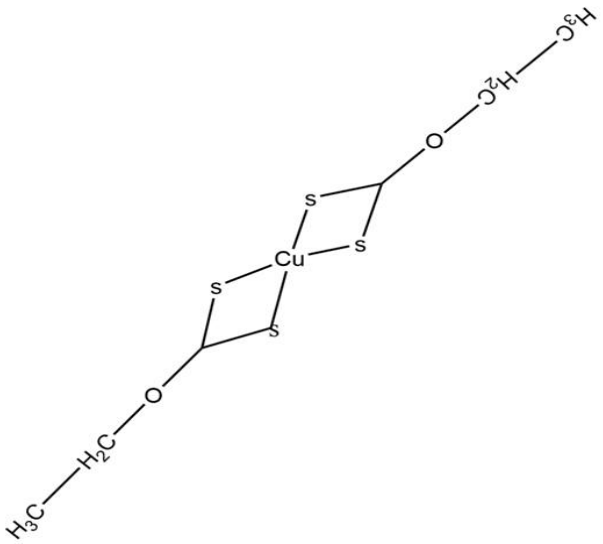

Figure 2.8: The chemical structure of Copper(II)ethylxanthate

$$Zn(CH_3CO_2.)_2.2H_2O + 2C_3H_5KOS_2 \longrightarrow Zn[C_3H_5OS_2]_2 + 2KCH_3CO_2 \quad \text{(vii)}$$

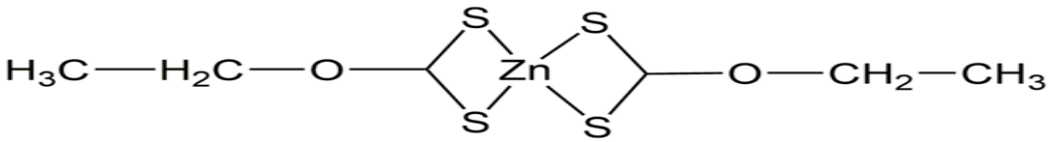

Figure 2.9: The chemical structure of Zinc(II)ethylxanthate

2.4.2 Discussion of binary systems (Ag-doped CoS).

UV-Vis analysis for CoS and Ag-doped CoS as shown in Figure 2.10 display a blue shift for all the nanoparticles between 300 nm and 400 nm when comparing CoS and Ag- doped CoS. The optical band gap energy for bulk CoS is reported to be 3.91eV[23, 24]. In this study, the band gap energies of CoS and Ag- doped CoS extrapolated from the Tauc plot (Figure 2.11) were found to be 1.60 eV and 1.58 eV, respectively. These results show a slight decrease in band gap of CoS after doping with Ag. This change in the optical band gap of CoS upon doping

with Ag^{+} may be attributed to the possible changes of crystal structure of CoS nanostructure and quantum size effect [25]. These changes in band gap values are suggestive potential application of CoS in optoelectronics.

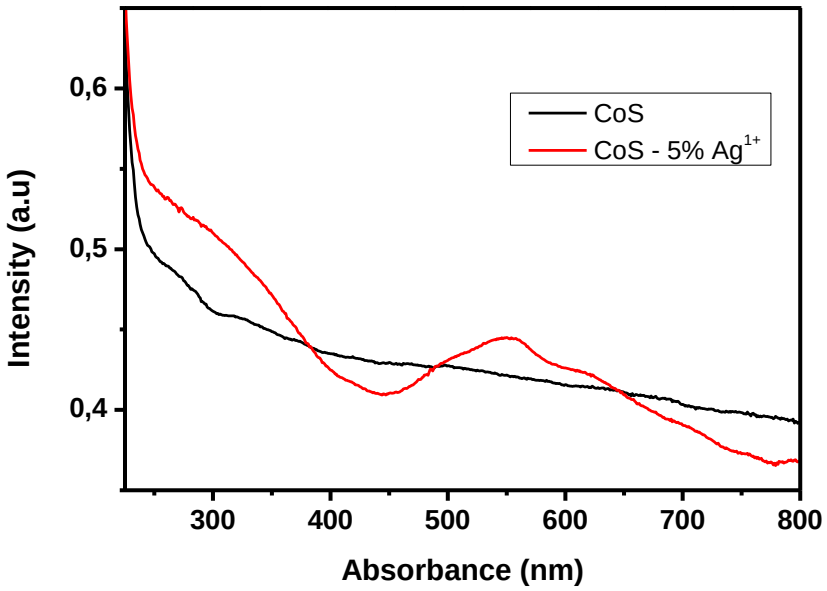

Figure 2.10: UV-vis spectra for CoS and Ag doped CoS.

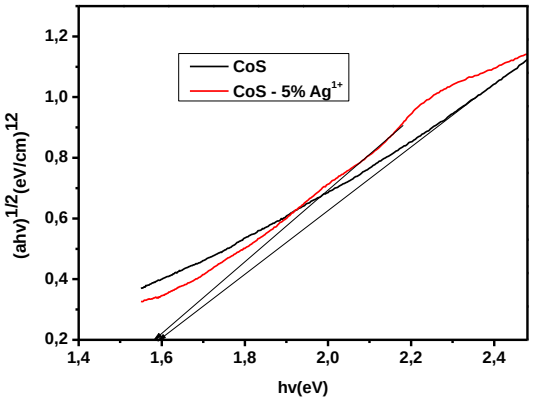

Figure 2.11: Tauc plot for CoS and Ag doped CoS.

The powder x- ray diffraction (p- XRD) peaks shown in Figure 2.12 represent the nanoparticles of CoS and Ag doped CoS formed by the solvent less pyrolysis of metal ethyl xanthate complex. Weak diffraction peaks were observed at 2θ =31.612°, 47.464°, 50.644° and 55.260° corresponding to (311), (422), (511) and (440) indices, respectively. These diffraction peaks coupled with their corresponding miller indices match well with the standard pattern of CoS

(ICDD #. 00-019-036). It is clearly seen from the XRD spectra that the visibility of the peaks corresponding to pure CoS was impaired due to amorphous nature of the sample and unexpected interference of the Cu source from the XRD instrument. Unlike CoS, the peaks corresponding to 5% Ag -doped CoS where somewhat intense accounting to its crystallinity. The particle crystalline sizes were calculated by using Scherer equation 5 and found to be 3.10 nm and 2.88 nm for CoS and Ag doped CoS, respectively.

$$D = K\lambda/B \cos\theta B \quad (5)$$

D is the coherent diffraction domain, λ is wavelength of the X-ray source applied B is the full width at half maximum (FWHM), θB is the diffraction angle and K is the scherrer's constant of the order of unity for usual crystal

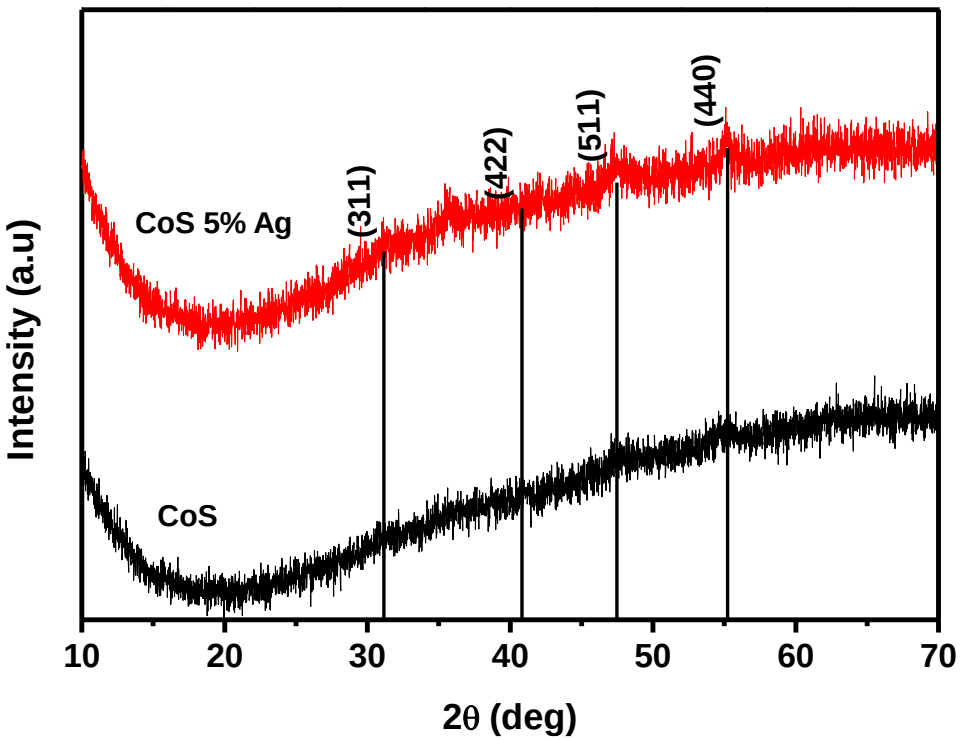

Figure 2.12: The p-XRD pattern of CoS and and 5% Ag doped CoS.

The TEM images of both pristine CoS and 5% Ag-doped CoS are shown in Figure 2.13. The undoped CoS nanoparticles shows unclear TEM image of agglomerated particles. On the other hand, the 5% Ag-doped CoS shows spherical particles with less agglomeration.

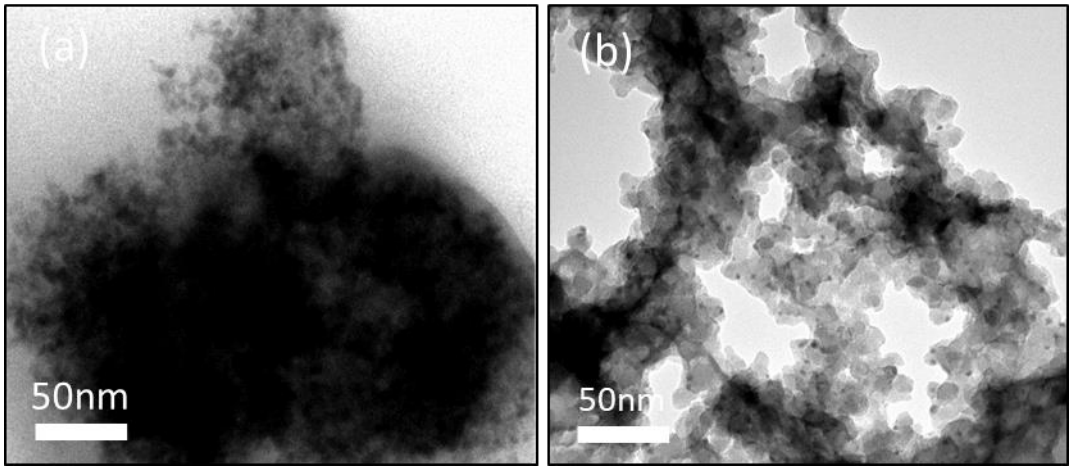

Figure 2.13: TEM images of (a) CoS undoped (b) 5% Ag doped CoS nanoparticles formed metal ethyl xanthate complex.

The selected area electron diffraction (SAED) patterns of the pristine CoS and 5% Ag doped CoS displayed in Figure 2.14 were taken at the edges of curved nano sheets. For both samples, the observed ultrathin sheets are composed of interconnected nanoparticles. The clear distinct diffraction rings indicate that all two samples are polycrystalline. In Figures 2.14 (a & b), The observed inter-planar spacing is 0.297 nm, corresponding to the (311) lattice plane of pure CoS and 5 % Ag- doped CoS due to low concentration of Ag xanthate doped, this show visible and tuning of material application while doping a higher concentration of dopant makes the material amorphous or more agglomerated. The SAED patterns shown in Figure 2.14 (a & b) could be indexed to the (440) and (311) planes of cubic phase of bare CoS and 5 % Ag doped CoS. The diffraction rings for all the above TEM-SAED data agree well with XRD results.

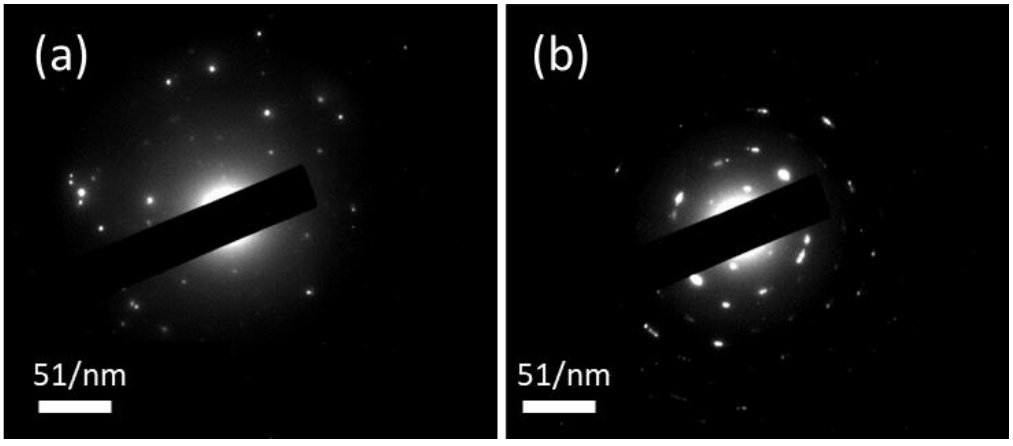

Figure 2.14: Selected area electron diffraction (SAED) images of (a) CoS (b) 5% Ag doped CoS

The analysis of surface morphologies for both CoS and 5% Ag doped CoS nanoparticles were performed by scanning electron microscopy. The SEM micrographs in Figure 2.15 indicate the formation of agglomerated particles. The EDX spectra presented in Fig, 2.16 shows that each atom in the final product is present in a stoichiometric manner, justifying that CoS and CoS 5% Ag-doped were formed without substantial loss in the amount of the starting materials. In Figure 2.15 (a) and (b) SEM mapping shows that the atoms are homogeneously distributed in the CoS and Ag-doped CoS systems.

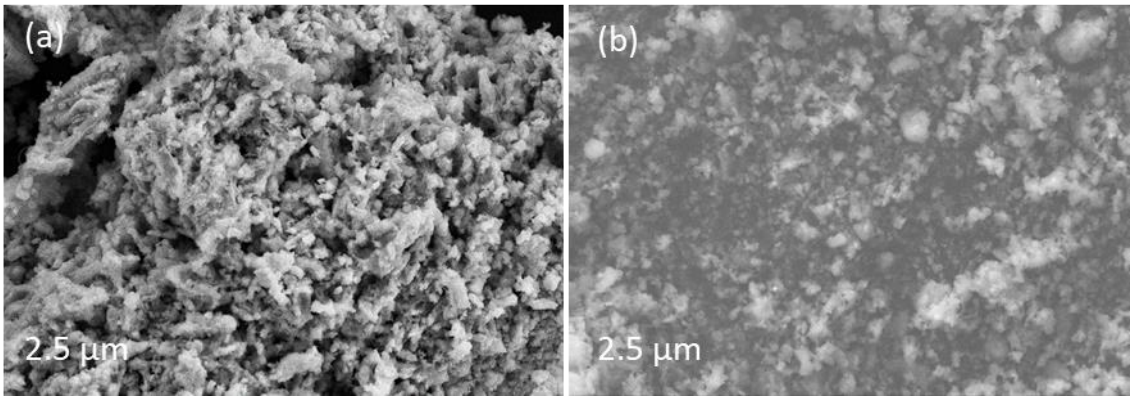

Figure 2.15: SEM images of (a) CoS (b) 5% Ag -doped CoS.

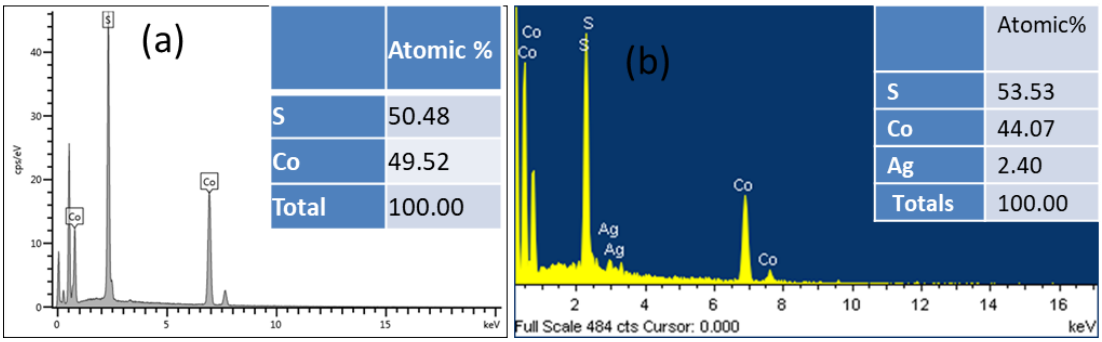

Figure 2.16: EDS images of (a) CoS (b) 5% Ag -doped CoS.

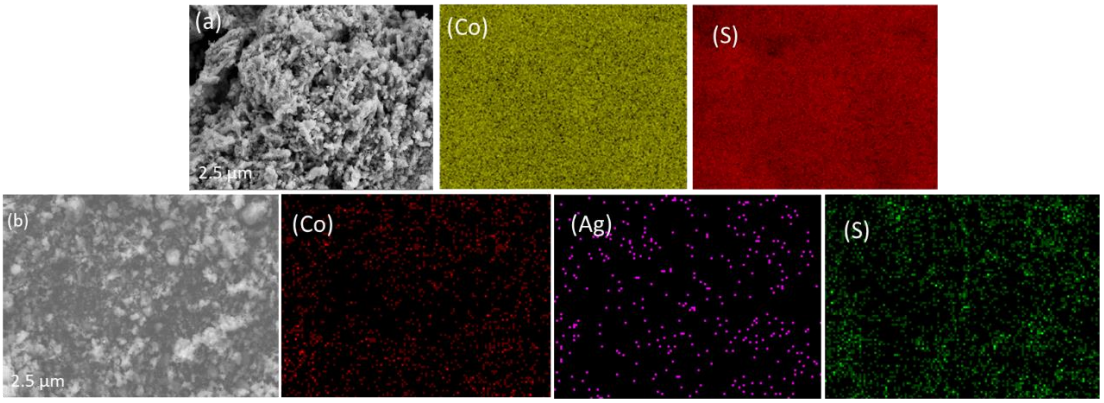

Figure 2.17: SEM mapping images of (a) CoS (b) 5% Ag doped CoS.

2.4.3 Divalent transition metals-doped CoS

In this section, doping of CoS with Ni^{2+}, Cu^{2+}, Cd^{2+}, and Zn^{2+} transition metal ions are discussed. An investigation on the properties of both bare CoS and transition metals doped CoS is presented.

The powder X-ray diffraction patterns of the pristine and transition metals-doped CoS are presented in Figure 2.20. The diffraction peaks of the nanoparticles were obtained at 2θ values of 31.612°, 47.464°, 50.644° and 55.260°. These diffraction angles can be well indexed to (311), (422), (511) and (440) indices respectively. These results are consistent with the standard diffraction pattern of CoS (ICDD #. 00-019-0367). It can be noted that there was a slight decrease in the intensity and shifting of the position of the peaks after doping CoS with transition metals. This is an indication that transition metals were able to influence the crystallinity of the pristine CoS as opposed to amorphous CoS. The crystallite particle sizes were calculated by using the Scherrer equation and found to be CoS, 3.10 nm; Cd doped CoS, 3.00 nm; Ni doped CoS, 2.90 nm; Cu doped CoS, 2.76 nm and Zn doped CoS, 2.88 nm respectively.

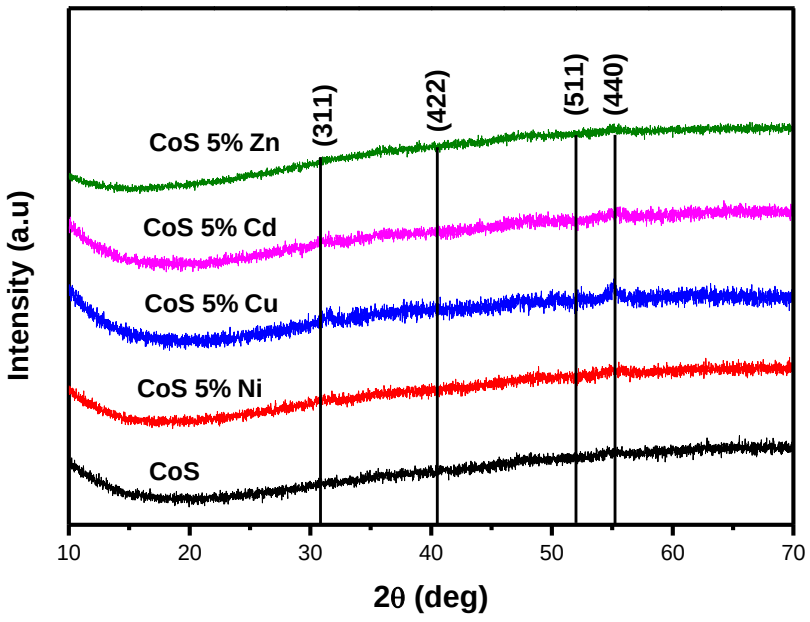

Figure 2.18: XRD patterns of CoS and transition metals- doped CoS.

TEM images of the prepared CoS and transition metals-doped CoS are displayed in Fig. 2.21. Both pristine CoS and transition metals-doped CoS show agglomerated particles. This is obvious due to the absence of capping agents during the synthesis process using the melt/solventless method.

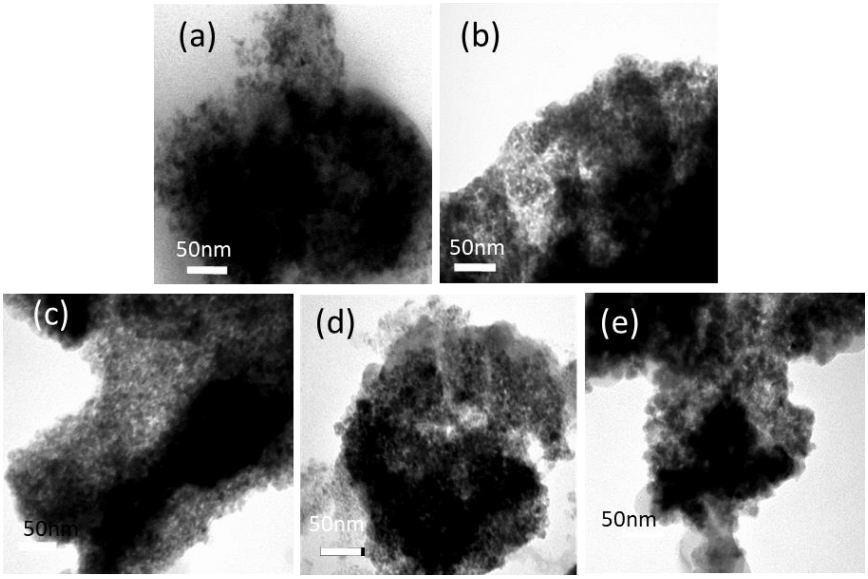

Figure 2.19: TEM images of (a) CoS (bNi doped CoS (c) Cu doped CoS (d) Cd doped CoS and (e) Zn doped CoS .

The selected area electron diffraction (SAED) patterns presented in Figure 2.22. The diffraction rings for CoS, Cu doped CoS and Cd doped CoS appear uniform and the space between them are uniform, indicating that the materials are polycrystalline in nature. On the other hand, in Ni doped CoS and Zn doped CoS some diffraction rings are not bright which may be due to the difference in the chemical nature of the dopants i.e; Ni^{2+} and Zn^{2+}. This indicate that properties of the resultant nanomaterial do not merely depend on the charge of the dopant but also on the inherent properties of the materials. For all the samples investigated, the ultrathin sheets are composed of interconnected nanoparticles. The diffraction rings for all samples are in agreement with the XRD results.

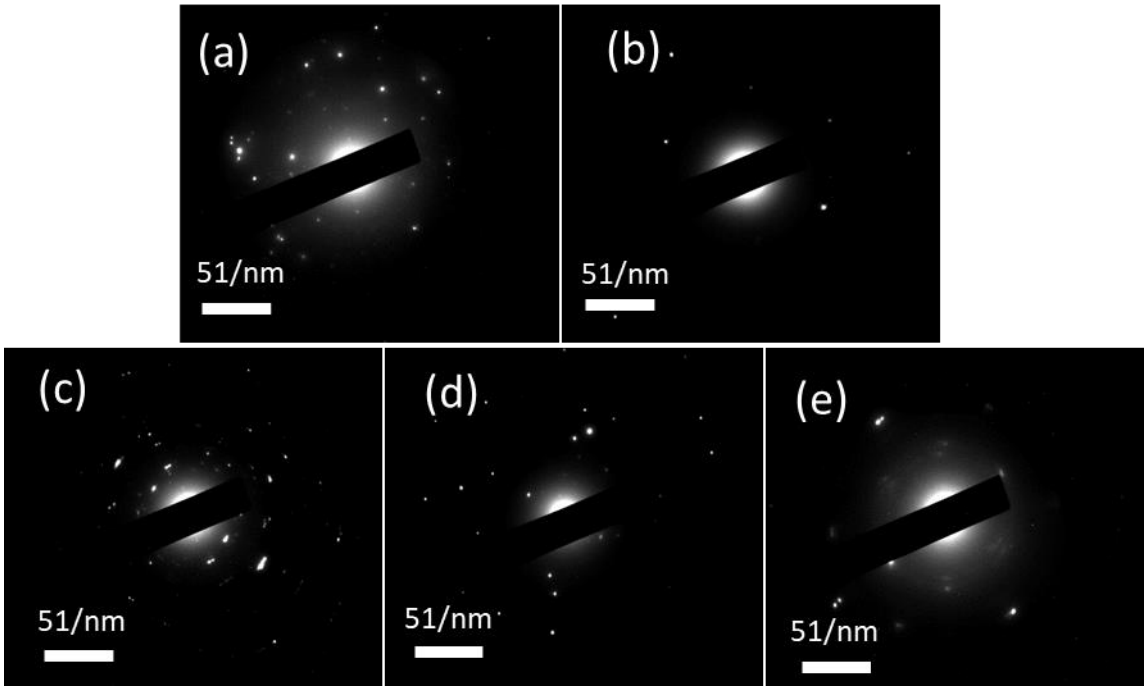

Figure.2.20: Selected area electron diffraction (SAED) images (a) CoS (b) Ni doped CoS (c) Cu doped CoS (d) Cd doped CoS (e) Zn doped CoS.

The SEM micrographs of both CoS and transition metals-doped CoS are shown in Figure 2.23. The images shows pronounced agglomeration of particles in CoS compared to transition metal doped systems. The dopants may have contributed to the reduction in agglomeration. The EDX spectra in Fig. 2.24 show the atomic percent of each atom in the system. The elemental composition of all systems are also summarized in Table 2.2. It can be seen that the experimental compositions of Co, S, Ni and Cu are in agreement with the expected compositions. On the other hand, the expected atomic percent of Zn and Cd were observed to be small compared to the values obtained from EDX. Figure 2.25 shows an even distribution of atoms in systems (b- d) while there is an uneven distribution of atoms in (e).

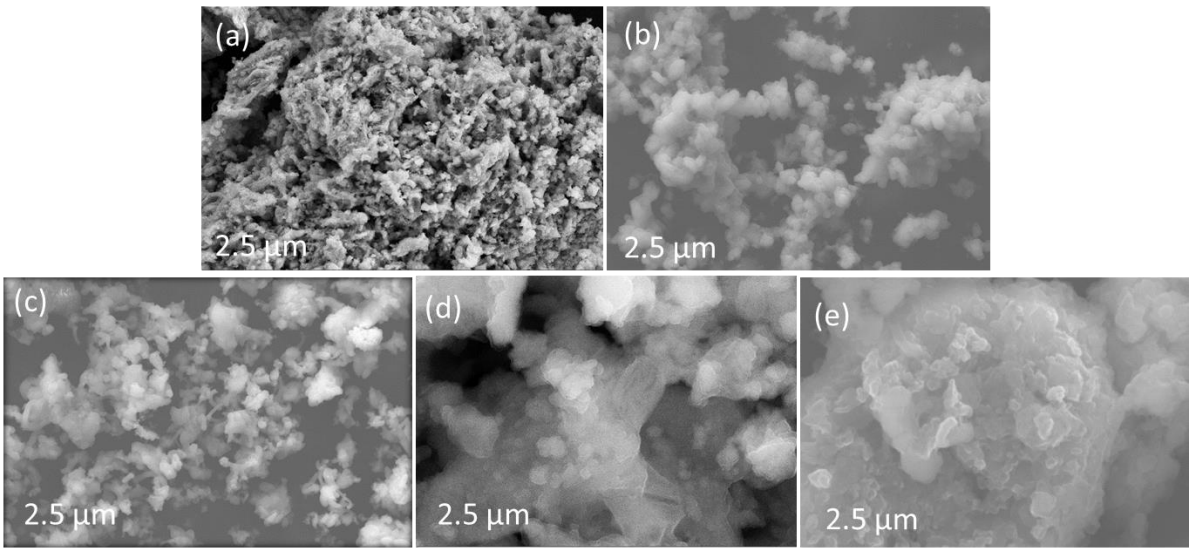

Figure 2.21: SEM images of (a) CoS (b) Ni doped CoS (c) Cu doped CoS (d) Cd doped CoS (e) Zn doped CoS .

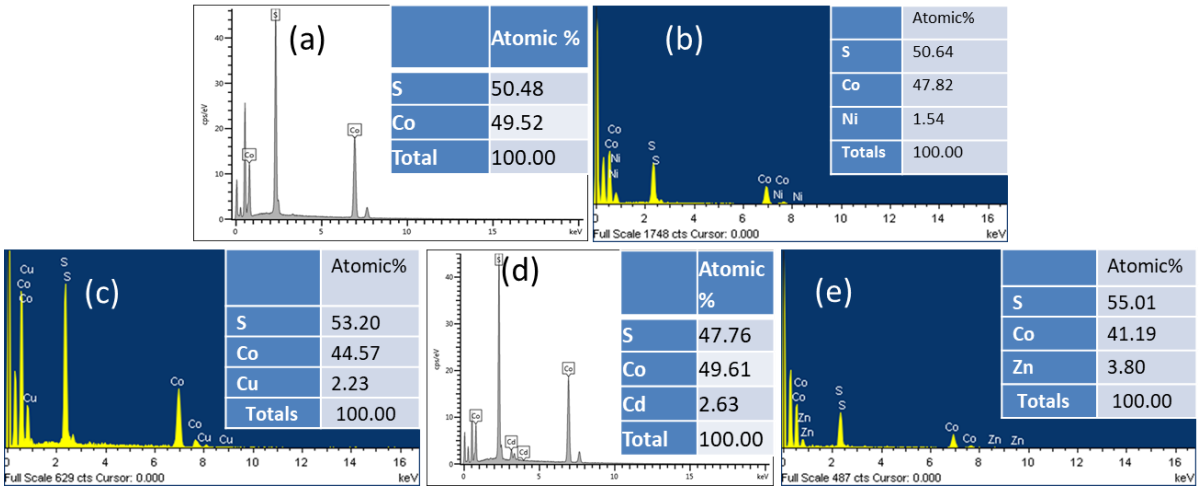

Figure 2.22: SEM EDX images of (a) CoS (b) Ni doped CoS, (c) Cu doped CoS, (d) Cd doped CoS and (e) Zn doped CoS .

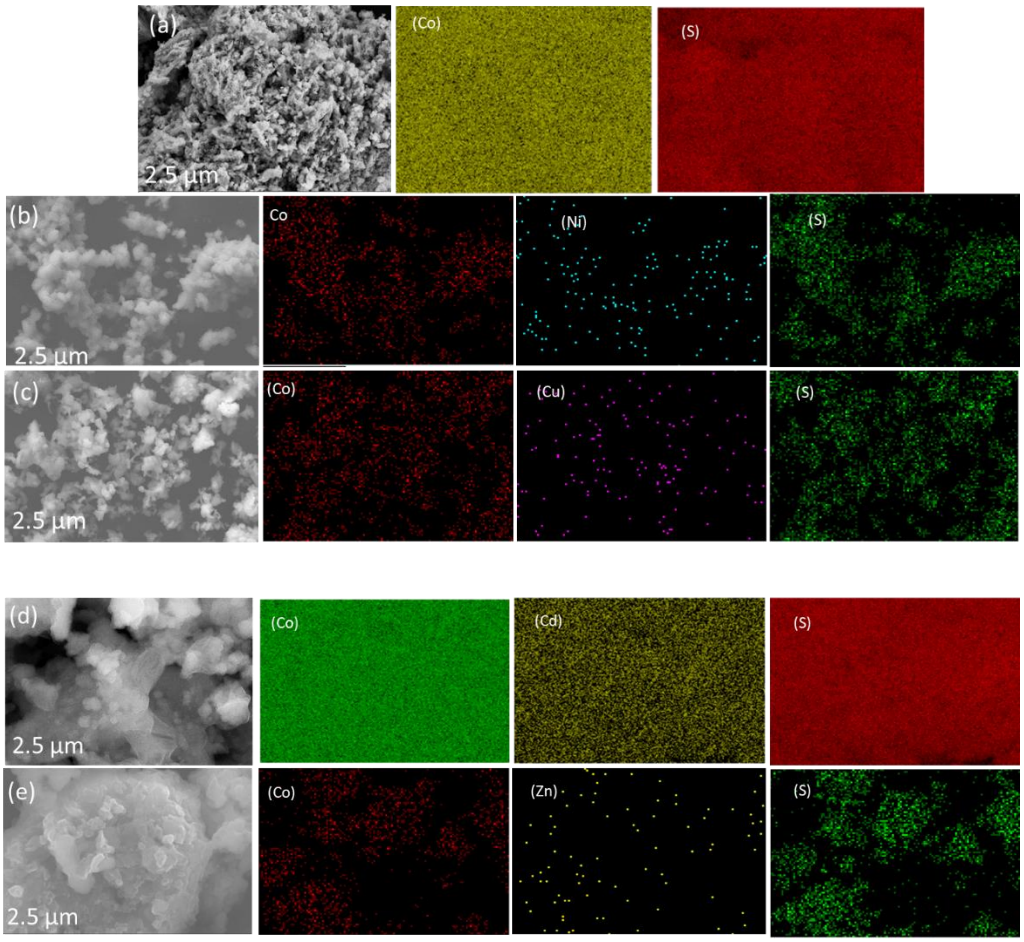

Figure 2.23: SEM mapping images of (a) CoS, (b) Ni doped CoS, (c) Cu doped CoS, (d) Cd doped CoS and (e) Zn doped CoS.

Table 2.2: Elemental composition of CoS and transition metal doped CoS.

	Undoped CoS		**$Co_{1-x}Cd_xS$**			**$Co_{1-x}Ni_xS$**			**$Co_{1-x}Cu_xS$**			**$Co_{1-x}Zn_xS$**		
	Co	S	Co	Cd	S	Co	Ni	S	Co	Cu	S	Co	Zn	S
%theoretical calculated compositions (Expected).	50	50	31.66	1.66	66.68	31.66	1.66	66.68	31.66	1.66	66.68	31.66	1.66	66.68
%composition of dopant obtained from EDS	50.48	49.52	49.61	2.63	47.76	47.82	1.54	50.64	2.23	44.57	53.20	41.19	3.80	55.01

It was observed from UV-Vis spectra shown in Fig. 2.18 that both the pristine CoS and transition metals-doped CoS nanomaterials displayed a blue shift for all the particles registering

an average absorption in the range of 200 nm and 400 nm. The band gap energy of the pristine CoS extrapolated from the Tauc plot (Figure 2.19) was found to be 1.60 eV. On the other hand, the band gap values of the transition metal-doped CoS obtained in this study are 1.58, 1.73; 1.65, and 1.71 eV for Cd, Ni, Cu and Zn doped CoS, respectively. From these results, it is obvious that the band gap of CoS increased after doping with divalent transition metals. Since, doping of transition metals was found to facilitate the reduction of crystallite size, the quantum size effect was expected to dominate in the transition metals-doped CoS nanoparticles, which resulted in a considerable enhancement in the optical band gap. Similar observations were reported by Thangavel *et al*.[26] in the study of bandgap modulation of PbS by cadmium doping.

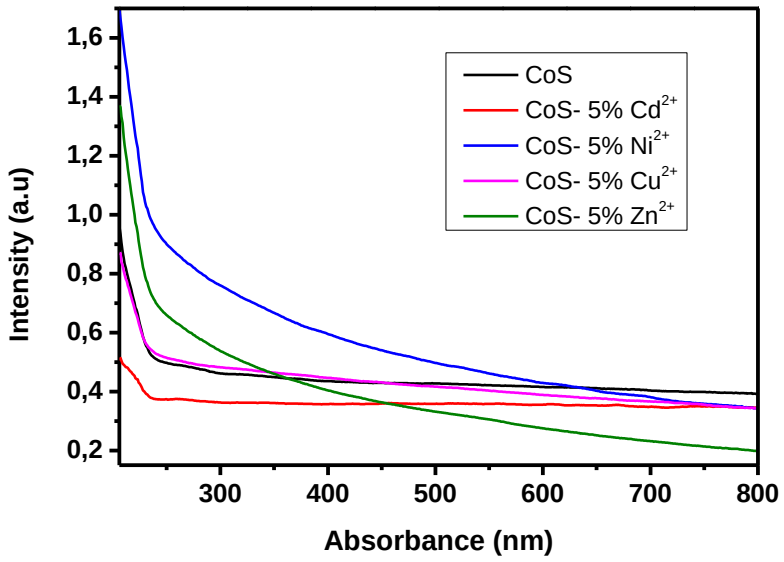

Figure 2.24: UV-Vis absorption spectra of CoS and transition metal-doped prepared by melt method.

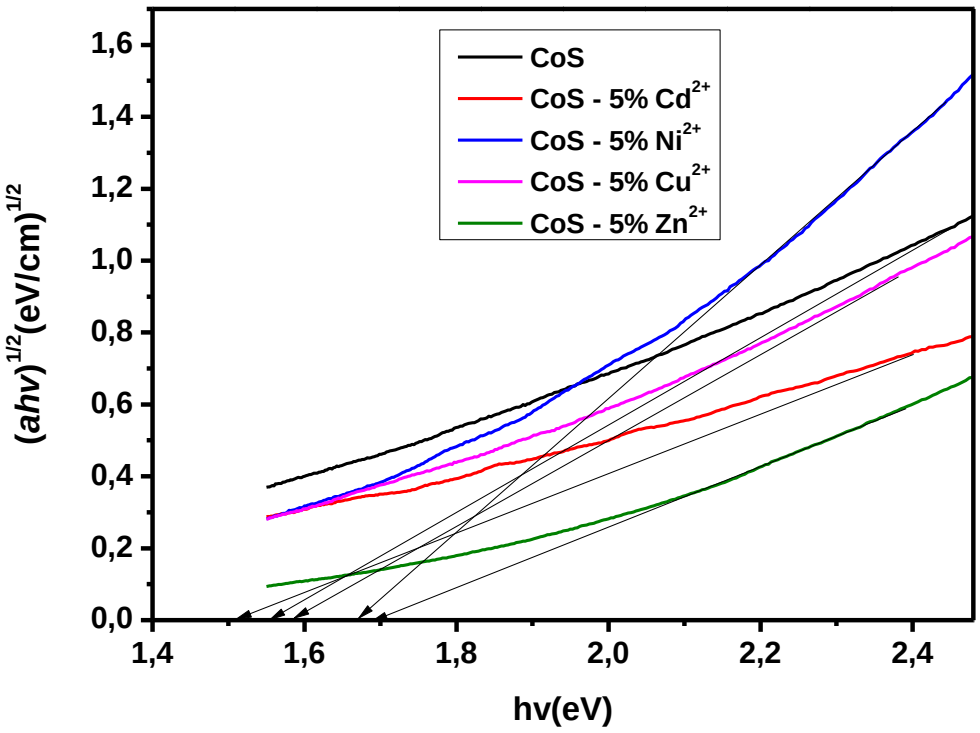

Figure 2.25: Tauc plots for CoS and transition metal-doped CoS prepared by melt.

2.4.4 Iron (Fe^{3+}) doped CoS

Figure 2.28 shows the XRD patterns of CoS and Fe doped CoS nanoparticles. The diffraction peaks obtained at 2θ values of 31.612°, 47.464°,50.644° and 55.260° can be well indexed to (311), (422), (511) and (440) hkl values, conforming to standard patterns CoS (ICDD #. 00-019-0367). The peaks are not clearly visible in pristine CoS due to the amorphous nature of the material and instrumental limitations when using the Cu source in the XRD technique. On the other hand, distinct peaks were observed in the Fe doped CoS indicating the crystalline nature of the material. The sizes were estimated from XRD diffraction data with the aid of the Scherrer equation and found to be 3.1 nm and 2.9 nm for CoS and Fe-doped CoS respectively.

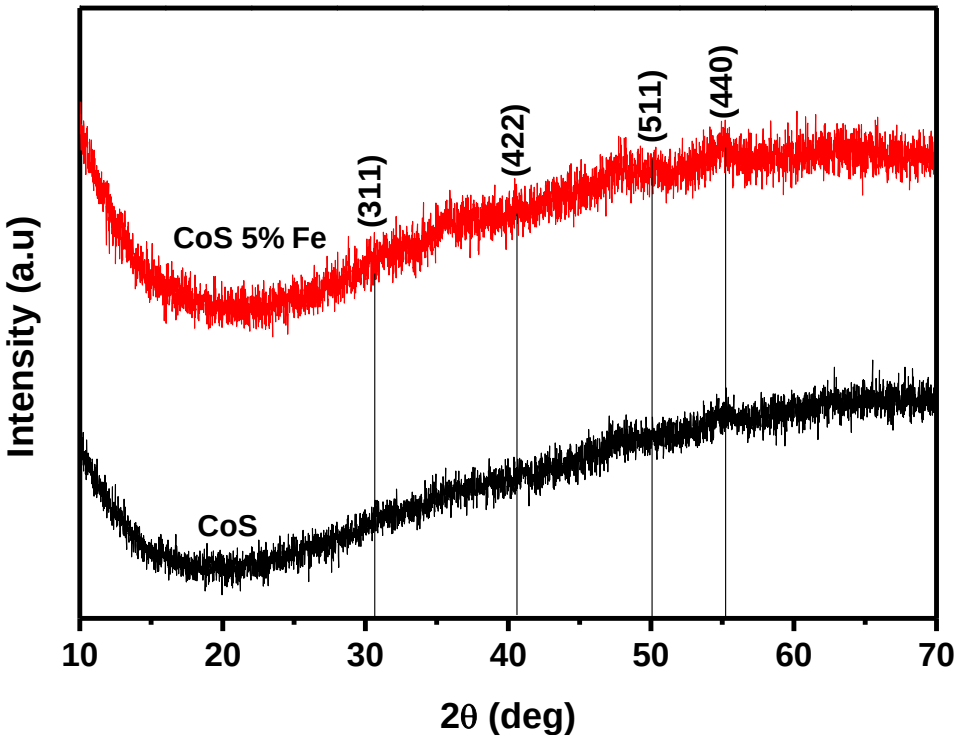

Figure 2.26: XRD pattern of the CoS and Fe doped CoS.

The TEM images of CoS and Fe doped CoS are shown in Figure 2.27. It can be observed that the particles in CoS are too close to each other and densely agglomerated while that of Fe doped CoS are somewhat dispersed although it is also difficult to identify the particle shape and size.

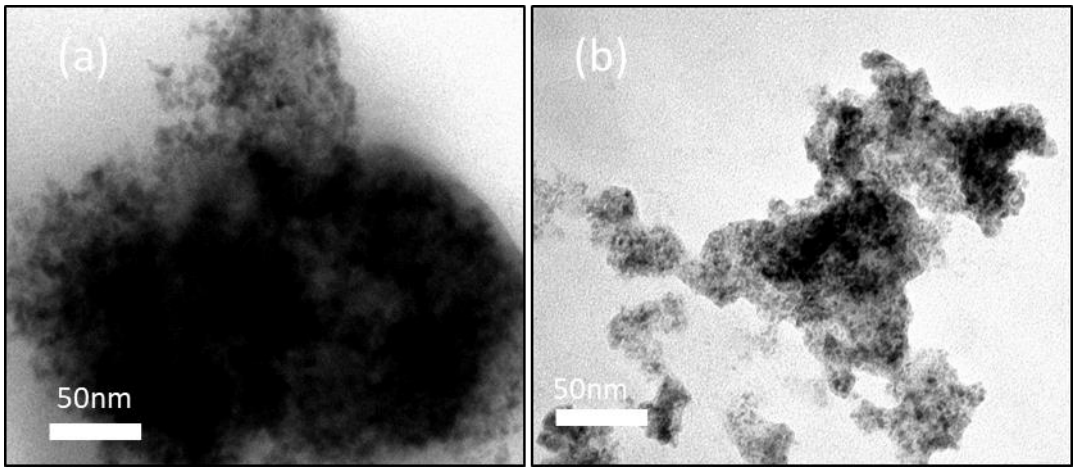

Figure 2.27: TEM images of (a) CoS (b) Fe doped CoS.

The selected area electron diffraction (SAED) patterns presented in Figure 2.28 were taken at the edges of curved nano sheets. For both samples, the ultrathin sheets are composed of interconnected nanoparticles. The clear distinct diffraction rings indicate that all two samples are polycrystalline and the diffraction rings are uniform and with equal spacing between them. This indicates that the Fe^{3+} dopant has a good influence in forming polycrystalline in CoS material. The diffraction rings for all the above SAED agree well with XRD results obtained in this study.

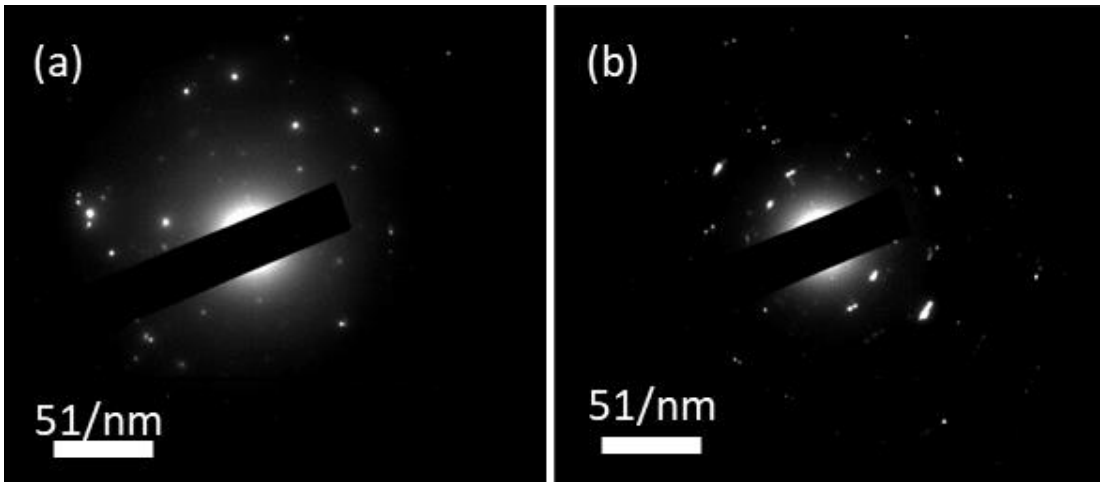

Figure. 2.28: Selected area electron diffraction (SAED) images (a) CoS (b) Fe doped CoS.

The SEM images of CoS and Fe doped CoS are displayed in Figure 2.29. Both images for CoS and Fe-doped CoS exhibit agglomerated particles. The EDX spectra in Figure 2.30 confirms the presence of the cobalt, sulphur and iron with the atomic composition of 39.83, 56.83 and 3.34 %, respectively. The experimental elemental composition obtained in EDX are close to the initial amount used during the preparation of nanoparticles. However, a slight deviation was noted in the composition of sulphur. Additionally, the images of SEM mapping in Figure 2.31 show that all atoms are evenly distributed in the CoS system.

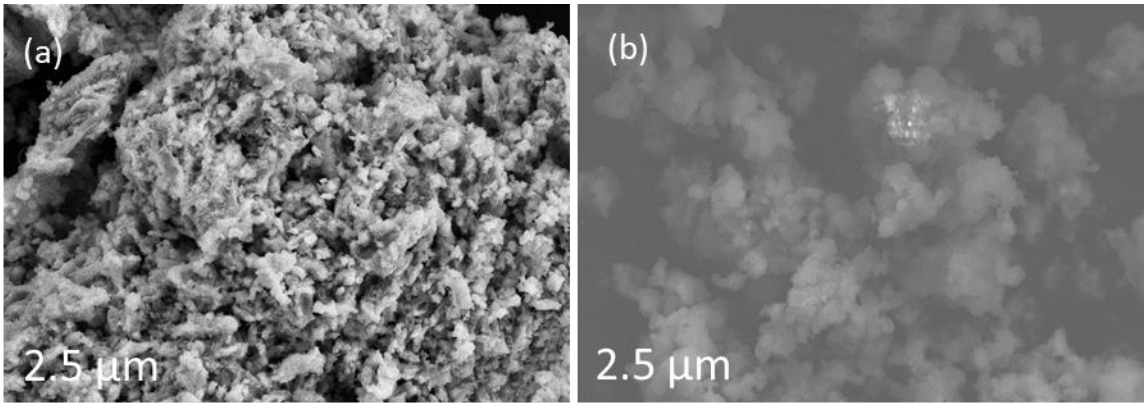

Figure 2.29: SEM images of (a) CoS, and (b) Fe doped CoS.

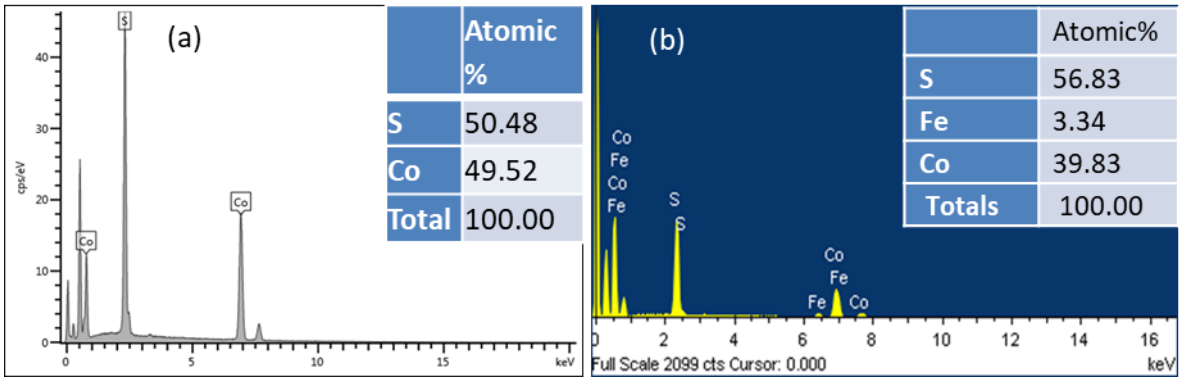

Figure 2.30: SEM- EDX images of (a) CoS (b) Fe doped CoS.

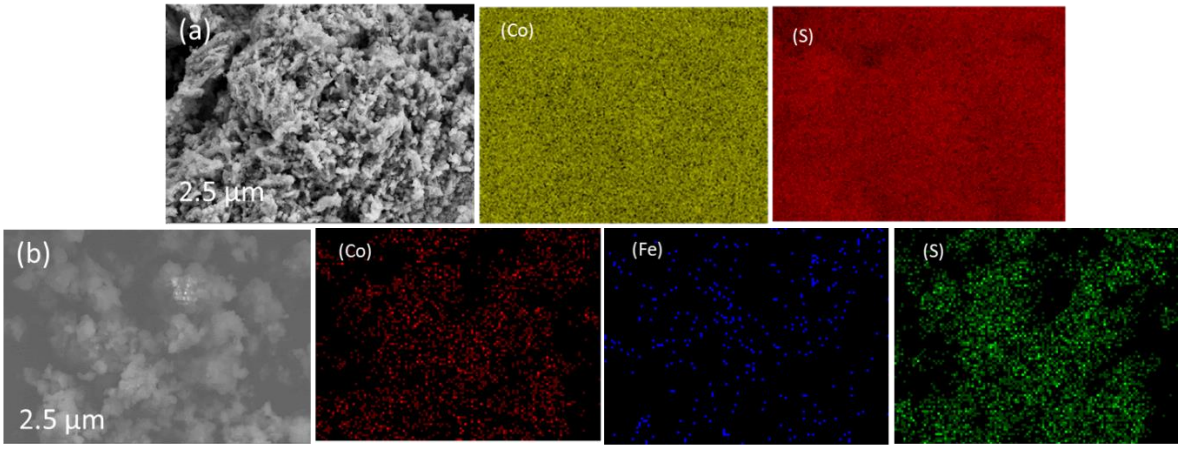

Figure 2.31: SEM mapping images of (a) CoS (b) Fe doped CoS .

The UV-Vis spectra of CoS and Fe -doped CoS are shown in Fig. 2.34. The spectra display a blue shift for both the pristine CoS and Fe-doped CoS nanoparticles at a wavelength range below 300 nm and 400 nm. From the literature, the bulk energy band gap of CoS is reported to be around 0.78-0.90 eV [23, 24]. In this study, the band gap energies extrapolated from the Tauc plots (Figure 2.35) were found to be 1.60 eV and 1.94 eV for CoS and Fe doped CoS

nanoparticles, respectively. It can be seen that the band gap energy of bare CoS is smaller than than that of Fe doped CoS obtained in this study. This increase in band gap can be explained by the quantum confinement effect [27].

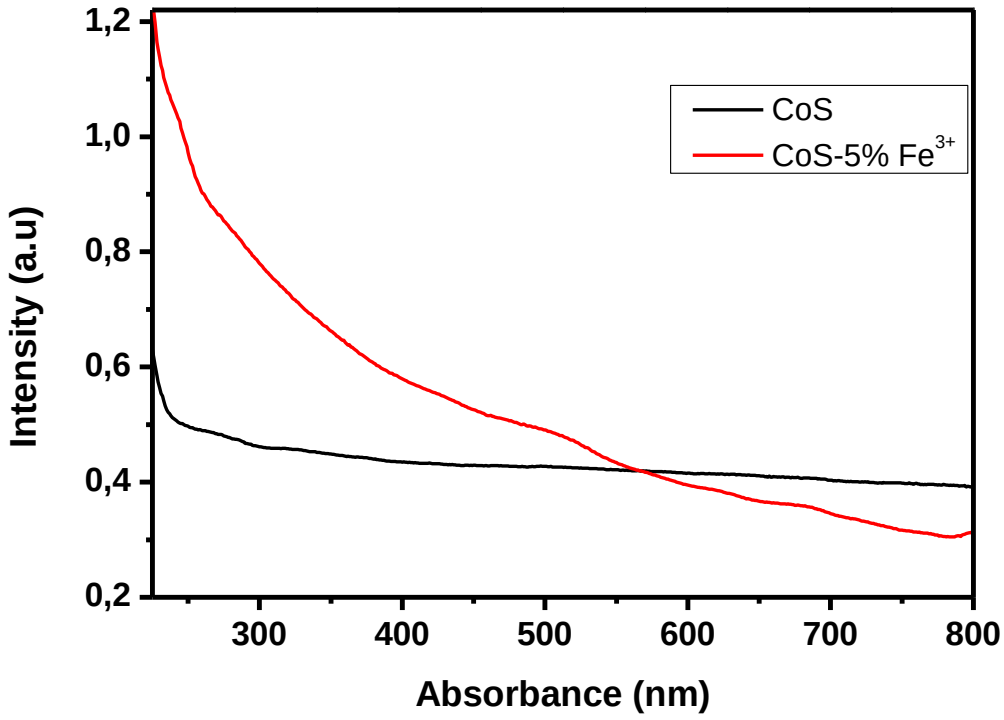

Figure 2.32: UV-vis absorption spectra of CoS and Fe doped prepared by melt method.

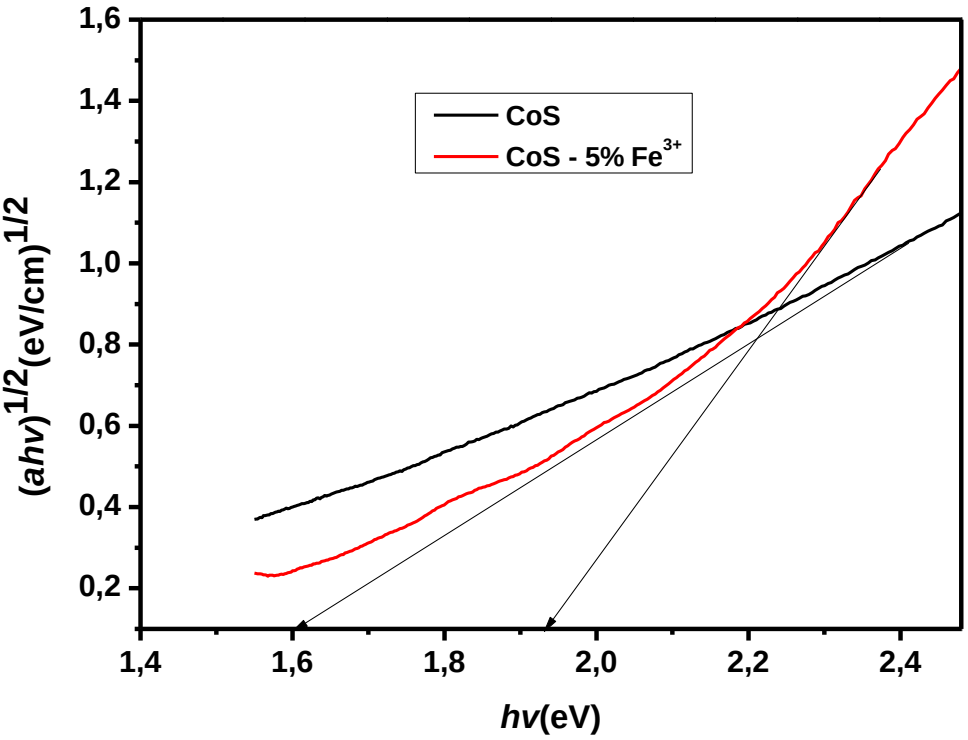

Figure 2.33: Tauc plot for of CoS and Fe doped prepared by melt method.

2.4. **Conclusion**

The melt method (the solventless approach) has been successfully employed to synthesize CoS as well as Zn^{2+}-, Cd^{2+}-, Ni^{2+}-, Fe^{3+}-, and Ag^{+}-doped CoS via pyrolysis of respective metal ethyl xanthate complexes at 250°C. The purity and crystallinity of the synthesized materials were confirmed by p-XRD analysis. The morphology of the synthesized materials was examined by TEM, in which all particles were observed to be spherical in shape. EDX analysis of the pyrolysis products confirmed the presence of only the required elements. The band gaps of the synthesized materials, as determined by Uv-vis spectroscopy, were found to be between 1.50 nm and 1.70 nm.

2.5. References

1. Huang, K.-J., Zhang, J.Z., Shi, G.W. and Liu, Y.M., *One-step hydrothermal synthesis of two-dimensional cobalt sulfide for high-performance supercapacitors.* Materials Letters, 2014. **131**: p. 45-48.
2. He, G., Qiao, M., Li, W., Lu, Y., Zhao, T., Zou, R., Li, B., Darr, J.A., Hu, J., Titirici, M.M. and Parkin, I.P., *S, N-Co-Doped Graphene-Nickel Cobalt Sulfide Aerogel: Improved Energy Storage and Electrocatalytic Performance,* Advanced Science, 2017. **4**(1): p. 1600214.
3. Yang, J., Yu, C., Fan, X., Liang, S., Li, S., Huang, H., Ling, Z., Hao, C. and Qiu, J., *Electroactive edge site-enriched nickel–cobalt sulfide into graphene frameworks for high-performance asymmetric supercapacitors.* Energy & Environmental Science, 2016. **9**(4): p. 1299-1307.
4. Huang, J. Wei, J., Xiao, Y., Xu, Y., Xiao, Y., Wang, Y., Tan, L., Yuan, K. and Chen, Y., , *When Al-doped cobalt sulfide nanosheets meet nickel nanotube arrays: a highly efficient and stable cathode for asymmetric supercapacitors.* ACS Nano, 2018. **12**(3): p. 3030-3041.
5. Liang, X., Nie, K., Ding, X., Dang, L., Sun, J., Shi, F., Xu, H., Jiang, R., He, X., Liu, Z. and Lei, Z., *Highly compressible carbon sponge supercapacitor electrode with enhanced performance by growing nickel–cobalt sulfide nanosheets.* ACS Applied Materials & Interfaces, 2018. **10**(12): p. 10087-10095.
6. Cheng, J., Fang, J.H., Li, M., Zhang, W.F., Liu, F. and Zhang, X.B., *Enhanced electrochemical performance of CoAl-layered double hydroxide nanosheet arrays coated by platinum films.* Electrochimica Acta, 2013. **114**: p. 68-75.
7. Sibokoza, S., Moloto, M.J., Moloto, N. and Sibiya, P.N.,The Effect of Temperature and Precursor Concentration on the Synthesis of Cobalt Sulfide Nanoparticles using Cobalt Diethyldithiocarbamate Complex, Chalcogenide Letters, 2017. **14**(2).
8. Bao, S.-J., Li, C.M., Guo, C.X. and Qiao, Y., *Biomolecule-assisted synthesis of cobalt sulfide nanowires for application in supercapacitors.* Journal of Power Sources, 2008. **180**(1): p. 676-681.
9. Peters, A.W., Li, Z., Farha, O.K. and Hupp, J.T., *Atomically precise growth of catalytically active cobalt sulfide on flat surfaces and within a metal–organic framework via atomic layer deposition.* ACS Nano, 2015. **9**(8): p. 8484-8490.

10. Wang, J., Bai, F., Chen, X., Lu, Y. and Yang, W., *Intercalated $Co(OH)_2$-derived flower-like hybrids composed of cobalt sulfide nanoparticles partially embedded in nitrogen-doped carbon nanosheets with superior lithium storage.* Journal of Materials Chemistry A, 2017. **5**(7): p. 3628-3637.
11. Sathiyaraj, E. and S. Thirumaran, *Structural, morphological and optical properties of iron sulfide, cobalt sulfide, copper sulfide, zinc sulfide and copper-iron sulfide nanoparticles synthesized from single source precursors.* Chemical Physics Letters, 2020. **739**: p. 136972.
12. Kadu, R., H. Roy, and V.K. Singh, *Diphenyltin (IV) dithiocarbamate macrocyclic scaffolds as potent apoptosis inducers for human cancer HEP_3B and IMR_{32} cells: synthesis, spectral characterization, density functional theory study and in vitro cytotoxicity.* Applied Organometallic Chemistry, 2015. **29**(11): p. 746-755.
13. Iornumbe, E., S. Yiase, and R. Sha'Ato, *Synthesis, Characterization and Antimicrobial Activity of Some Organotin (IV) Complexes with a Potassium Hydrogen Ethanedioate Ligand.* Int. J. Sci. Res, 2016. **5**: p. 1610-1617.
14. Hollingsworth, N., Roffey, A., Islam, H.U., Mercy, M., Roldan, A., Bras, W., Wolthers, M., Catlow, C.R.A., Sankar, G., Hogarth, G. and de Leeuw, N.H., *Active nature of primary amines during thermal decomposition of nickel dithiocarbamates to nickel sulfide nanoparticles.* Chemistry of Materials, 2014. **26**(21): p. 6281-6292.
15. Gervas, C., Mlowe, S., Akerman, M.P., Ezekiel, I., Moyo, T. and Revaprasadu, N., *Synthesis of rare pure phase Ni_3S_4 and Ni_3S_2 nanoparticles in different primary amine coordinating solvents.* Polyhedron, 2017. **122**: p. 16-24.
16. Wang, J.-Z., Chou, S.L., Chew, S.Y., Sun, J.Z., Forsyth, M., MacFarlane, D.R. and Liu, H.K., *Nickel sulfide cathode in combination with an ionic liquid-based electrolyte for rechargeable lithium batteries.* Solid State Ionics, 2008. **179**(40): p. 2379-2382.
17. Deshmukh, L. and S. Mane, *Liquid phase chemical deposition of cobalt sulphide thin films: growth and properties.* Digest Journal of Nanomaterials and Biostructures, 2011. **6**(3): p. 931-936.
18. Xiao, J., Wan, L., Yang, S., Xiao, F. and Wang, S., *Design hierarchical electrodes with highly conductive $NiCo_2S_4$ nanotube arrays grown on carbon fiber paper for high-performance pseudocapacitors.* Nano Letters, 2014. **14**(2): p. 831-838.
19. Shombe, G.B., Khan, M.D., Zequine, C., Zhao, C., Gupta, R.K. and Revaprasadu, N., *Direct solvent free synthesis of bare α-NiS, β-NiS and α-β-NiS composite as excellent*

electrocatalysts: Effect of self-capping on supercapacitance and overall water splitting activity. Scientific Reports, 2020. **10**(1): p. 1-14.

20. Ekimov, A.I. and A.A. Onushchenko, *Quantum size effect in three-dimensional microscopic semiconductor crystals.* JETP Letters, 1981. **34**(6): p. 345-349.
21. Khan, M.D., Aamir, M., Sohail, M., Bhoyate, S., Hyatt, M., Gupta, R.K., Sher, M. and Revaprasadu, N.,*Electrochemical investigation of uncapped $AgBiS_2$ (schapbachite) synthesized using in situ melts of xanthate precursors.* Dalton Transactions, 2019. **48**(11): p. 3714-3722.
22. Kaltenhauser, V., Rath, T., Haas, W., Torvisco, A., Müller, S.K., Friedel, B., Kunert, B., Saf, R., Hofer, F. and Trimmel, G., *Bismuth sulphide–polymer nanocomposites from a highly soluble bismuth xanthate precursor*. Journal of Materials Chemistry C, 2013. **1**(47): p. 7825-7832.
23. Sohrabnezhad, S., A. Pourahmad, and M. Zanjanchi, *Incorporation of CoS nanoparticles into ZSM-5 zeolite by hydrothermal and ion exchange methods.* Journal of the Iranian Chemical Society, 2009. **6**(3): p. 612-619.
24. Ochbelagh, D.R., Sohrabnezhad, S., Biroon, M.K. and Golboos, N.M., *Study of neutron irradiation on CoS nanoparticles grown on AlMCM-41 matrix.* Spectrochimica Acta Part A: Molecular and Biomolecular Spectroscopy, 2012. **92**: p. 245-249.
25. Sivakumar, S., Venkatesan, A., Soundhirarajan, P. and Khatiwada, C.P., *Synthesis, characterizations and anti-bacterial activities of pure and Ag doped CdO nanoparticles by chemical precipitation method.* Spectrochimica Acta Part A: Molecular and Biomolecular Spectroscopy, 2015. **136**: p. 1751-1759.
26. Thangavel, S., Ganesan, S., Chandramohan, S., Sudhagar, P., Kang, Y.S. and Hong, C.H., *Band gap engineering in PbS nanostructured thin films from near-infrared down to visible range by in situ Cd-doping.* Journal of Alloys and Compounds, 2010. **495**(1): p. 234-237.
27. Chamarro, M., Voliotis, V., Grousson, R., Lavallard, P., Gacoin, T., Counio, G., Boilot, J.P. and Cases, R., *Optical properties of Mn-doped CdS nanocrystals.* Journal of Crystal Growth, 1996. **159**(1-4): p. 853-856.

Chapter three

Facile cationic (Cu^{2+}, Sb^{3+} and Fe^{3+}) doping in $AgBiS_2$ by solventless route using xanthate complexes

3.1 Introduction

Semiconductor materials are an important class of materials due to their applications in everyday life such as telecommunications [1], energy [2-4] and transportation. The world is facing challenges not only in energy production but also in environmental pollution generated by the use of non-renewable energy sources [5]. Though nuclear energy production can be fruitful in fulfilling the energy demands, dealing with nuclear waste is a major issue [6].Therefore in a quest to find alternative sources of energy, the approach should be to investigate materials that are not only energy efficient but also environmentally benign. In this regard, semiconductors are important materials that are potential candidates in both energy generating and energy storage devices [7-10]. These semiconducting materials can be further classified as binary or multinary (ternary, quaternary) semiconductors [11-13]. The use of ternary or quaternary metal chalcogenide semiconductors are comparatively more advantageous over binary semiconducting materials, as they offer better flexibility in tuning the desired properties and also the synergistic effect from multi-components can enhance the performance multi-fold [12, 14-16]. Ternary metal chalcogenide semiconductors (I-IV-VI) may exist in different phases however a simple and important class of ternary materials is chalcopyrite type materials. Chalcopyrites can be represented by a general formula of ABX_2, where A is a monovalent cation, B is a trivalent cation and X is chalcogenide (S, Se, Te) atom.

Silver bismuth sulfide ($AgBiS_2$) is an example of the chalcopyrite family, with suitable semiconducting properties [17-20]. This chalcopyrite has been used in optoelectric and thermoelectric devices including optical recording media [19, 21, 22]. Furthermore, it is composed of non-toxic and earth abundant elements, which makes it an environmentally friendly material.

$AgBiS_2$ has been synthesised by different methods, such as microwave method [17], flux techniques [22] solvothermal [23],[24] and cyclic microwave techniques [24]. Nevertheless, these synthetic methods require toxic organic agents, prolonged heating and duration or expensive substrates to prepare thin films. There are very limited reports on use of metal organic precursors for the synthesis of $AgBiS_2$ nanomaterials [25].

The melt method is a solventless, scalable method that can be used to upscale the synthesis of $AgBiS_2$ at comparatively much lower temperatures. The absence of any solvent makes it more cost effective and a comparatively greener route. Various materials such as CuS

nanorods [26], mono dispersed Ag_2S [27], Bi_2S_3 nanorods and nanowires [28], Cu_2S nano disks [29], NiS nano rods and triangular nano prisms [30] have been synthesised by the solventless method.

Amongst the different precursors, the use of xanthate complexes is advantageous as they have a low decomposition temperature and the by-products are volatile easily leaving behind a pure crystalline product. [31-35] More importantly, various metal sulfide nanomaterials with controllable size and morphology have been prepared from the corresponding xanthate precursors through solvothermal[36-39] or solvent-less thermolysis routes [40]. Bulk $AgBiS_2$ has an energy band gap of $E_g = \sim 1.2$ eV [41], which is close to the optimal gap (1.39 eV) for a solar absorber, [40] and it also has a high absorption coefficient of $\alpha = \sim 105$ cm^{-1} (at λ = 600 nm) [42]. These two features give $AgBiS_2$ the potential to be utilized for a high-efficiency solar absorbers [19, 40, 43]. Similarly, the electrochemical properties also indicates its potential as a supercapacitor material. The efficiency of $AgBiS_2$ is expected to be altered by substituting Ag or Bi with other cations. In this study we have incorporated Cu, Sb and Fe into $AgBiS_2$ in different ratios (i.e. 5%, 10% and 15%) to form $Ag_{1-x}Cu_xBiS_2$, $AgSb_xBi_{1-x}S_2$ and $AgFe_xBi_{1-x}S_2$. The dopants are also abundant in nature, non-toxic and can have a synergistic effect on the properties of $AgBiS_2$.

3.2 Synthesis of xanthate precursors for $AgBiS_2$/metal doped $AgBiS_2$

As stated earlier xanthate precursors are advantageous to use as compared to the other metal organic precursors. The synthesis of various xanthate precursors and their use in preparation of binary or ternary metal sulphides is well established. Similarly, xanthate precursors have been used successfully to prepare ternary metal chalcogenides by the solventless route as well[40]. In this study, the ternary system, $AgBiS_2$ has been doped with different cations (Cu^{2+}, Sb^{3+} and Fe^{3+}) with varying concentrations (5, 10 and 15%).

3.2.1 Synthesis of Potassium ethyl xanthate

Ethanol (60 mL) and potassium hydroxide (0.9600g, 40.0 mL) were mixed and the reaction mixture was stirred at room temperature. Upon dissolution of KOH, the mixture was then cooled in ice bath, followed by the slow addition of carbon disulphide. The reaction mixture was stirred for half an hour and the precipitate was filtered, washed with diethylether and dried under vacuum.

3.2.2 Synthesis of metal complexes from potassium ethyl xanthate

3.2.2.1 Synthesis of silver(I)ethylxanthate, $Ag(S_2COEt)$ (AgEtX):

Silver(I) nitrate (5.300g, 0.0312 mol) in 20.0 mL of water was added drop-wise to the ethanolic solution of potassium ethyl xanthate (5.0 g, 0.0312 mol), and the mixture was stirred for one hour. The resulting light green colored precipitate was then collected by filtration, washed with distilled water and dried in vacuum. Yield: 5.2 g, 77 %. Elemental analysis: Found (%): C, 15.82; H, 2.25; S, 28.2; Ag, 47.3 %. Calc. C, 15.71; H, 2.20; S, 27.93; Ag, 47.1%.

3.2.2.2 Synthesis of Copper(II)ethylxanthate, $[Cu(S_2COEt)_2]$ (CuEtX):

Copper(II) nitrate (3.70 g, 0.0156 mol) in 20.0 mL of water was added drop-wise to the aqueous solution of potassium ethyl xanthate (5.0 g, 0.0312 mol), and the mixture was stirred for one hour. The resulting yellow precipitate was then collected by filtration, washed with distilled water and dried in vacuum. Elemental analysis: Found (%): C, 23.1%; H, 3.14%; S, 41.16%. Calc. C, 23.57%; H, 3.30%; S, 41.86%.

3.2.2.3 Synthesis of Antimony(III)ethylxanthate, [Sb(S_2COEt)$_3$](SbEtX):

Antimony(III) chloride (2.40 g, 0.0104 mol) in 20.0 mL of methanol was added drop-wise to the aqueous solution of potassium ethyl xanthate (5.0 g, 0.0312 mol), and the mixture was stirred for one hour. The resulting pale yellow precipitate was then collected by filtration, washed with methanol and dried in vacuum. Yield: (3.2 g) 79%, m. p. 90.3 ºC, elemental analysis: found (%): C, 22.61; H, 3.07; S, 39.71; Sb, 24.15; calc. (%) C, 22.25; H, 3.11; S, 39.55; Sb, 25.08.

3.2.2.4 Synthesis of Bismuth(III)ethylxanthate, [Bi(S_2COEt)$_3$](BiEtX):

Bismuth(III) chloride (3.30 g, 0.0104 mmol) in 20.0 mL of methanol was added drop-wise to the aqueous solution of potassium ethyl xanthate (5.0g, 0.0312 mmols), and the mixture was stirred for one hour. The resulting yellow precipitate was then collected by filtration, washed with methanol and dried in vacuum. Yield (3.8 g, 80%), m.p. 110 ºC, elemental analysis: found (%): C, 19.14; H, 2.65; S, 33.46; Bi, 36.47; calc. (%) C, 18.86; H, 2.64; S, 33.53; Bi, 36.49.

3.2.2.5 Synthesis of Iron(III)ethylxanthate, [Fe(S_2COEt)$_3$] (FeEtX):

Iron(III) chloride (2.80 g, 0.0104 mmol) in 20.0 mL of water was added drop-wise to the aqueous solution of potassium ethyl xanthate (5.0 g, 0.0312 mmol), and the mixture was stirred for one hour. The resulting black precipitate was then collected by filtration, washed with distilled water and dried in vacuum. Yield (3.9 g, 86 %), m.p (118℃) elemental analysis: found (%): C, H, S, Fe; Calc. (%) C, 25.80; H, 3.61; S, 45.81; Fe, 13.32.

3.2.3 Solventless synthesis of $AgBiS_2$ and metal doped $AgBiS_2$

For $AgBiS_2$, stoichiometric quantities of Ag(S_2COEt) and [Bi(S_2COEt)$_3$] complexes were ground to obtain a homogeneous mixture, and placed in a ceramic boat. The boat was then inserted in a glass reactor tube and heated in the furnace at 250 °C under nitrogen for 1 hour. After specified time duration, the heating source was removed and the furnace was cooled naturally.

Likewise, the solventless synthesis of metal doped $AgBiS_2$ involved pyrolysis of stoichiometric mixtures of Ag(S_2COEt), [Bi(S_2COEt)$_3$] and the respective metal dopant precursor under the same conditions. Particularly, a representative detailed synthetic procedure for the preparation of Cu-doped $AgBiS_2$ is given as follows.

A homogeneous mixture of [$Cu(S_2COEt)_2$] (0.01 g, 0.044mmol), $Ag(S_2COEt)$ **(**0.095g, 0.415mmol), and [$Bi(S_2COEt)_3$] **(**0.250g, 0.440mmol) was spread in a ceramic boat. The boat was placed in the centre of a quartz tube and heated in the furnace at a rate of 20 °C/min to the required target temperature of 250 °C in a nitrogen flow. After 1 hour, heating was turned off, the formed solid product allowed to cool to room temperature, and collected for further analysis. A detailed description of each of the synthesized systems is given in Table 3.1 below.

Table 3.1: The table below shows the calculated mass compositions in each formation of the ternary doped system.

Material synthesized	**% Metal xanthate**	**% Metal xanthate**	**% Metal xanthate**	**Mass of Metal xanthate**	**Mass Metal xanthate**	**Mass Metal xanthate**
$AgBiS_2$(standard)						
$Ag_{0.95}Cu_{0.05}BiS_2$	5% Cu	95% Ag	100% Bi	0.007 g Cu	0.095 g Ag	0.250 g Bi
$Ag_{0.90}Cu_{0.10}BiS_2$	10% Cu	90% Ag	100% Bi	0.0134 g Cu	0.090 g Ag	0.250 g Bi
$Ag_{0.85}Cu_{0.15}BiS_2$	15% Cu	85% Ag	100% Bi	0.0200 g Cu	0.085 g Ag	0.250 g Bi
$AgBi_{0.95}Sb_{0.05}S_2$	5% Sb	95% Bi	100% Ag	0.0106 g Sb	0.2375 g Bi	0.100 g Ag
$AgBi_{0.90}Sb_{0.10}S_2$	10% Sb	90% Bi	100% Ag	0.0212 g Sb	0.225 g Bi	0.100 g Ag
$AgBi_{0.85}Sb_{0.15}S_2$	15% Sb	85% Bi	100% Ag	0.032 g Sb	0.213 g Bi	0.100 g Ag
$AgFe_{0.05}Bi_{0.95}S_2$	5% Fe	95% Bi	100% Ag	0.0090 g Fe	0.237 g Bi	0.100 g Ag
$AgFe_{0.1}Bi_{0.90}S_2$	10% Fe	90% Bi	100% Ag	0.0181 g Fe	0.2250 g Bi	0.100 g Ag

$AgFe_{0.15}Bi_{0.85}S_2$	15% Fe	85% Bi	100% Ag	0.0181 g Fe	0.2250 g Bi	0.100 g Ag

3.3 Results and Discussion

3.3.1 Cu^{2+}, Sb^{3+} and Fe^{3+} doped $AgBiS_2$ by the melt method

Figure 3.1 shows a schematic diagram for decomposition of metal organic precursors to obtain $AgBiS_2$ doped with Cu^{2+}. This diagram shows three metal xanthates are mixed together in required stoichiometries, the homogenous mixture is placed in the crucible boat in the furnace where the reaction temperature is increased in an inert environment. Under heat treatment, C–S or M–S (M is either Cu^{2+}, Sb^{3+}, Fe^{3+} or Ag^{1+}) bond in precursors maybe broken, and Ag_2S, CuS, Fe_2S_3 and Sb_2S_3 nuclei are formed simultaneously. The M–S bonds were generated by the decomposition of C-S bonds. The nuclei of one metal sulfide combines/fuses with the nuclei of other metal sulfide to generate the alloyed ternary material. At the same time, when the M–S is generated by decomposition of precursors the volatile organic by-products are removed from other end of the tube furnace by nitrogen gas. The materials $AgSb_xBi_{1-x}S_2$, $Ag_{1-x}Cu_xBiS_2$ and $AgFe_xBi_{1-x}S_2$ formed, were used directly for analysis (XRD, SEM and EDS).

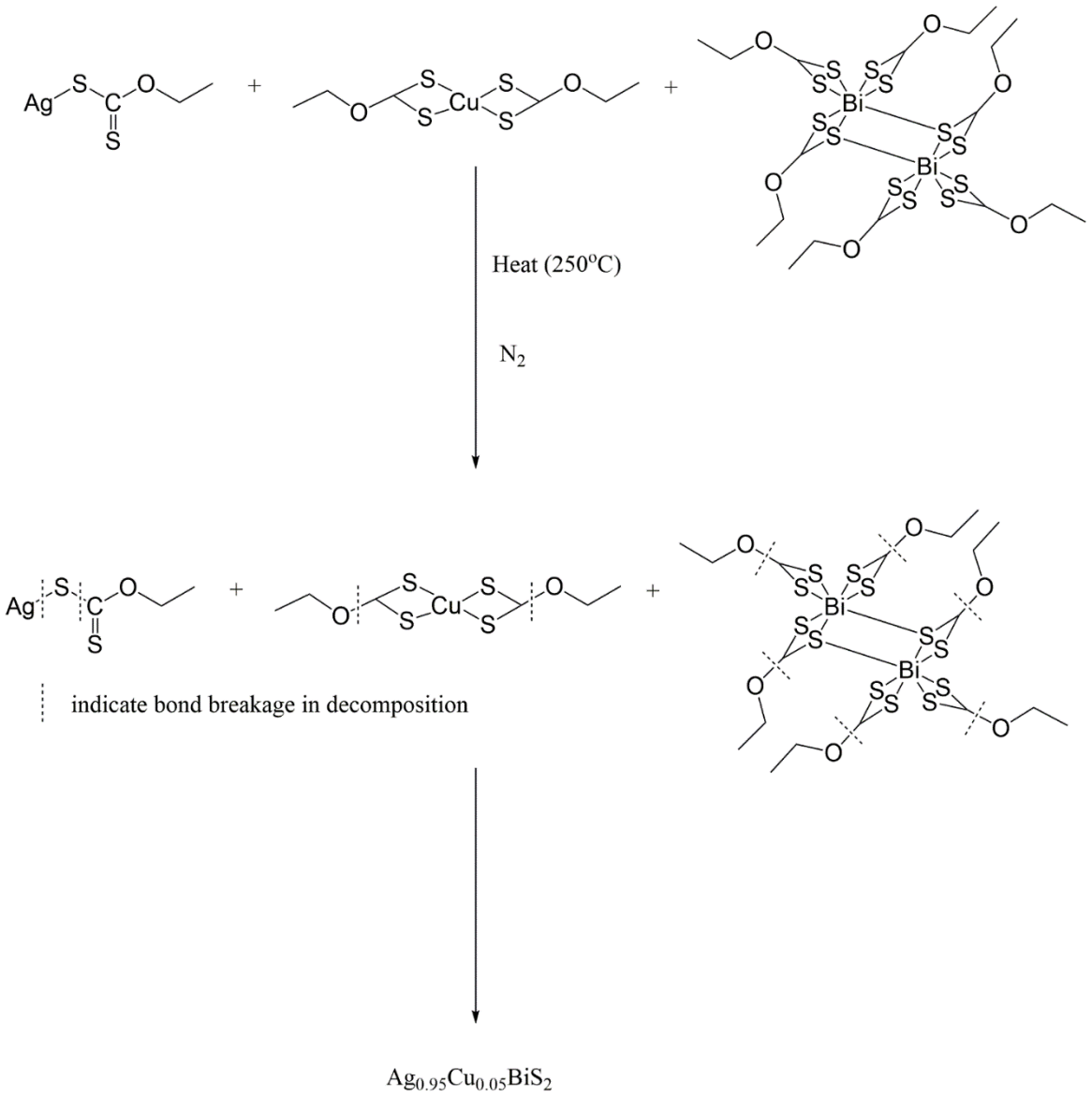

Figure 3.1: The diagram shows what is happening during heating and the function of Ethyl Xanthate as self-capping agent[44].

3.3.2 Characterization of precursors

The synthesized metal ethyl xanthate complexes were characterized by CHN and thermogravimetric analyses. Thermogravimetric analysis was performed to study the thermal stability and decomposition of the synthesized complexes AgEtX, CuEtX, BiEtX, SbEtX and FeEtX (EtX = ethyl xanthate) (Figures 3.2). The analysis was carried out at 20 °C/min heating rate from 30 °C to 700 °C under N_2 gas flow rate of 10 mL/min, using a Perkin Elmer Pyris 6 TGA equipped with a closed perforated ceramic pan. The thermograms of the decomposition of all the complexes show that they thermalize cleanly at fairly moderate temperatures. Complexes AgEtX, CuEtX, BiEtX and FeEtX decompose in a single step unlike complex SbEtX that thermalize in two steps. The second decomposition step of complex SbEtX could be due to the loss of some sulfur. The decomposition of all the complexes begin between 100 ^{0}C and 150 ^{0}C followed by a rapid weight loss and ends between 150 ^{0}C to 200 ^{0}C, typical of xanthate complexes.[40, 45] Complexes AgEtX, CuEtX, BiEtX, SbEtX and FeEtX decompose to a final weight loss of 55.1 %, 31 %, 45 %, 35 % and 28 % which is in good agreement with the calculated percentage weight loss of 52.3%, 31.3%, 44.9%, 35.0% and 28.6% respectively for Ag_2S, CuS, Bi_2S_3, Sb_2S_3 and FeS_2.

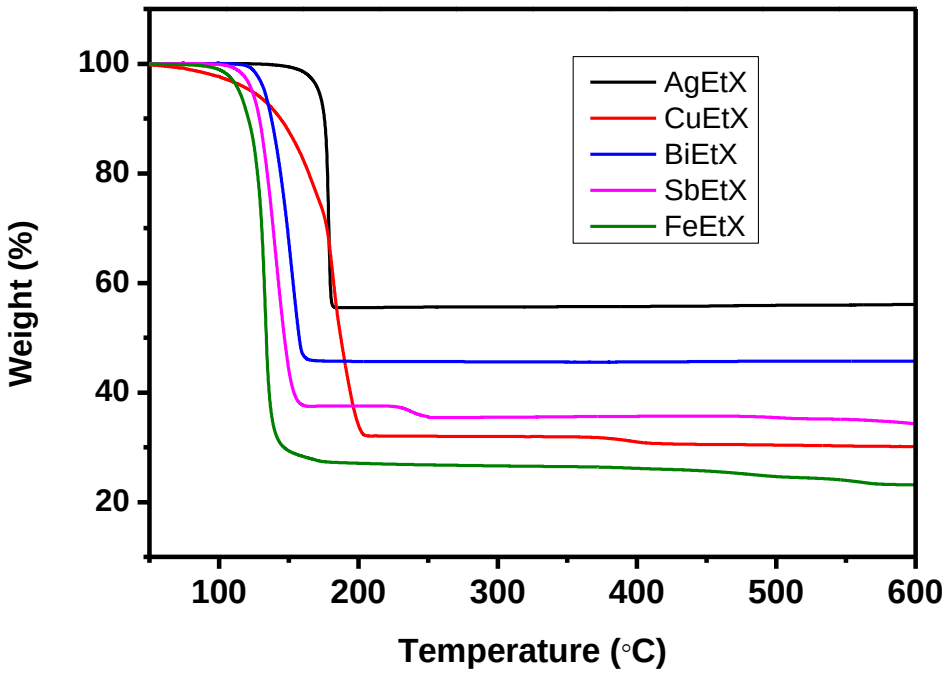

Figure 3.2: TGA profiles for $[Ag(S_2COEt_2)_3]$, $[Cu(S_2COEt_2)_2]$, $[Bi_2(S_2COEt_2)_6]$, $[Sb_2(S_2COEt_2)_6]$ and $[Fe(S_2COEt)_3]$.

3.3.3 Characterization of $AgBiS_2$ and metal doped $AgBiS_2$

All the synthesized materials ($AgBiS_2$, $Ag_{1-x}Cu_xBiS_2$, $AgSb_xBi_{1-x}S_2$ and $AgFe_xBi_{1-x}S_2$; x = 0.05, 0.1 and 0.15) were analysed by powder X- Ray Diffractometry (p-XRD), transmission electron microscopy (TEM), scanning electron microscopy (SEM) and energy dispersive X-ray spectroscopy (EDX). These instruments were discussed in detail in Chapter 2.

3.3.3.1 Characterization of $AgBiS_2$ and $Ag_{1-x}Cu_xBiS_2$ (x =0.05, 0.1, 0.15)

XRD patterns of the $AgBiS_2$ and $Ag_{1-x}Cu_xBiS_2$ materials prepared at 250 °C are shown in (Figure 3.3(a)). For $AgBiS_2$ the peaks match well with the cubic phase $AgBiS_2$ (JCPDS Card File No. 00-004-0699) and the diffraction peaks correspond to (111), (200), (220), (311), (222) and (400) planes. The presence of any impurity peaks were not observed. Likewise, the p-XRD analysis of the of $Ag_{1-x}Cu_xBiS_2$ series shows that the Cu has been incorporated into the $AgBiS_2$ lattice successfully, as there is no phase segregation or extra peaks observed, as an indication of the impurity phase. The substitution of Ag^+ with Cu^{2+} causes a gradual shift of the diffraction patterns towards higher angle with increasing concentration of copper (Figure 3.3(b)). This observation is in agreement with Vegard's law i.e. change in d-spacing with change in the composition. The shift in peak positions is attributed to the small ionic radius of Cu^{2+} (0.73Å) as compared to that of Ag^+ (1.15Å). The peaks are intense and sharp which indicates the good crystallinity of the material. The average particle size of $AgBiS_2$ using the Scherrer equation is 25.78 nm and of 5% Cu doped $Ag_{1-x}Cu_xBiS_2$ is 24.81 nm, 10% Cu doped is 28.61 nm, 15% Cu doped is 29.50 nm.

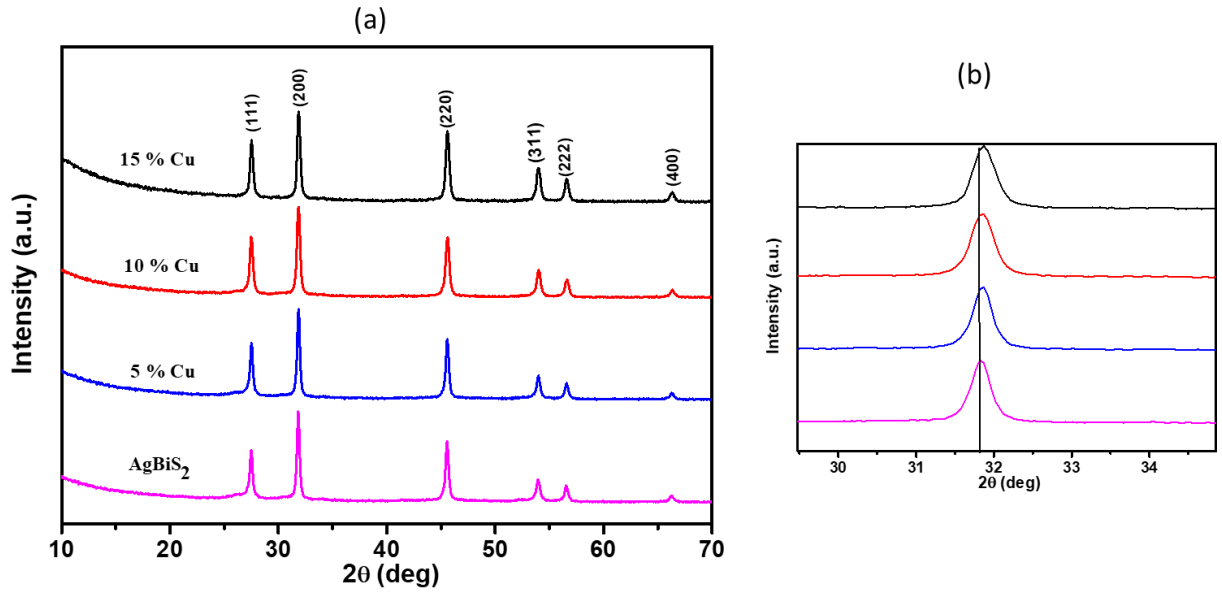

Figure 3.3: p-XRD peaks of (a) $AgBiS_2$ and $Ag_{1-x}Cu_xBiS_2$ (5% Cu, 10% Cu and 15% Cu) synthesized at 250 °C (b) Shows the shift of diffraction peaks to larger values as the composition x changes from $AgBiS_2$ to 15% Cu doped materials synthesized by the melt method.

The transmission electron microscopy (TEM) images of the $AgBiS_2$ and Cu doped $AgBiS_2$ are shown in Figure 3.4. The particles were aggregated and the particles were of irregular shape. The particles were poly-dispersed due to the absence of any capping agent. The absence of capping agent results in agglomerated particles as the particles are of high surface energy and it is accompanied by increasing of aggregation to form larger particles and lower the overall energy. The average size particles are (a) 35.40 nm, (b) 15.21 nm, (c) the particles were too agglomerated to calculate the average size particles and (d) 33.00 nm.

Likewise Cu doped $AgBiS_2$ showed similar behaviour and particles showed a broad size distribution. This implies that the incorporation of Cu in $AgBiS_2$ crystal lattice causes no significant effect on the morphology of the particles.

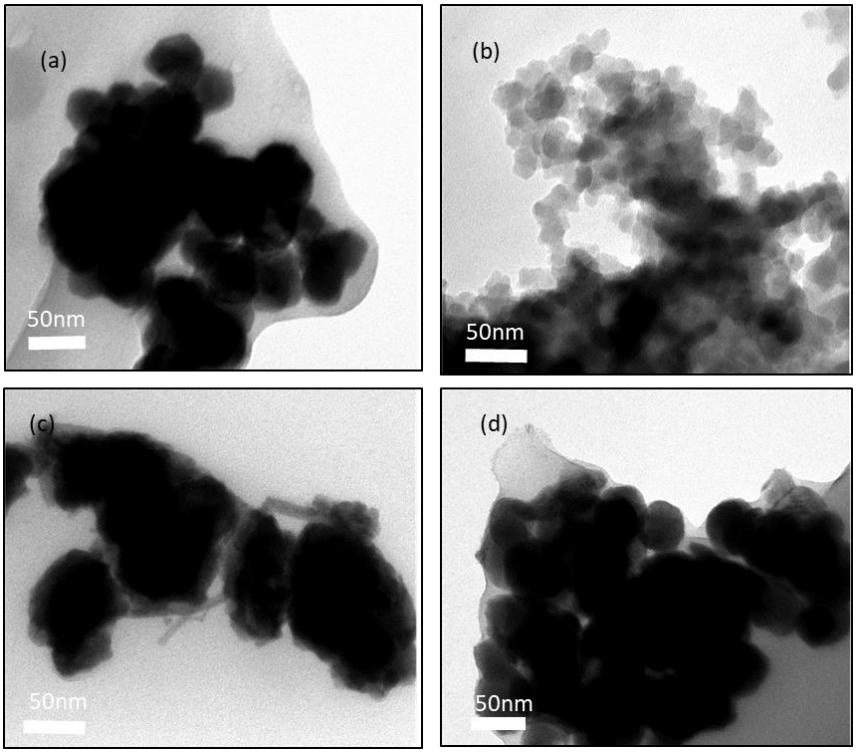

Figure 3.4: TEM images of (a) $AgBiS_2$, (b) 5% Cu doped $AgBiS_2$ (c) 10% Cu doped $AgBiS_2$ and (d) 15% Cu doped $AgBiS_2$ synthesized at 250 °C.

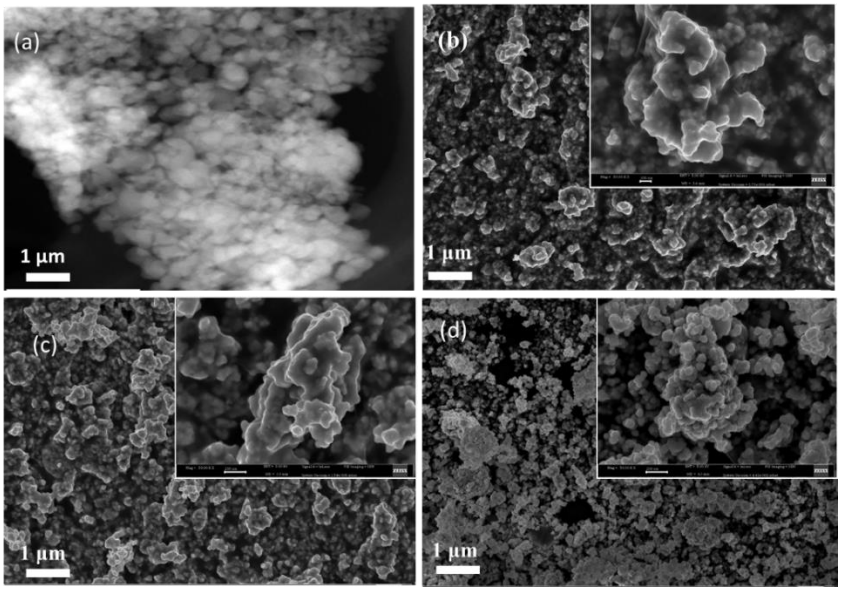

Figure 3.5: SEM images of (a) $AgBiS_2$, (b) 5% Cu doped $AgBiS_2$ (c) 10% Cu doped $AgBiS_2$ and (d) 15% Cu doped $AgBiS_2$ synthesized at 250 °C.

Figure 3.5 (a–d) shows the SEM images of the $AgBiS_2$ (the image of $AgBiS_2$ is used throughout the results for comparisons purposes) and $Ag_{1-x}Cu_xBiS_2$ (5%, 10% and 15%) systems. The images of Cu doped $AgBiS_2$ particles were taken at different magnifications (Figure 3.5(b-d)) and the higher magnification image were shown as inset images. The particles did not show any defined morphology and the particle size changes slightly with different doping concentrations, revealed by SEM observations, is in agreement with the calculations of crystallite size from the XRD patterns as shown in Figure 3.3(a).

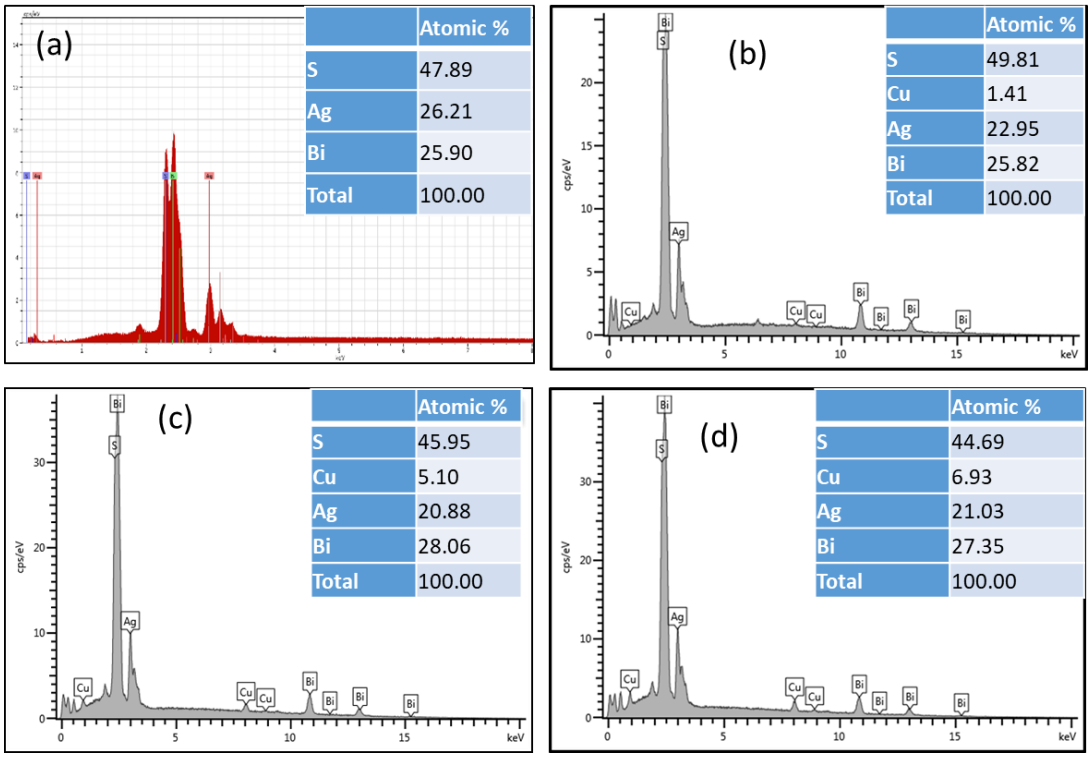

Figure 3.6: Comparison of the compositions observed by the EDX analysis (a) $AgBiS_2$, (b) 5% Cu doped $AgBiS_2$ (c) 10% Cu doped $AgBiS_2$ and (d) 15% Cu doped $AgBiS_2$ synthesized at 250 °C.

The composition of the samples was determined by EDX analysis, as shown in Figure 3.6. Pristine $AgBiS_2$ showed the presence of Ag, Bi and S in almost required stoichiometric amounts while the sample is slightly sulfur deficient. Likewise the compositional analysis of the alloyed samples, showed the presence of copper along with Ag, Bi and S within the range of the required dopant concentration as indicated in Table 2 below respectively. All the samples were sulfur deficient, especially the samples with high dopant concentrations. The

high temperature might have resulted in the sublimation of the sulfur due to its high partial pressure.

Table 3.2: The comparison of theoretical composition prepared by melt and EDX analysis.

	Prepared by melt method				**Analysed by EDX %**			
a	1.25% Cu	23.75% Ag	25% Bi	50% S	1.41 Cu	22.95 Ag	25.82 Bi	49.81 S
b	2.5% Cu	22.5% Ag	25% Bi	50% S	5.10 Cu	20.88 Ag	28.06 Bi	45.95 S
c	3.75% Cu	21.25% Ag	25% Bi	50% S	6.93 Cu	21.03 Ag	27.35 Bi	44.69 S

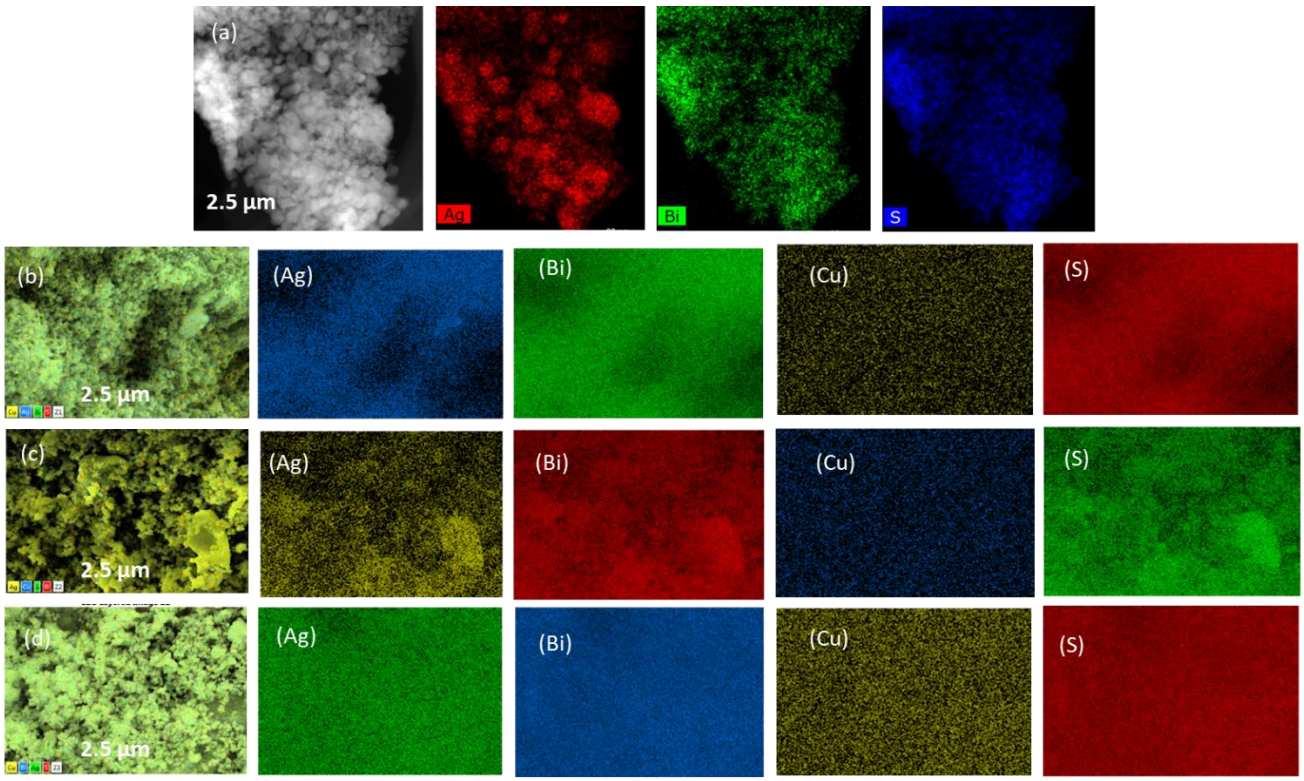

Figure 3.7: Mapping observed by the EDX analysis (a) $AgBiS_2$, (b) 5% Cu doped $AgBiS_2$ (c) 10% Cu doped $AgBiS_2$ and (d) 15% Cu doped $AgBiS_2$ synthesized at 250 °C.

In Figure 3.7, the elemental mapping shows the uniform elemental distribution of each atom in $AgBiS_2$ and $Ag_{1-x}Cu_xBiS_2$ samples. It shows the suitability of the melt method to prepare homogenous alloys at large scale.

3.3.3.2 Characterization of $AgBiS_2$ and $AgSb_xBi_{1-x}S_2$ (x =0.05, 0.1, 0.15))

The p-XRD analysis of the $AgSb_xBi_{1-x}S_2$ series shows the similar kind of diffraction peaks of the alloy system when compared to the undoped $AgBiS_2$. Since the ionic radius of Bi^{3+} is larger (1.03Å) than that of the Sb^{3+} (0.76Å), a small shift of the diffraction peaks to higher angles is observed with increasing Sb^{3+} concentration (Figure 3.8b). This shift agrees with Vegard's law. There was no indication of the presence of Ag_2S, Bi_2S_3, Sb_2S_3 or other undesired phases. The average particle size of $AgBiS_2$ using the Scherrer equation was 25.78 nm and for $AgSb_xBi_{1-x}S_2$ were (34.38 nm for 5% Sb doped, 35.24 nm for 10% Sb doped, and 38.99 nm for 15% Sb doped).

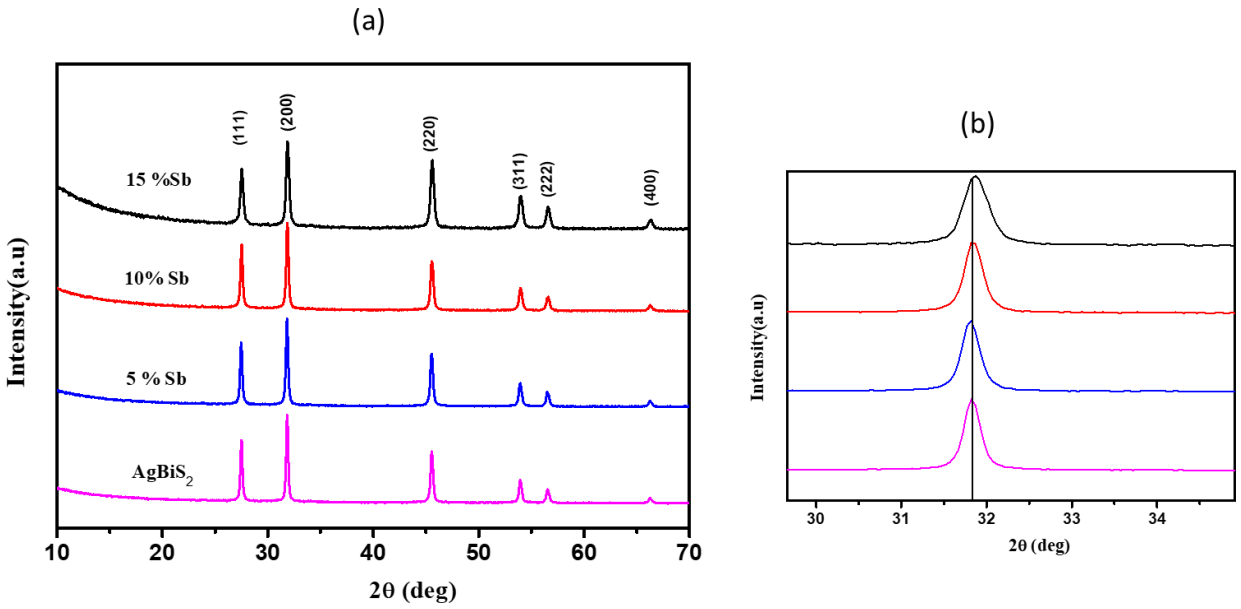

Figure 3.8: p-XRD peaks for (a) $AgBiS_2$ undoped and $AgSb_xBi_{1-x}S_2$ (5% Sb, 10% Sb and 15% Sb) (b) Shows the shift of diffraction peaks to larger values as the composition x changes from $AgBiS_2$ undoped to 15% dopant materials synthesised by melt method.

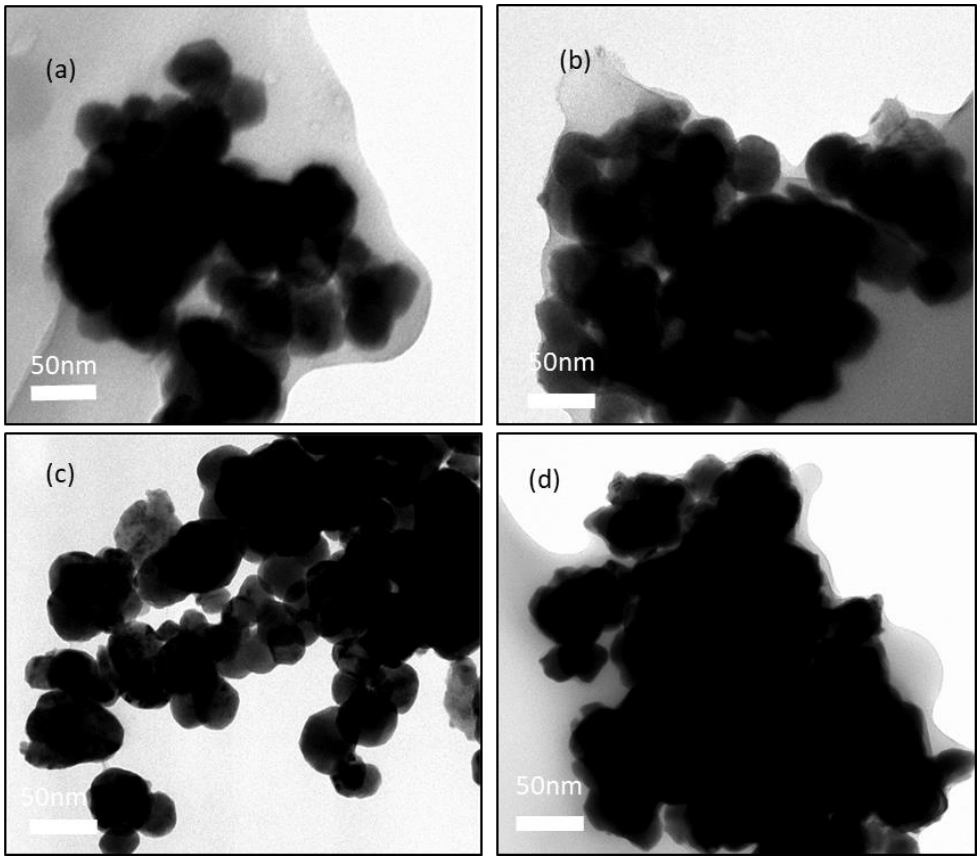

Figure 3.9: TEM images of (a) $AgBiS_2$, (b) 5% Sb doped $AgBiS_2$ (c) 10% Sb doped $AgBiS_2$ and (d) 15% Sb doped $AgBiS_2$ synthesized at 250 °C.

Figure 3.9 shows the transmission electron microscopy (TEM) images of $AgSb_xBi_{1-x}S_2$, doped by Sb^{3+} (from 5% 10% and 15%), where the substitution is between Bi^{3+} and Sb^{3+}. Figure 3.9 shows that the particles have a wide size distribution due to agglomeration of particles, to lower the surface energy. All samples were composed of agglomerated particles with the average particle sizes of (a) 35.40 nm, (b) 44.99 nm, (c) 49.80 nm and (d) 59.34 nm, and the crystallite size calculated by the Debye–Scherrer equation.

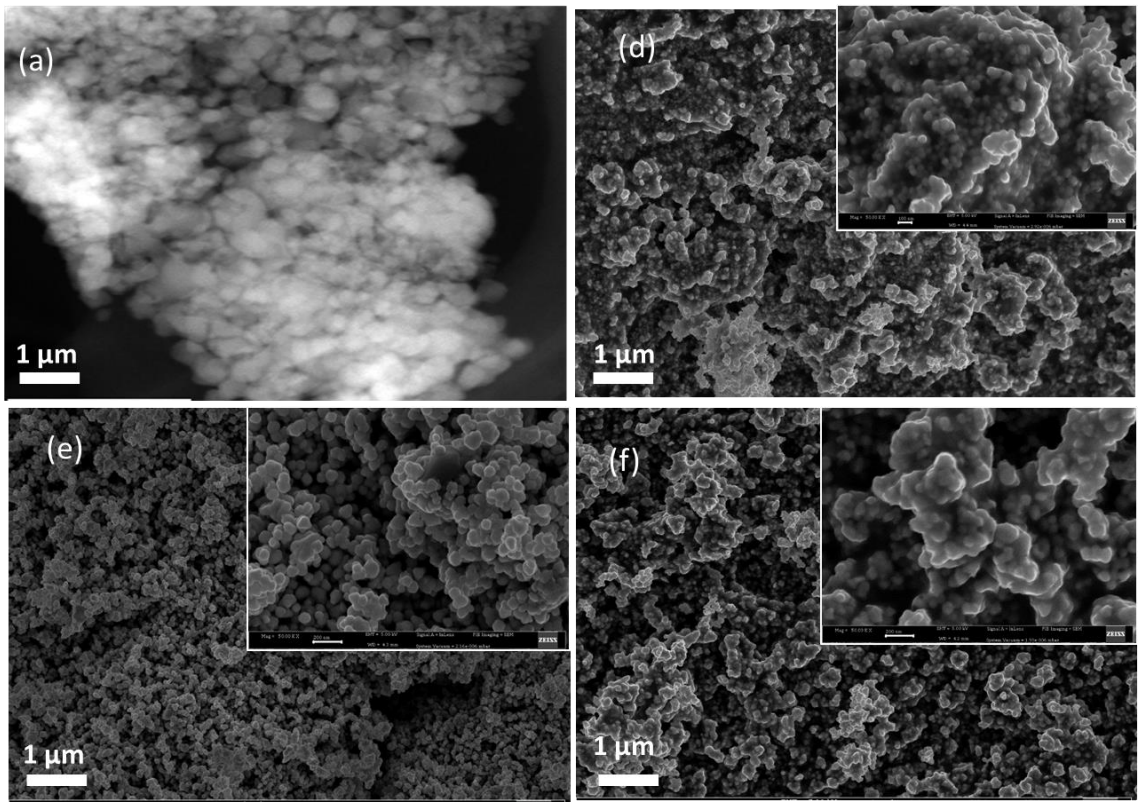

Figure 3.10: SEM images of (a) $AgBiS_2$ undoped, and $AgSb_xBi_{1-x}S_2$ doped with (b) 5% Sb (c) 10% Sb and (d) 15% Sb.

Figure 3.10 (a–d) shows the SEM images of Sb^{3+} doped (5%, 10% and 15%) $AgSb_xBi_{1-x}S_2$ systems. The images taken at different scales as shown in Figure 3.10 (b-d). The image at low resolution was taken to observe the overall size distribution and morphology of sample at large scale, whereas the inset image is taken at 100 nm, to show the shape of the particles by substitution of Bi^{3+} with Sb^{3+}. Figure 3.10 (a) shows SEM image of un-doped $AgBiS_2$ at 1 µm for comparison with the doped samples. The particles show that the shape is spherical to somewhat elongated. The particle size changes slightly and the agglomeration increases, as revealed by SEM observations, which is in agreement with the calculations of crystallite size from the XRD patterns as shown in Figure 3.8(a).

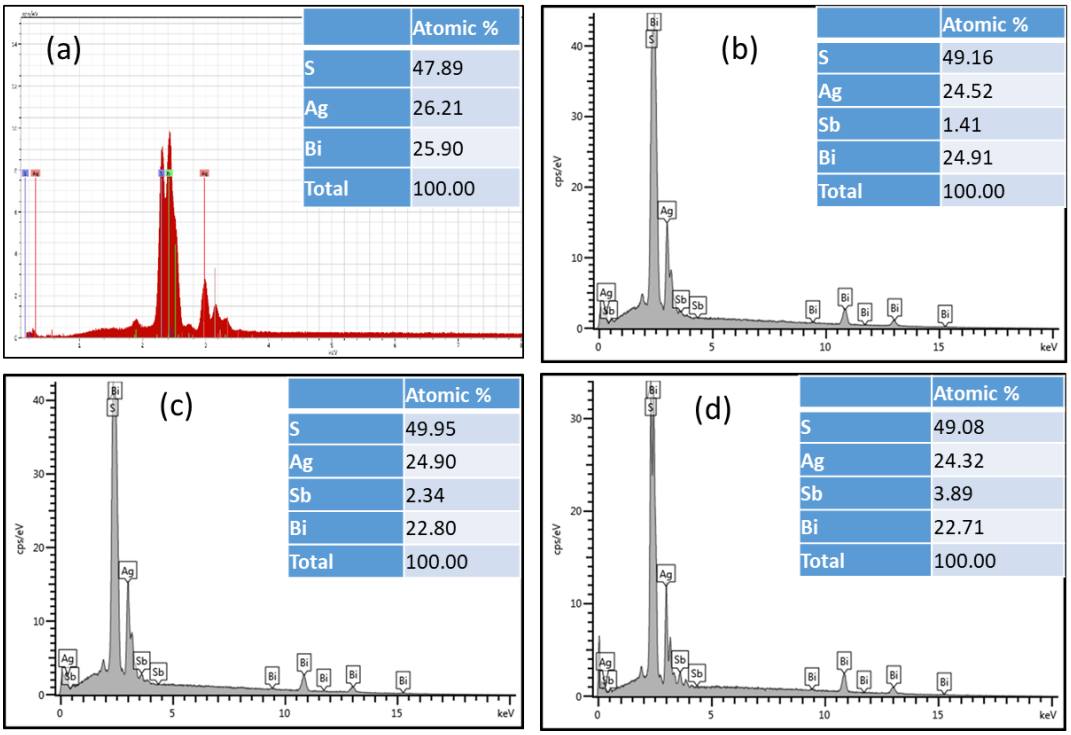

Figure 3.11: Comparison of the compositions observed by the EDX analysis for (a) $AgBiS_2$ undoped and $AgSb_xBi_{1-x}S_2$ doped with (b) 5% Sb (c) 10% Sb and (d) 15% Sb.

The EDX spectrum of the powder prepared for 1h are shown in Figure 3.11. The EDX for $AgBiS_2$ shows the existence of Ag, Bi, S (Figure 3.11(a)), and Figure 3.11(b-d) shows Ag, Bi, S and Sb as dopant in different concentrations (i.e. from 5% to 15%). The atomic percentages of all elements were found to be relatable to the added dopant quantity. The calculated dopant values and the elemental percentage obtained by EDX is listed in Table 3 below respectively, which shows that there are small differences in calculated values and the EDX results.

Table 3.3: The comparisons of theoretical composition prepared by melt and EDX analysis.

	Prepared by melt method				**Analysed by EDX %**			
	% of Sb	**% of Bi**	**% of Ag**	**% of S**	**% of Sb**	**% of Bi**	**% of Ag**	**% of S**
a		25 %	25 %	50 %		25.90 %	26.21 %	47 %
b	1.25 %	23.75 %	25 %	50 %	1.41 %	24.91 %	24.52 %	49.16 %
c	2.5 %	22.5 %	25 %	50 %	2.34 %	22.80 %	24.90 %	49.95 %
d	3.75 %	21.25 %	25 %	50 %	3.89 %	22.71 %	24.32 %	49.08 %

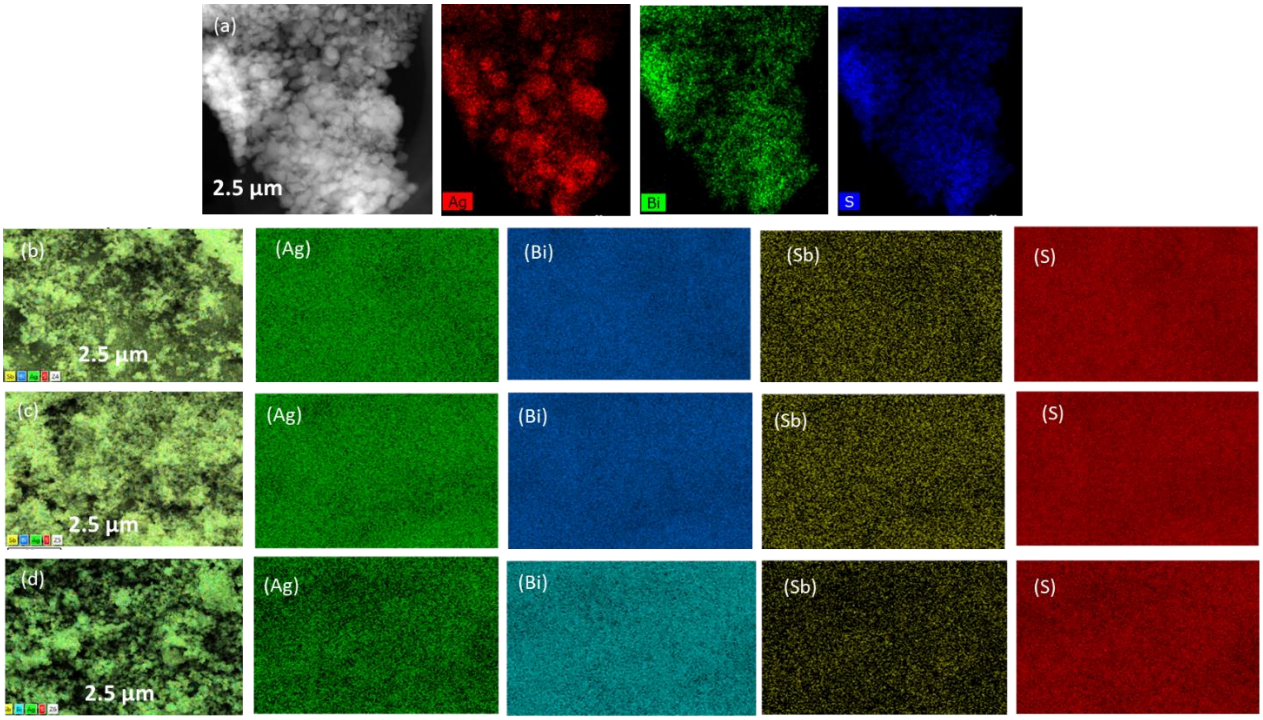

Figure 3.12: Mapping observed by the EDX analysis (a) $AgBiS_2$ undoped, $AgSb_xBi_{1-x}S_2$ (b) 5% Sb (c) 10% Sb and (d) 15% Sb materials synthesized by the melt method.

Figure 3.12 shows the EDX mapping and the elemental distribution of each atom in the parent $AgBiS_2$ and doped samples i.e. $AgSb_xBi_{1-x}S_2$. The dopants are equally distributed from Sb as

indicated in Figure 3.12 (b-d). This also shows that the melt method can be used for the scale up synthesis of ternary and doped materials.

3.3.3.3 $AgBiS_2$ undoped and $AgFe_xBi_{1-x}S_2$ materials using 5%, 10% and 15% Fe^{3+} by substituting Bi^{3+} metals.

XRD patterns of $AgFe_xBi_{1-x}S_2$ materials showed cubic phase with JCPDS Card File No. 00-004-0699 from 10^o to 70^o 2θ x-axis (Figure 3.13). The p-XRD analysis of $AgFe_xBi_{1-x}S_2$ series shows that the diffraction peaks of the alloy system fall in between those of pure $AgBiS_2$ and the doped samples (Figure 3.13). A shift towards the higher angle was observed with increasing concentration of the Fe^{3+} mole ratio, especially for the (111) plane where the shift is towards higher theta. This confirms the substitution of Bi^{3+} by Fe^{3+} where Bi (1.03Å) ionic radius is bigger than that of Fe (0.63 Å), although they have similar charges. This is also confirmed by Vegard's law which indicates that the d-spacing is inversely proportional to the theta value, hence with the replacement of the bigger Bi atom by a smaller Fe atom the shift will be on a higher angle. No indications of other undesired phases were identified by XRD, the peaks correspond to planes of (111,200, 220,311, 222 and 400) of $AgBiS_2$ and $AgFe_xBi_{1-x}S_2$.

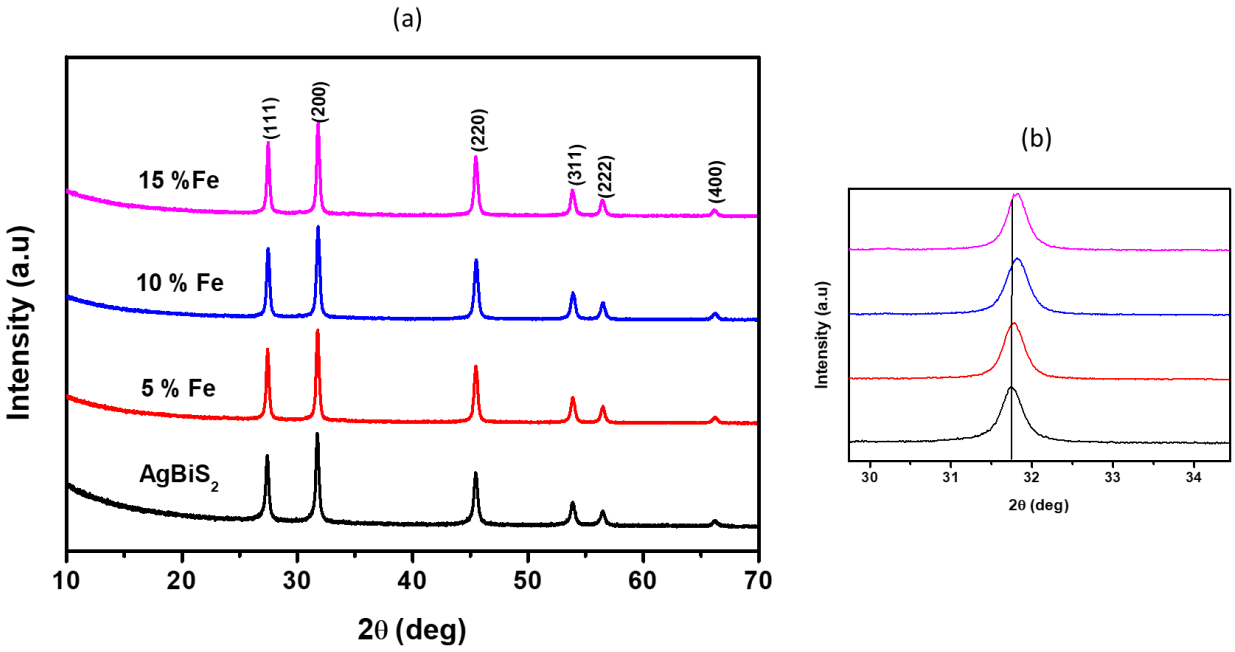

Figure 3.13: p-XRD peaks for (a) undoped $AgBiS_2$ and $AgFe_xBi_{1-x}S_2$ (5% Fe, 10% Fe and 15% Fe), (b) Shows the shift of diffraction peaks to larger values as the composition x changes from $AgBiS_2$ undoped to 15% dopant materials synthesised by melt method.

The average particle size of $AgBiS_2$ using Scherrer equation was 25.78 nm, and for $AgFe_xBi_{1-x}S_2$ were (for 5% Fe doped 28.92 nm, 10% Fe doped 26.74 nm and 15% Fe doped 29.48 nm). With respect of properties of melt method and xanthate ligands most of the materials can be synthesised[40].

Figure 3.14 shows the transmission electron microscopy (TEM) images of $AgFe_xBi_{1-x}S_2$ doped by Fe^{3+} (5%, 10% and 15%). In Figure 3.14(a-d) all particles are cubic in shape. Figure 3.14 (b-d) shows small particles compared to Figure 3.14a. This may be due to the ionic radius comparison between Bi^{3+} and Fe^{3+}. The average size of particles obtained from the TEM images are (a) 35.40 nm, (b) 4712 nm, (c) 64.37 nm and (d) 69.45 nm. This deviation of particle shapes could be due to the dopant and the concentration of sulphur from both metal xanthates.

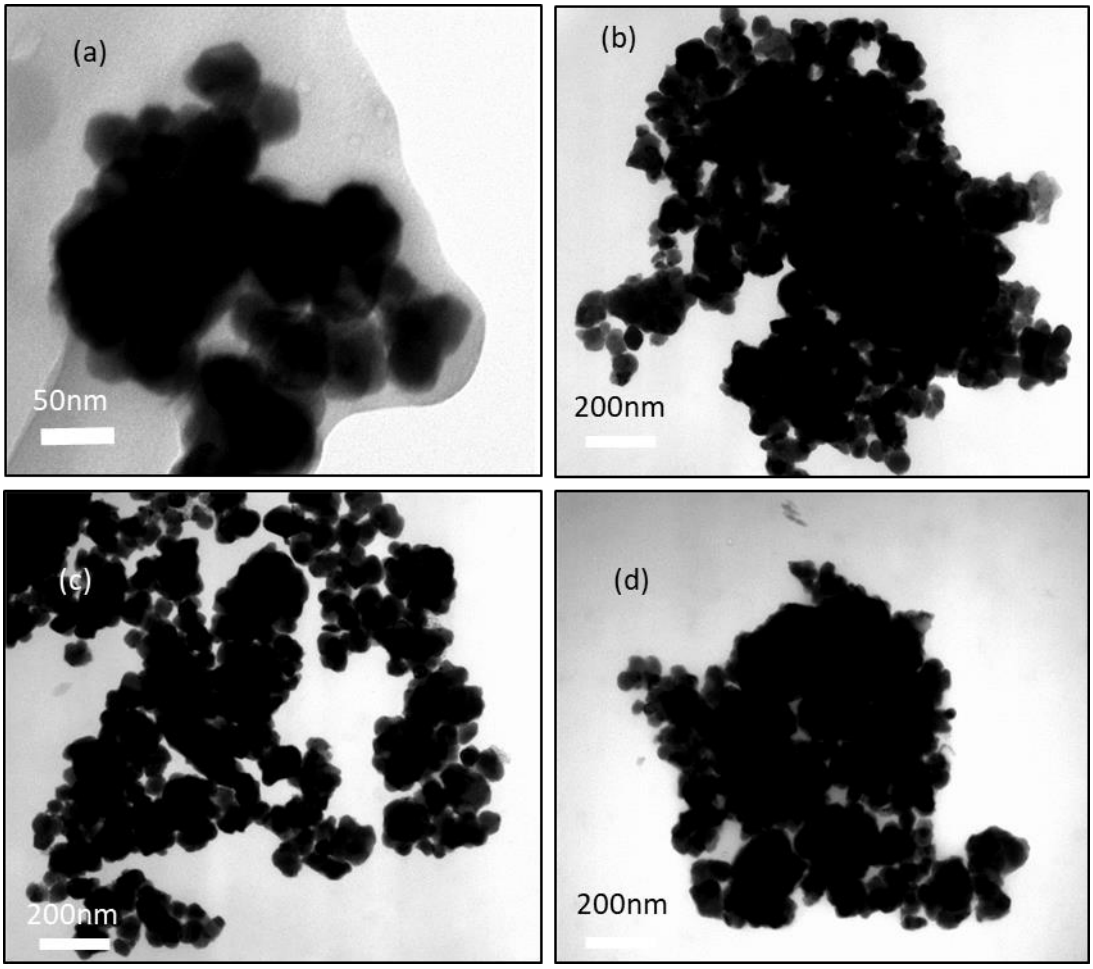

Figure 3.14: TEM images of the ternary crystals produced from metal ethyl xanthate complex single source precursor to melt method. (a) un-doped $AgBiS_2$, (b) 5% Fe doped $AgBiS_2$, (c) 10% Fe doped $AgBiS_2$ and (d) 15% Fe doped $AgBiS_2$.

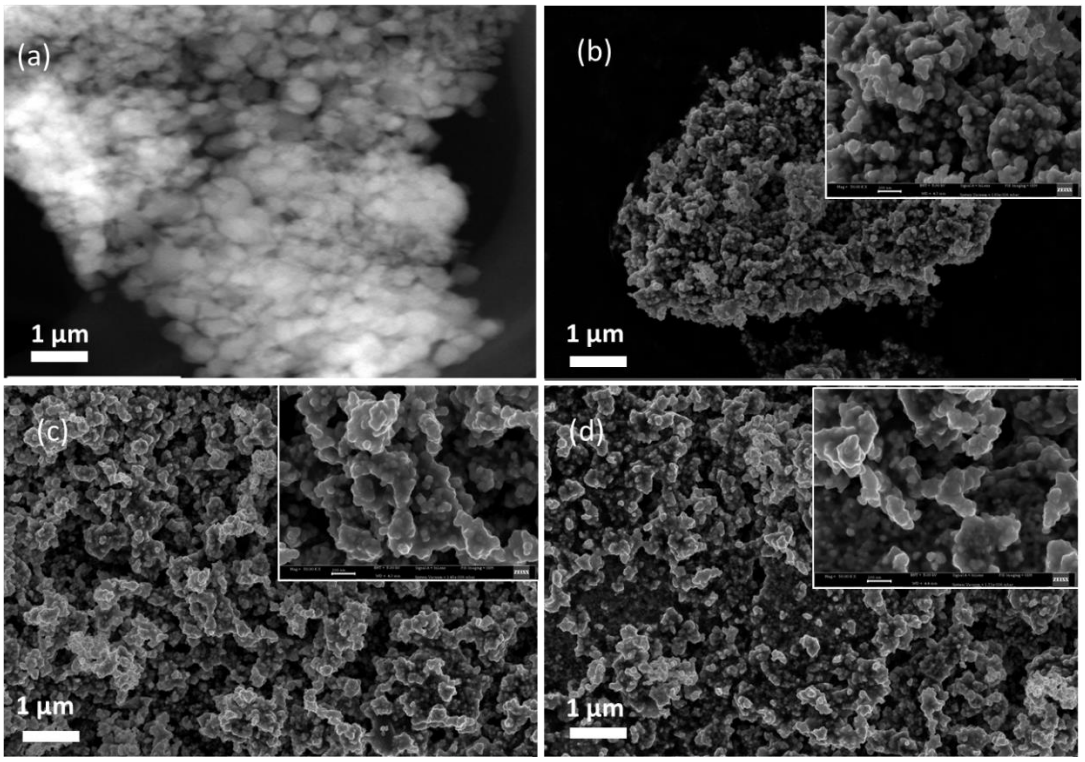

Figure 3.15: SEM images of (a) $AgBiS_2$ undoped, $AgFe_xBi_{1-x}S_2$ (b) 5% Fe (c) 10% Fe and (d) 15% Fe materials synthesized by the melt method.

Figure 3.15 (a–d) shows the SEM images of $AgFe_xBi_{1-x}S_2$ doped Fe^{3+} (5%, 10% and 15%) which confirms the particle shapes as cubic. Figure 3.15(b-d) were selected from different scales, for example one in 1um and other one in 100 nm. The shape distribution in both scales confirms the cubic shape except for (d) where the shape is not clear. The tendency of the particle size changes, revealed by SEM observations, is in agreement with the calculations of crystallite size from the XRD patterns as shown in Figure 3.13.

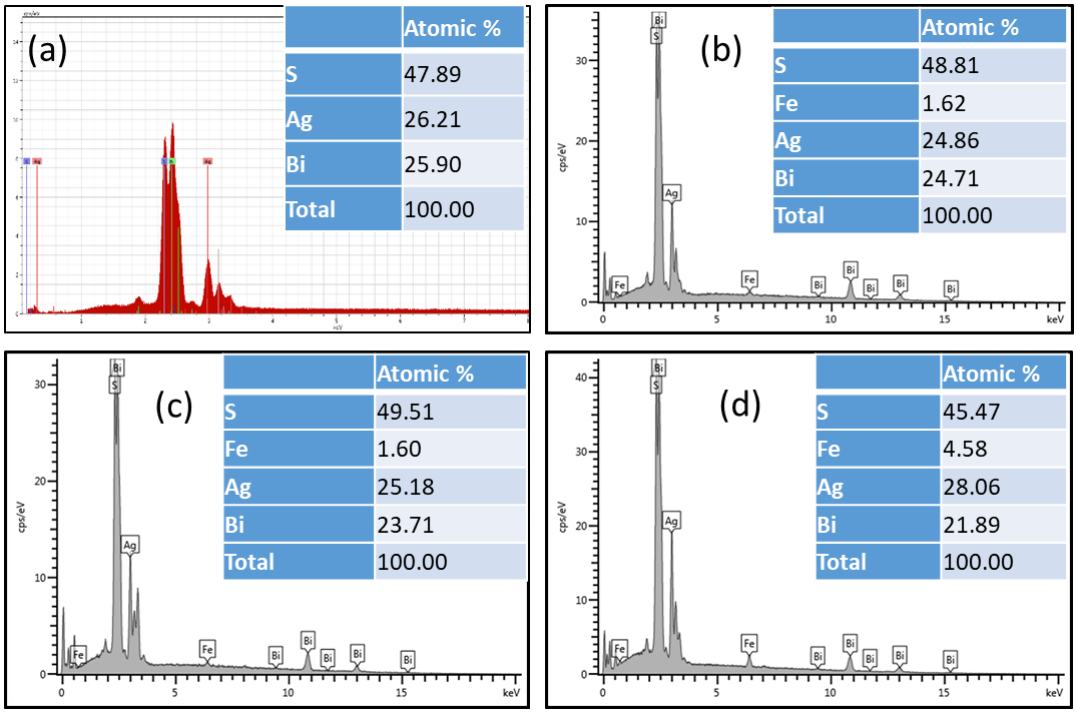

Figure 3.16: Comparison of the compositions observed by the EDX analysis for (a) $AgBiS_2$ undoped and $AgFe_xBi_{1-x}S_2$ doped with (b) 5% Fe (c) 10% Fe and (d) 15% Fe, synthesized by the melt method at 250 °C.

The EDX spectrum of the powder prepared at 1h by in Figure 3.16 presents the existence of Ag, Bi, S and elements and dopants Fe. The atomic percentages of all metals were found to be corresponding to the prepared dopant as shown in the Table 4 below. The observable change of sulphur element in graph (d) shows a smaller percentage as compared to others. This could be due to the higher percentage of Fe dopant.

Table 3.4: The comparisons of theoretical composition prepared by melt and EDS analysis.

	Prepared by melt method				**Analysed by EDX %**			
	% of Fe	**% of Ag**	**% of Bi**	**% of S**	**% of Fe**	**% of Ag**	**% of Bi**	**% of S**
a		25 %	25 %	50 %		26.21 %	25.90 %	47.89 %
g	1.25 %	23.75% Bi	25% Ag	50% S	1.60 %	24.71 %	24.86 %	48.81 %
h	2.5 %	22.5 Bi	25% Ag	50% S	1.65 %	23.7 %	25.16 %	49.50 %
i	3.75 %	21.25 Bi	25% Ag	50% S	4.58 %	21.89 %	28.06 %	45.47 %

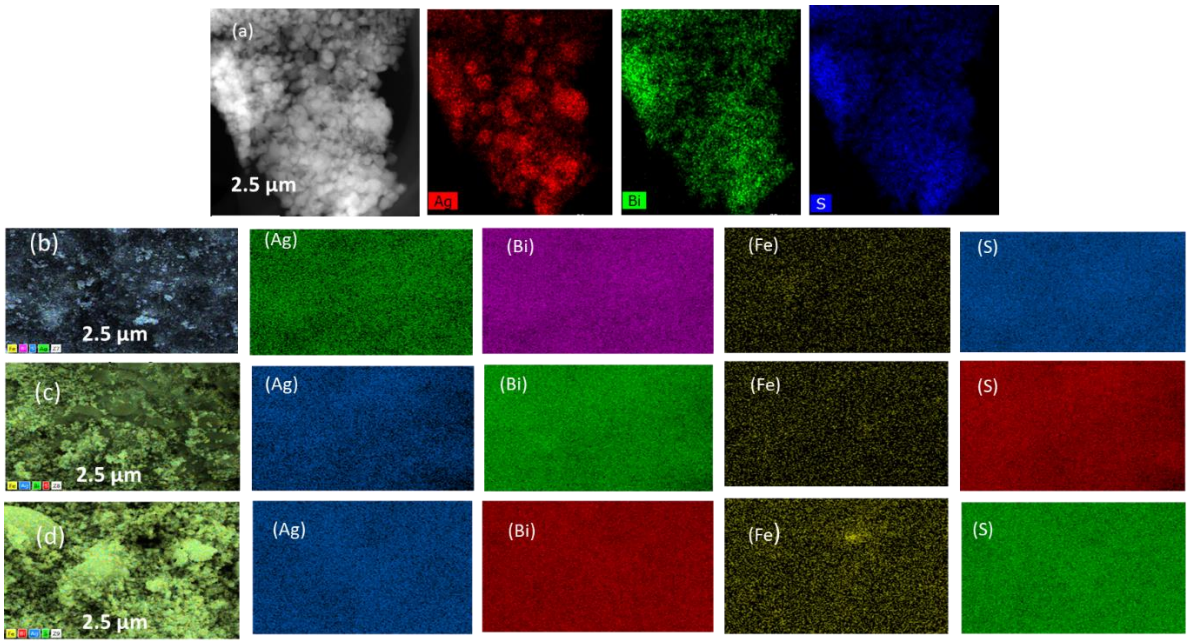

Figure 3.17: Mapping observed by the EDX analysis (a) $AgBiS_2$ undoped and $AgFe_xBi_{1-x}S_2$ doped with (b) 5% Fe (c) 10% Fe and (d) 15% Fe synthesized by the melt method at 250 °C.

The EDX mapping (Figure 3.17) shows the elemental distribution per each atom in the systems of $AgBiS_2$ and $AgFe_xBi_{1-x}S_2$. The atomic distribution is referred to the SEM image as indicated above including dopants Fe and Bi comparison shows that Fe is well distributed in the system doped.

3.4 Conclusion

The ternary system of $AgBiS_2$ and $AgBiS_2$ doped with Cu^{2+}, Sb^{3+} and Fe^{3+} has been successfully prepared using the melt method (the solventless approach). This synthesis process yielded cubic shaped $AgBiS_2$ and $AgBiS_2$ doped with Cu^{2+}, Sb^{3+} and Fe^{3+} nanocrystals at 250°C. The average size of the particles ranged from ±15.00 nm to ±60.00 nm; this proves the materials were in nanocrystals.

3.5 References

1. Mowery, D.C., *Federal policy and the development of semiconductors, computer hardware, and computer software: a policy model for climate change R&D?*, in *Accelerating Energy Innovation: Insights from Multiple Sectors*. 2011, University of Chicago Press. p. 159-188.
2. Anitha, V., A.N. Banerjee, and S.W. Joo, *Recent developments in TiO_2 as n-and p-type transparent semiconductors: synthesis, modification, properties, and energy-related applications.* Journal of materials science, 2015. **50**(23): p. 7495-7536.
3. Chakraborty, A., *Advancements in power electronics and drives in interface with growing renewable energy resources.* Renewable and Sustainable Energy Reviews, 2011. **15**(4): p. 1816-1827.
4. Lai, C.-H., M.-Y. Lu, and L.-J. Chen, *Metal sulfide nanostructures: synthesis, properties and applications in energy conversion and storage.* Journal of Materials Chemistry, 2012. **22**(1): p. 19-30.
5. Schou, P., *Polluting non-renewable resources and growth.* Environmental and Resource Economics, 2000. **16**(2): p. 211-227.
6. Giusti, L., *A review of waste management practices and their impact on human health.* Waste management, 2009. **29**(8): p. 2227-2239.
7. Wang, X., Lu, X., Liu, B., Chen, D., Tong, Y. and Shen, G., *Flexible energy-storage devices: design consideration and recent progress.* Advanced materials, 2014. **26**(28): p. 4763-4782.
8. Arico, A.S., Bruce, P., Scrosati, B., Tarascon, J.M. and Van Schalkwijk, W., *Nanostructured materials for advanced energy conversion and storage devices*, in *Materials for sustainable energy: a collection of peer-reviewed research and review articles from Nature Publishing Group*. 2011, World Scientific. p. 148-159.
9. Millán, J., Godignon, P., Perpiñà, X., Pérez-Tomás, A. and Rebollo, J., *A survey of wide bandgap power semiconductor devices.* IEEE transactions on Power Electronics, 2013. **29**(5): p. 2155-2163.
10. Gurunathan, K., Murugan, A.V., Marimuthu, R., Mulik, U.P. and Amalnerkar, D.P., *Electrochemically synthesised conducting polymeric materials for applications towards technology in electronics, optoelectronics and energy storage devices.* Materials Chemistry and Physics, 1999. **61**(3): p. 173-191.

11. Aldakov, D., A. Lefrançois, and P. Reiss, *Ternary and quaternary metal chalcogenide nanocrystals: synthesis, properties and applications.* Journal of Materials Chemistry C, 2013. **1**(24): p. 3756-3776.
12. Regulacio, M.D. and M.-Y. Han, *Multinary I-III-VI2 and I2-II-IV-VI4 semiconductor nanostructures for photocatalytic applications.* Accounts of Chemical Research, 2016. **49**(3): p. 511-519.
13. Prusty, G., Guria, A.K., Patra, B.K. and Pradhan, N.,*Diffusion-induced shape evolution in multinary semiconductor nanostructures.* The journal of physical chemistry letters, 2015. **6**(13): p. 2421-2426.
14. Zhao, Y. and C. Burda, *Development of plasmonic semiconductor nanomaterials with copper chalcogenides for a future with sustainable energy materials.* Energy & Environmental Science, 2012. **5**(2): p. 5564-5576.
15. Ryan, K.M., Singh, S., Liu, P. and Singh, A., *Assembly of binary, ternary and quaternary compound semiconductor nanorods: From local to device scale ordering influenced by surface charge.* CrystEngComm, 2014. **16**(40): p. 9446-9454.
16. Mahboob, S., Malik, S.N., Haider, N., Nguyen, C.Q., Malik, M.A. and O'Brien, P., *Deposition of binary, ternary and quaternary metal selenide thin films from diisopropyldiselenophosphinato-metal precursors.* Journal of crystal growth, 2014. **394**: p. 39-48.
17. Chen, D., Shen, G., Tang, K., Jiang, X., Huang, L., Jin, Y. and Qian, Y., *Microwave synthesis of $AgBiS_2$ dendrites in aqueous solution.* Inorganic Chemistry Communications, 2003. **6**(6): p. 710-712.
18. Thongtem, T., J. Jaroenchaichana, and S. Thongtem, *Cyclic microwave-assisted synthesis of flower-like and hexapod silver bismuth sulfide.* Materials Letters, 2009. **63**(24-25): p. 2163-2166.
19. Huang, P.-C., W.-C. Yang, and M.-W. Lee, *$AgBiS_2$ semiconductor-sensitized solar cells.* The Journal of Physical Chemistry C, 2013. **117**(36): p. 18308-18314.
20. Nakamura, M., Nakamura, H., Ohsawa, T., Imura, M., Shimamura, K. and Ohashi, N., *$AgBiS_2$ single crystal grown using slow cooling method and its characterization.* Journal of Crystal Growth, 2015. **411**: p. 1-3.
21. Liu, H., Zhong, J., Liang, X., Zhang, J. and Xiang, W., *A mild biomolecule-assisted route for preparation of flower-like $AgBiS_2$ crystals.* Journal of alloys and compounds, 2011. **509**(27): p. L267-L272.

22. Shen, G., Chen, D., Tang, K. and Qian, Y., *Novel polyol route to $AgBiS_2$ nanorods.* Journal of crystal growth, 2003. **252**(1-3): p. 199-201.
23. Bai, J., Ban, Y., Bian, J.G., Chen, G.P., Chen, H.F., Chen, J., Chen, J.C., Chen, Y., Chen, Y.B., Chen, Y.Q. and Cheng, B.S., *Measurement of the total cross section for hadronic production by $^{e+}$ $^{e-}$ annihilation at energies between 2.6–5 GeV.* Physical Review Letters, 2000. **84**(4): p. 594.
24. Thongtem, T., N. Tipcompor, and S. Thongtem, *Characterization of $AgBiS_2$ nanostructured flowers produced by solvothermal reaction.* Materials Letters, 2010. **64**(6): p. 755-758.
25. Wang, F., Shifa, T.A., Zhan, X., Huang, Y., Liu, K., Cheng, Z., Jiang, C. and He, J., *Recent advances in transition-metal dichalcogenide based nanomaterials for water splitting.* Nanoscale, 2015. **7**(47): p. 19764-19788.
26. Larsen, T.H., Sigman, M., Ghezelbash, A., Doty, R.C. and Korgel, B.A., *Solventless synthesis of copper sulfide nanorods by thermolysis of a single source thiolate-derived precursor.* Journal of the American Chemical Society, 2003. **125**(19): p. 5638-5639.
27. Zhang, C., Zhang, S., Yu, L., Zhang, Z., Zhang, P. and Wu, Z., *Size-controlled synthesis of monodisperse Ag_2S nanoparticles by a solventless thermolytic method.* Materials Letters, 2012. **85**: p. 77-80.
28. Cha, H.G., Lee, D.K., Kim, Y.H., Kim, C.W., Lee, C.S. and Kang, Y.S., *Solventless nanoparticles synthesis under low pressure.* Inorganic chemistry, 2008. **47**(1): p. 121-127.
29. Sigman, M.B., Ghezelbash, A., Hanrath, T., Saunders, A.E., Lee, F. and Korgel, B.A., *Solventless synthesis of monodisperse Cu_2S nanorods, nanodisks, and nanoplatelets.* Journal of the American Chemical Society, 2003. **125**(51): p. 16050-16057.
30. Ghezelbash, A., M.B. Sigman, and B.A. Korgel, *Solventless synthesis of nickel sulfide nanorods and triangular nanoprisms.* Nano Letters, 2004. **4**(4): p. 537-542.
31. James, S.L., Adams, C.J., Bolm, C., Braga, D., Collier, P., Friščić, T., Grepioni, F., Harris, K.D., Hyett, G., Jones, W. and Krebs, A., *Mechanochemistry: opportunities for new and cleaner synthesis.* Chemical Society Reviews, 2012. **41**(1): p. 413-447.
32. Park, J., Joo, J., Kwon, S.G., Jang, Y. and Hyeon, T., *Synthesis of monodisperse spherical nanocrystals.* Angewandte Chemie International Edition, 2007. **46**(25): p. 4630-4660.

33. Pradhan, N. and S. Efrima, *Single-precursor, one-pot versatile synthesis under near ambient conditions of tunable, single and dual band fluorescing metal sulfide nanoparticles.* Journal of the American Chemical Society, 2003. **125**(8): p. 2050-2051.
34. Landge, S., D. Ghosh, and K. Aiken, *Solvent-free synthesis of nanoparticles*, in *Green Chemistry*. 2018, Elsevier. p. 609-646.
35. Al-Shakban, M., Matthews, P.D., Deogratias, G., McNaughter, P.D., Raftery, J., Vitorica-Yrezabal, I., Mubofu, E.B. and O'Brien, P., *Novel xanthate complexes for the size-controlled synthesis of copper sulfide nanorods.* Inorganic chemistry, 2017. **56**(15): p. 9247-9254.
36. Tang, A., Wang, Y., Ye, H., Zhou, C., Yang, C., Li, X., Peng, H., Zhang, F., Hou, Y. and Teng, F., *Controllable synthesis of silver and silver sulfide nanocrystals via selective cleavage of chemical bonds.* Nanotechnology, 2013. **24**(35): p. 355602.
37. Pradhan, N., B. Katz, and S. Efrima, *Synthesis of high-quality metal sulfide nanoparticles from alkyl xanthate single precursors in alkylamine solvents.* The Journal of Physical Chemistry B, 2003. **107**(50): p. 13843-13854.
38. Liu, Y., Qin, D., Wang, L. and Cao, Y., *A facile solution route to CuS hexagonal nanoplatelets.* Materials chemistry and physics, 2007. **102**(2-3): p. 201-206.
39. Mirkovic, T., Hines, M.A., Nair, P.S. and Scholes, G.D., *Single-source precursor route for the synthesis of EuS nanocrystals.* Chemistry of materials, 2005. **17**(13): p. 3451-3456.
40. Khan, M.D., Aamir, M., Sohail, M., Bhoyate, S., Hyatt, M., Gupta, R.K., Sher, M. and Revaprasadu, N., *Electrochemical investigation of uncapped $AgBiS_2$ (schapbachite) synthesized using in situ melts of xanthate precursors.* Dalton Transactions, 2019. **48**(11): p. 3714-3722.
41. Pejova, B., Nesheva, D., Aneva, Z. and Petrova, A., *Photoconductivity and relaxation dynamics in sonochemically synthesized assemblies of $AgBiS_2$ quantum dots.* The Journal of Physical Chemistry C, 2010. **115**(1): p. 37-46.
42. So, D., *Copper indium sulfide colloidal quantum dot solar cells.* 2016.
43. González-Pedro, V., Xu, X., Mora-Sero, I. and Bisquert, J., *Modeling high-efficiency quantum dot sensitized solar cells.* ACS nano, 2010. **4**(10): p. 5783-5790.
44. Saah, S.A., *Synthesis and characterization of lead sulphide nanoparticles from lead alkyl xanthate single source precursors using a solventless method*. 2013.

45. Kaltenhauser, V., Rath, T., Haas, W., Torvisco, A., Müller, S.K., Friedel, B., Kunert, B., Saf, R., Hofer, F. and Trimmel, G., *Bismuth sulphide–polymer nanocomposites from a highly soluble bismuth xanthate precursor.* Journal of Materials Chemistry C, 2013. **1**(47): p. 7825-7832.

CHAPTER FOUR:

CONCLUSIONS AND RECOMMENDATIONS

4.1.Summary and Conclusion

A facile and scalable synthesis of technologically important binary and ternary metal sulfides (CoS and $AgBiS_2$), and cationically (Ag, Cu, Zn, Cd, Ni, Fe and Sb) doped CoS and $AgBiS_2$ was performed successfully, using respective metal ethyl xanthate complexes. Thermogravimetric analysis indicated that all complexes show clean thermal decomposition at fairly moderate temperatures. All xanthate complexes (*i.e.* CuEtX, CoEtX, CdEtX, NiEtX, AgEtX, FeEtX BiEtX, SbEtX and FeEtX (where EtX = ethyl xanthate)) showed a single step decomposition, except ZnEtX complex which showed a two-step decomposition. All xanthate complexes were decomposed almost around 200 °C, and the residual mass confirms formation of respective metal sulphides. It provides an opportunity to prepare different binary, ternary or doped metal sulphides at relatively low temperature. The melt method is comparatively easy and user friendly as fewer parameters are involved for reaction optimization, and no solvents/capping ligands are required. The formations of binary system (*i.e.* CoS, Zn^{2+} doped CoS, Cd^{2+} doped CoS, Ni^{2+} doped CoS, Fe^{3+} doped CoS and Ag^{+} doped CoS) and ternary system ($AgBiS_2$ and $AgBiS_2$ doped with Cu^{2+}, Sb^{3+} and Fe^{3+}) were characterised by different techniques to determine the phase, morphology, shape transformation and elemental distribution, using X-Ray diffraction (p-XRD), transmission electron microscopy (TEM), scanning electron microscopy (SEM) and EDX for both binary and ternary system. UV-vis was used for binary system to observe the effect of dopants on optical properties of CoS. The results showed that ethyl xanthate ligand and melt method can be used for scaling up materials for applications in renewable energy.

4.2 Recommendations for Future Work

The potential of binary/ternary nanomaterials synthesized in this work will be used to investigate their electrocatalytic properties. The materials will specifically be investigated for supercapacitance and water splitting; and the effect of cationic substituents on the catalytic performance will be studied in detail. This work can therefore be extended to the actual applications of the nanomaterial. The identification of a potentially active material will be a step closer to the green energy and minimising the dependency on non-renewable energy sources.

4.3 Research outputs

Two papers are expected to be published in fairly good journals *i.e.* chapter two binary materials and chapter three discussing ternary materials. The work has been presented in conferences, both locally and internationally:

Conferences

1. Oral presentation: Materials for renewable and sustainable energy, 2019, Amonoo-neizer conference centre (IDL), Kwame Nkrumah University of Science and Technology, Kumasi, Ghana.
2. Oral presentation: Science and agriculture post graduate Symposium UNIZULU, 2019, Kwa-Dlangezwa, South Africa.
3. Oral presentation: UNIZULU Nanotechnology mini symposium, 2019, Bon hotel, Empangeni South Africa.